Bedrock incision due to the interaction between flow and sediment transport in uniformly curved channels

ANDRIAMBOAVONJY Mamy Rija

A thesis submitted in partial fulfillment of the requirements for the degree of

Doctor of Engineering

Examination Committee

Prof. Norihiro IZUMI

Assoc. Prof. Toshiki IWASAKI

Prof. Yasunori WATANABE

Doctoral Theis No.

Division of Field Engineering for the Environment

Graduate School of Engineering, Hokkaido University

March 2023

Acknowledgment

First of all, "Yours, O Lord, is the strength and the power and the glory, and the authority and the honor: for everything in heaven and on earth is yours; yours is the kingdom, O Lord, and you are lifted up as head over all." (1 Chronicles 29:11).

This dissertation would not have been possible without the support, guidance, and encouragement of unique people who contributed their assistance in this work.

My first and most earnest acknowledgment must go to my advisor and supervisor, Professor Norihiro Izumi, for his scientific contributions throughout the work. During my experimental works, analytical development, manuscript-writing, and dissertation writing period, he encouraged me, provided valuable suggestions, and lots of good ideas. I express my appreciation for all his contributions to time, ideas, and guidance. Additionally, I would also like to offer great gratitude to Professor Tomohito Yamada for his scientific contributions, pieces of advice, suggestions, and comments, and for giving me direction.

I would like to thank Dr. Hiroki Okachi for his continuous support and Mr. Tomoya Terakado for assisting me with the experimental measurements. The list of people who helped me is extensive; impossible to mention everyone involved here. However, thanks to the River and Watershed Engineering Laboratory members, the e3 Community, and the staff. Thank you for everything; you made my life easier and more pleasant here.

During the COVID pandemic, SOWA Project supported a lot; thank you! The financial support for this Ph.D. work came from the Japanese Government Scholarship (MEXT) and the River and Watershed Engineering Laboratory led by Prof. Norihiro Izumi. Please find here my sincere gratitude.

My parent and family have been an essential motivation for supporting my emotion and morals during my Ph.D. time. Not easy to be the first kid in the family; I am far from perfect, but I dedicate this to you, sisters and brothers. Valiha and Kintanay - my daughters, no matter how distant we are, you are always the source of my motivation, the strength that picks me up whenever I am down. I said a long time ago, and I want to become "Plusieurs-genieur," not only "1-genieur" here I am, Dad. You always motivate and show me to be a good man. Mom, you are always part of me. THANK YOU.

Lau, I wonder how to thank you. Five – six years, we have been separated, many things happened, up-and-downs, come-and-go…you were there, yet still here, supporting me. No words can express it; at least receive my humble and sincere "thank you".

ありがとうございます。

Finally, I would like to close this section by saying, "Put all your hope in God, not looking to your reason for support." (Proverbs 3:5).

Abstract

This study aims to investigate the bedrock incision in uniformly curved channels. The flow dynamics and mass transfer in curved channels are more complex than the straight channels due to the inherent spiral flow. The spiral flow combines the channel's primary/streamwise and secondary/transverse flow. This particular flow drags and deposits the sediment along the inner wall. However, this specific feature raises questions regarding how it can affect the bed erosion of the channels.

The actual study mainly uses analytical and experimental methods. The flow characteristics in curved channels are analytically derived, as well as the deposition morphology - transverse slope bed profile. The experiments are conducted to investigate the bedrock incision in uniformly curved channels. The flow conditions necessary to produce the spiral flow are presumed to be met; however, bedload transport of sediment predominates with minor suspended sediment. Moreover, it is assumed that the primary erosion of the channel bedrock occurs by incision, i.e., by physical interaction between the bedrock surface and the sediment grains displacement, such as grain saltation or sliding.

The flow velocities in uniformly curved channels are derived from the three-dimensional Reynolds-averaged Navier-Stokes equations and the continuity equation. For simplicity and due to the symmetricity, the channel is subdivided into two similar domains, the lower and the upper half domains. The wall effect is neglected. After the normalization, the equations are expressed as a function of the parameter ϵ - the channel width ratio for the curvature radius. The primary/streamwise flow velocity is obtained as the solution of the normalized equation for straight channels. The secondary flow velocity, however, is obtained by

doing the asymptotic expansion on ϵ. The velocities are obtained separately from the predefined domains but satisfy the continuity at the center of the channel. The flow velocities are expressed as funa ction of the boundary roughness z0. The transverse bed profile is obtained using the lateral sediment transport equation with the previous flow velocities in the equilibrium state.

It is found that the flow velocities distribution along the vertical is generally symmetrical, due to the assumption that the top ceiling and the bottom would have the same roughness. Indeed, the boundary roughness greatly influences the shape of the flow velocity distribution: the water column flows more uniformly, and there is less secondary flow at smoother boundaries. Additionally, the transverse slope becomes steeper with the boundary roughness and with the depth-average velocity

On the other hand, the experiments in an annular flume aim to simulate the bedrock incision. Two cases – Case 1 and Case 2 are carried out, each with different rotation speeds of the top ceiling, 40 and 48 RPM, respectively. Both cases use plaster as the bedrock and the same amount of sediment - grain size 0.45 mm, density 2.61 g/cc - as the abrasive tools. In both cases, sediment motion is kept as bedload transport. It is found that the sediment deposition and the moving bedforms along the inner wall differ for each case. A uniform transverse slope is observed for a rotation speed o, 4,8 RPM, and wavy bedforms are found for a rotation speed of 40 RPM. The bedrock incision results in the development of the inner channel along the base of the transverse slope. This inner channel grows more quickly and toward the inner wall under the wavy bedforms than under the uniform transverse slope. These findings suggest that in the case of bedload transport of the sediment, the bedrock erosion would depend mainly on the bed morphology, and that the bedform influences more on the bedrock incision than flow speed.

Nevertheless, comparing the analytical results with the experimental data shows suitable agreements. Such results are obtained under the following conditions: the

depth-averaged flow velocity is estimated to be 60 - 70 % of the top ceiling speed, and the boundary roughness becomes a “bedform roughness” for wavy bedforms and a “grain roughness” for uniform transverse slope.

The thesis includes five chapters. Chapter 1 introduces the background, literature review, objectives, and organization of this study. Chapter 2 introduces the theoretical model to evaluate the secondary flow in uniformly curved closed channels using the mixing length turbulent model, one of the simplest turbulent closure models, and demonstrates their primary and secondary flow solutions. In addition, the shape of sediment deposition in the riverbed is derived from the velocity profiles in the uniformly curved channel obtained in the analysis. Chapter 3 describes laboratory experiments using a uniformly curved closed channel, with a detailed description of the results of the experiments. Chapter 4 compares the experimental and analytical results and discusses the physical implications of the results. Finally, Chapter 5 and 6 deal with the discussion and the conclusions, respectively, with several recommendations for future studies.

Contents

List Figures

List of Tables

1 Introduction

Natural mechanisms for river path changes include alluvial and incision meandering. The former is mainly the result of bank erosion on an alluvial plain, and the latter happens when a bedrock incision occurs [1,2]. In alluvial meandering, the floodplains are usually well-vegetated and rich in fine sediment. The combination of vegetation and fine sediment slows down the erosion and the lateral expansion of the river, which positively impacts the aquaculture of the river system [3,4]. In contrast, meandering by the incision is commonly active on the bedrock and plays an essential role in landscape evolution. This explains why discussions on river incisions tend to be limited to their contribution to landscape evolution [5,6]. Nonetheless, the incision meandering also finds its implication in different fields, such as engineering. The bedrock incisions were first discussed from an engineering perspective at the end of the nineteenth century, with arguments about their dynamics [7,8] and recently about their importance in urbanism and construction alongside river paths [9–11].

Here, the bedrock incision is investigated due to the interaction between flow and sediment transport in uniformly curved channels. According to previous studies, the main parameters influencing bedrock incisions are sediment distribution, channel geometry, and flow fluctuation [12]. Sklar and Dietrich suggested that bedrock incisions occur at the optimal bed coverage and shear stress [13]. On the other hand, Zhang et al. [14] proposed a model considering the local bed state by integrating the bed cover fraction and the ratio of alluvial thickness to bedrock macro-roughness. These two models assume that the bedload transport of the sediment and the sediment grain saltation on the bedrock is the origin of the incision. While these interpretations are widely accepted, few studies have examined the factors influencing bedrock incisions in curved channels.

Both alluvial and incision meandering cause infrastructures such as bridges and construction to collapse (e.g., [15,16]). Consequently, several human interventions are done along the river channels to prevent such hazards, including but not limited to dam construction, bank revetment, groins, and so on (e.g., [17–19]). They are supposed to control

the stream power (flow, sediment transport control…). Those interventions mainly deal with the riverbanks where the erosion occurs quickly, leaving the riverbed more or less unattended. Interestingly, Simon and Rinaldi suggested that those interventions lead to the increase of the bed channel degradation/incisions as feedback to a disturbance in which an excess of flow energy, shear stress, or stream power occurs relative to the amount of sediment supplied to the stream [20]. Several studies reported from field observation that any intervention on the riverbank for its protection increases the bed incision. In contrast, no intervention results in less or no bed erosion. Notably, Amissah et al. [9] reported the degradation of the bed along the inner side of a curved part of the Tisza River in Hungary. They highlighted that such a phenomenon might threaten humanity and need to be considered in the community's urbanization or development.

In curved channels, the generation of helical/spiral flow, as presented in Figure 1, is the main flow feature (e.g., [21]). The imbalance between the uniformly distributed pressure gradient and the non-uniform centrifugal force causes the spiral flow. The term spiral flow will be used throughout this document for convenience. The spiral flow is the combination of the tangential/longitudinal/primary and the transversal/radial/secondary flows—also, the terms primary and secondary flows will be used from this point forward. Previous studies demonstrated that, near the surface, the flow goes diagonally from the inner wall to the outer wall and then goes down along the outer wall; at the bottom, it flows from the outer wall to the inner wall, where it rises again, and so forth [21–25]. Exceptionally, the reverse spiral flow may also be observed in the case of a density-driven flow, whose maximum primary velocity is observed near the bed [26]. Anyhow, this flow pattern forces the redistribution of the velocity and the bed shear stress and has consequences on bed morphology and engineering [9,24,27–35].

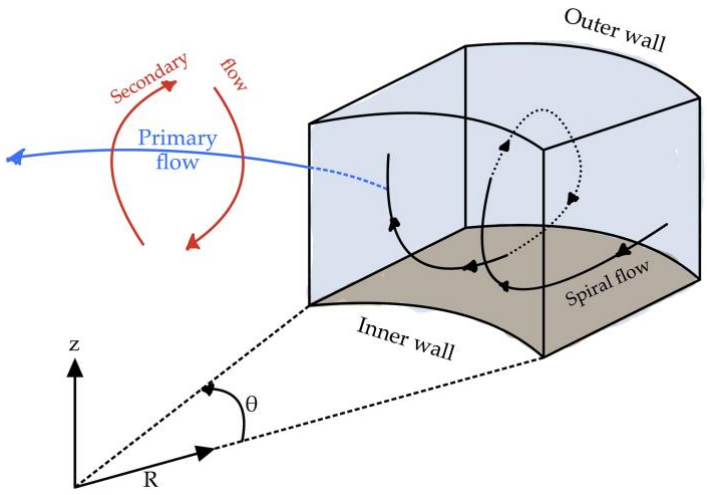

Figure 1: Schematic diagram of the spiral flow along curved channels as the combination of the primary and the secondary flow.

Erosion typically occurs on the outer bank of curved channels due to the quick erosion process on that side, posing risks and threats to the area [4,36]. River channels, particularly curved ones, were subjected to several interventions to manage the flow and sediment transport to prevent such catastrophes. These interventions include but are not limited to, the construction of levee dams, artificial meander cutoffs, bank protection, and stabilization [37]. Despite this, the riverbed frequently receives less care and is left unattended, and in this instance, it is the weakest and least protected part of the channel, subject to potential erosion, with little research done [38].

Due to its complexity, spiral flow studies are often conducted experimentally, numerically, or analytically [39–41]. The actual study - bedrock incision due to the interaction between flow and sediment transport in uniformly curved channels will be investigated analytically and experimentally.

Recently, the annular flume has been widely adopted to study hydrodynamics in curved channels experimentally. This is because the annular flume allows a continuous spiral flow to be reproduced like that in curved channels during the necessary timespan (e.g., [23,42–45]). Also, to control the spiral flow, the rotation of the cover lid of the annular flume is varied, and the other parameters are maintained at constant values (water depth, sediment

amount, and caliber) [14,43,44]. In the present study, the rotation speed of the cover lid is the primary variable to monitor the flow, sediment transport and deposition investigations, and the erosion process.

A review of the literature on the experiments using an annular flume found that the flow velocity components (primary and secondary) and the bed shear stress increase with the top lid rotation speed (e.g., [23,43]). The primary flow velocity increases from the inner wall towards the outer wall; the shear stress may also increase towards the inner wall with the increase of the bed roughness [41]. Simultaneously, the sediment is dragged towards the inner bank and forms the transverse slope (e.g., [22,46–49]). The secondary flow velocity is less than half of the primary flow velocity near the bed [23]; when the flow pattern varies in space and time, the bed topography also fluctuates, and conversely (e.g., [14,39,43,50,51]). The minimal second flow criteria are met after the cover lid rotation begins. The sediment is deposited along the inner wall, forming a uniform transverse slope that gradually turns into regular deposition patterns (e.g., [27,43,49–51]). Taguchi et al. [32,33] discovered a limited incised area experimentally and suggested that the erosion mainly occurs under the moderately covered bed, namely at the base of the transverse slope. They added the alternation of the bed's condition between covered and exposed as another contributing factor to the erosion. Their results were obtained with a constant cover lid rotation speed of 40 RPM, and mortar simulated the bedrock. In contrast, the experiments in the present study adopt two different rotation speeds, one with 40 RPM for reference with the previous study and the second one with 48 RPM; in addition, plaster is used for the bedrock, and the experiments are performed longer in time to see the advanced state of the erosion growth.

Often, the flow velocities models derived from open curved channels are adopted to compare with the experimental data, employing approximations and assumptions and leading to a certain level of agreement, or vice-versa [28,30,31,52]. Flow velocity and transverse bed profile models will be derived analytically in this study. The analytical part uses a variation of Engelund F. [22] and Sheng Y. [23]'s approaches and allows to express the flow model as a function of the boundary roughness. The spiral flow is still complex,

even using the annular flume. Nonetheless, Engelund has already noted an unrealistic velocity near the top lid. Sheng also highlighted that the results could not correctly describe the turbulent boundary layer using a laminar model.

The experiments will be conducted to monitor the interaction between the flow and the sediment transport on the bedrock incision, an interaction that is based on the bottom roughness. First, the flow velocity distribution will be derived to study the bedrock incision due to the interaction between flow and sediment transport in uniformly curved channels. From that will be calculated the transverse bed slope model, which will be compared with the transverse slope obtained experimentally.

After this introduction, Chapter 2 introduces the theoretical model to derive the primary and secondary flow in uniformly curved closed channels using the mixing length turbulent model. The transverse slope model in the uniformly curved channel will be derived from those flow velocities. Chapter 3 will describe laboratory experiments using a uniformly curved closed channel, with a detailed description of the results of the experiments. The validation of the experimental and analytical results is in Chapter 4. Chapter 5 is dedicated to the discussion, and the conclusions of this study are given in chapter 6, with some recommendations for future studies.

2 Bed transverse slope in uniformly curved channels

This chapter will derive the secondary flow in uniformly curved closed channels. The turbulent model, "the mixing length turbulent model," will be adopted to obtain the main flow and secondary flow velocities. In addition, the analytical transverse slope of the sediment deposition in the riverbed will also be expressed from the velocity profiles in the uniformly curved channel obtained in the analysis.

2.1 Formulation

2.1.1 Governing equation

The Reynolds-averaged Navier-Stokes equations and the continuity equation for sufficiently shallow flow in a curved channel read:

$$\frac{r_0^*}{r_0^*+n^*}u^*\frac{\partial u^*}{\partial s^*}+v^*\frac{\partial u^*}{\partial n^*}+w^*\frac{\partial u^*}{\partial z^*}+\frac{u^*v^*}{r_0^*+n^*}=-\frac{1}{\rho}\frac{r_0^*}{r_0^*+n^*}\frac{\partial p^*}{\partial s^*}+\frac{\partial}{\partial z^*}\left(\nu_T^*\frac{\partial u^*}{\partial z^*}\right) \quad (1)$$

$$\frac{r_0^*}{r_0^*+n^*}u^*\frac{\partial v^*}{\partial s^*}+v^*\frac{\partial v^*}{\partial n^*}+w^*\frac{\partial v^*}{\partial z^*}-\frac{u^{*2}}{r_0^*+n^*}=-\frac{1}{\rho}\frac{\partial p^*}{\partial n^*}+\frac{\partial}{\partial z^*}\left(\nu_T^*\frac{\partial v^*}{\partial z^*}\right) \quad (2)$$

$$\frac{r_0^*}{r_0^*+n^*}u^*\frac{\partial w^*}{\partial s^*}+v^*\frac{\partial w^*}{\partial n^*}+w^*\frac{\partial w^*}{\partial z^*}=-\frac{1}{\rho}\frac{\partial p^*}{\partial z^*}+\frac{\partial}{\partial z^*}\left(2\nu_T^*\frac{\partial w^*}{\partial z^*}\right)-g \quad (3)$$

$$\frac{r_0^*}{r_0^*+n^*}\frac{\partial v^*}{\partial s^*}+\frac{\partial v^*}{\partial n^*}+\frac{\partial w^*}{\partial z^*}+\frac{v^*}{r_0^*+n^*}=0 \quad (4)$$

Where s^*, n^* And z^* are the coordinates in the streamwise, lateral and depth directions respectively; u^*, v^* and w^* are the velocity components in the s^*, n^* and z^* directions respectively, r_0^* is the curvature radius of the channel center, p^* is the pressure, ν_T^* is the eddy viscosity, and g is the gravity acceleration. Note that we take the origins of n^* and z^* at the lateral and depth centers of the channel, respectively.

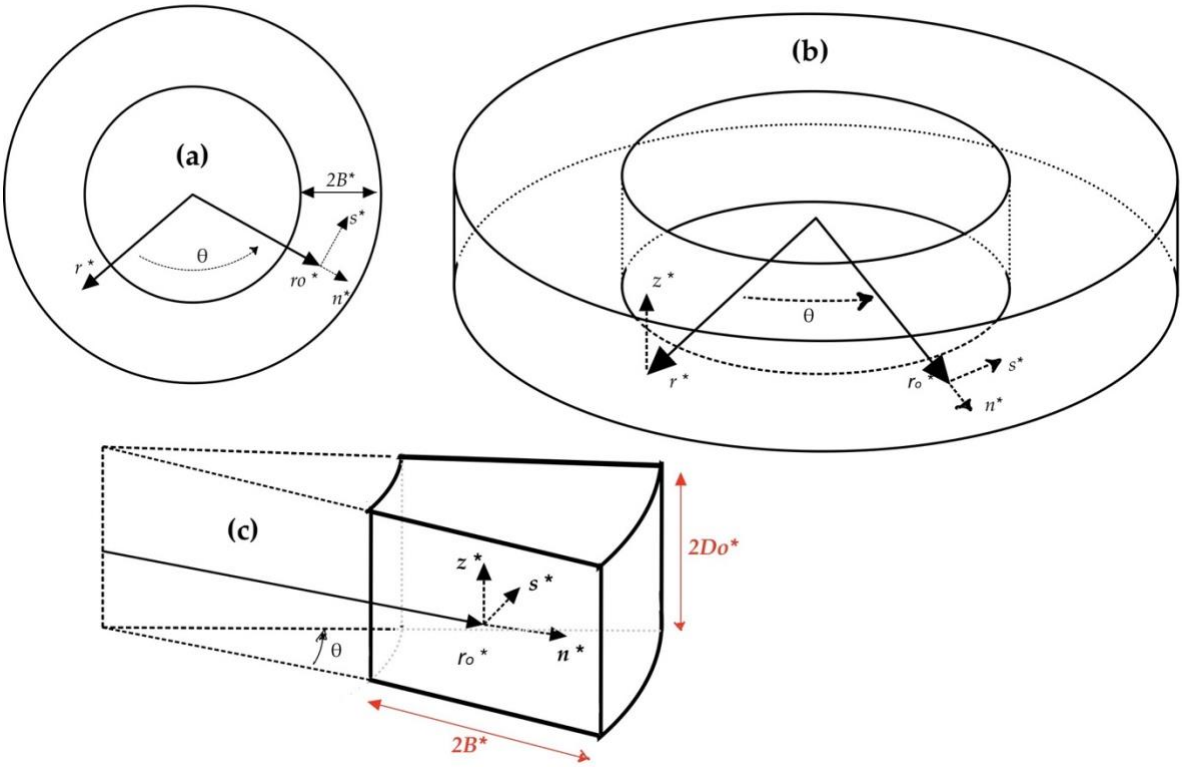

Figure 2: Representation of the coordinate system: (a) Top view, (b) 3D view, and (c) Section view

2.1.2 Normalization

In this study, we express the normalization of the form:

$$(s^*, n^*) = B^*(s,n) \quad (5.a) \qquad z^* = D_0^* z \quad (5.b) \qquad r_0^* = R_0^* r_0 = \frac{R_0^*}{C} \quad (5.c)$$

$$(u^*, v^*) = U_a^*(u,v) \quad (5.d) \qquad w^* = \frac{U_a^*}{\beta} w \quad (5.e) \qquad p^* - \rho g(D_0^* - z^*) = \rho U_a^{*2} p \quad (5.f)$$

$$\nu_T^* = U_a^* D_0^* \nu_T \quad (5.g)$$

where B^* is the half–width of the channel, D_0^* is the half-height of the channel, U_a^* is the depth-averaged velocity in the flume, R_0^* is a typical curvature radius, C is the non-dimensional curvature (inverse of r_0), p is the normalized piezometric pressure, and β is the aspect ratio defined by B^*/D_0^*. As already described, the origins of n, and z are located

at the lateral and depth centers of the channel, respectively (Figure 2). Therefore, the flow domain is $-1 \leq n \leq 1$ and $-1 \leq z \leq 1$.

Applying these to the equations (1) to (4), we obtain:

$$\frac{1}{1+\epsilon nC} u \frac{\partial u}{\partial s} + v \frac{\partial u}{\partial n} + w \frac{\partial u}{\partial z} + \frac{\epsilon C u v}{1+\epsilon nC} = -\frac{1}{1+\epsilon nC} \frac{\partial p}{\partial s} + \beta \frac{\partial}{\partial z}\left(\nu_T \frac{\partial u}{\partial z}\right) \quad (6)$$

$$\frac{1}{1+\epsilon nC} u \frac{\partial v}{\partial s} + v \frac{\partial v}{\partial n} + w \frac{\partial v}{\partial z} - \frac{\epsilon C u^2}{1+\epsilon nC} = -\frac{\partial p}{\partial n} + \beta \frac{\partial}{\partial z}\left(\nu_T \frac{\partial v}{\partial z}\right) \quad (7)$$

$$\frac{1}{1+\epsilon nC} u \frac{\partial w}{\partial s} + v \frac{\partial w}{\partial n} + w \frac{\partial w}{\partial z} = -\beta^2 \frac{\partial p}{\partial z} + \beta \frac{\partial}{\partial z}\left(2\,\nu_T \frac{\partial w}{\partial z}\right) - F^{-2} \quad (8)$$

$$\frac{1}{1+\epsilon nC} \frac{\partial u}{\partial s} + \frac{\partial v}{\partial n} + \frac{\partial w}{\partial z} + \frac{\epsilon C v}{1+\epsilon nC} = 0 \quad (9)$$

where F is the Froude number, and ϵ is the ratio of the half-width for the typical curvature radius of the channel; it is a parameter defining the sinuosity of the channel and is expressed by:

$$\epsilon = \frac{B^*}{R_0^*} \quad (10)$$

2.2 Analytical solutions – Uniformly Curved Channels

2.2.1 Primary flow velocity – Solution for straight channels

Except near the side walls ($n = \pm 1$), the following equation holds:

$$C = 1, \qquad \frac{\partial}{\partial s} = 0, \qquad w = 0 \tag{11}$$

Then, the equations (6) - (9) reduce to:

$$v\frac{\partial u}{\partial n} + \frac{\epsilon u v}{1+\epsilon n} = \beta\frac{\partial}{\partial z}\left(\nu_T \frac{\partial u}{\partial z}\right) \tag{12}$$

$$v\frac{\partial v}{\partial n} - \frac{\epsilon C u^2}{1+\epsilon n C} = -\frac{\partial p}{\partial n} + \beta\frac{\partial}{\partial z}\left(\nu_T \frac{\partial v}{\partial z}\right) \tag{13}$$

$$\beta^2 \frac{\partial p}{\partial z} = F^{-2} \tag{14}$$

$$\frac{\partial v}{\partial n} + \frac{\epsilon v}{1+\epsilon n} = 0 \tag{15}$$

Remember that ϵ is the ratio of B^* to R_0^*. It follows that if the channel is straight, then R_0^* is infinity, the lateral velocity and the variation in the lateral direction vanish. Therefore, we have the following relations:

$$\epsilon = 0, \qquad v = 0, \qquad \frac{\partial}{\partial n} = 0 \tag{16}$$

These relations reduce the equation (12) to:

$$\frac{\mathrm{d}}{\mathrm{d}z}\left(\nu_T \frac{\mathrm{d}u}{\mathrm{d}z}\right) = 0 \tag{17}$$

where we replace the partial derivatives with total derivatives because u is a function only of z. After the integration of this equation (17), we obtain:

$$\nu_T \frac{\mathrm{d}u}{dz} = C_f \tag{18}$$

where C_f is the friction coefficient defined by $\left(U_f^*/U_a^*\right)^2$, $\mathrm{U_f^*}$ is the shear velocity defined by $\sqrt{\frac{\tau^*}{\rho}}$, and $\tau^*$is the shear stress.

From Equation (18), we find that the shear stress is constant in the z direction in this flow. It means the shear stress exerted on the flow by the lid is exerted downward without change.

The kinematic eddy viscosity ν_T is defined by:

$$\nu_T = l^2 \left|\frac{\mathrm{d}u}{\mathrm{d}z}\right| \tag{19}$$

where l is the mixing length defined as the distance from the boundary.

2.2.1.1 *In the lower half domain*

In the lower half domain of the channel $(-1 \leq z \leq 0)$, the effect of the bottom is dominant, and the distance from the bottom to the height z is $1 + z$. Therefore, the mixing length l is defined by:

$$l = \kappa(1 + z) \tag{20}$$

Combining the above relation with (18) and (19), we obtain:

$$\kappa^2 (1 + z)^2 \left|\frac{\mathrm{d}u}{\mathrm{d}z}\right| \frac{\mathrm{d}u}{\mathrm{d}z} = C_f \tag{21}$$

The above differential equation has the solution of the form:

$$u = \frac{\sqrt{C_f}}{\kappa} \ln(1 + z) + C_0 \tag{22}$$

where C_0 is an integral constant which is determined by a great number of past experimental results. In the case of the bottom surface being smooth, it is found

$$u = \frac{\sqrt{C_f}}{\kappa} \ln[9Re(1 + z)] \tag{23}$$

where Re is the Reynolds number defined by

$$Re = \frac{U_f^* \, D_0^*}{\nu} \tag{24}$$

where ν is dynamic viscosity of the fluid.

In the case of the bottom surface being rough, it is found

$$u = \frac{\sqrt{C_f}}{\kappa} \ln\left[\frac{30\,(1+z)}{k_s}\right] \tag{25}$$

where k_s is the roughness height.

The velocity distribution in the lower half can be written in the following unified form:

$$u \;=\; \frac{\sqrt{C_f}}{\kappa} ln\left(\frac{1\,+z}{z_0}\right) \tag{26}$$

$$z_0 = \begin{cases} \dfrac{1}{9Re} & for\ smooth\ boundary \\ \dfrac{k_s}{30} & for\ rough\ boundary \end{cases} \tag{27}$$

2.2.1.2 *In the upper half-domain*

In the upper half domain of the channel ($0 \le z \le 1$), the effect of the ceiling is dominant. Because the distance from the ceiling to the height z is $1 - z$, the mixing length l is defined by:

$$l \;=\; \kappa\,(1 \,-\, z\,) \tag{28}$$

Combining the above relation with (18) and (19), we obtain

$$\kappa^{\,2}\,(1 \,-\, z\,)^2 \left|\frac{\mathrm{d}u}{\mathrm{d}z}\right| \frac{\mathrm{d}u}{\mathrm{d}z} = \; C_f \tag{29}$$

and after some modification, we obtain:

$$\mathrm{d}u \;=\; -\,\frac{\sqrt{C_f}}{\kappa}\,\frac{\mathrm{d}(1\,-z)}{1\,-\,z} \tag{30}$$

The above differential equation has the solution of the form:

$$u = -\frac{\sqrt{C_f}}{\kappa}\ln(1-z) + C_1 \tag{31}$$

Assuming that the ceiling has the same roughness as the bottom, and that the flow velocity where $z = 1 - z_0$ is the moving speed of the ceiling U_c we obtain the constant of integration:

$$C_1 = U_c + \frac{\sqrt{C_f}}{\kappa}\ln z_0 \tag{32}$$

And the velocity distribution in the upper half domain is thus:

$$u = U_c - \frac{\sqrt{C_f}}{\kappa}\ln\left(\frac{1-z}{z_0}\right) \tag{33}$$

Furthermore, the solutions in the lower and upper half domains should be matched at the depth center of the channel ($z = 0$), such that:

$$\frac{\sqrt{C_f}}{\kappa}\ln\frac{1}{z_0} = U_c - \frac{\sqrt{C_f}}{\kappa}\ln\frac{1}{z_0}\ln\frac{1}{z_0} \tag{34}$$

From the above equation, we obtain the relation of the form:

$$C_f = \left(\frac{\kappa U_c}{2\ln(1/z_0)}\right)^2 \tag{35}$$

Substituting the above relation into (26) and (33), we find that the velocity u in the whole domain is written in the form:

$$u(z) = \begin{cases} \dfrac{U_c}{2}\left(1 - \dfrac{\ln(1+z)}{\ln z_0}\right) & (-1 \le z \le 0) \\ \dfrac{U_c}{2}\left(1 + \dfrac{\ln(1-z)}{\ln z_0}\right) & (0 \le z \le 1) \end{cases} \tag{36}$$

Note that the velocity vanishes at the point where the distances from the bottom and ceiling are both z_0 ($z = -1 + z_0$ and $z = 1 - z_0$, respectively). Taking the depth average of the above equation, we obtain the depth-averaged velocity in the form

$$\begin{aligned}
\frac{1}{2}\int_{-1}^{1} u \, \mathrm{d}z \quad &= \int_{-1}^{0} \frac{U_c}{4}\left(1 - \frac{\ln(1+z)}{\ln z_0}\right)\mathrm{d}z + \int_{0}^{1} \frac{U_c}{2}\left(1 + \frac{\ln(1-z)}{\ln z_0}\right)\mathrm{d}z \\
&= \frac{U_c}{4}\left[z - \frac{(1+z)\ln(1+z) - (1+z)}{\ln z_0}\right]_{-1}^{0} \\
&\qquad + \frac{U_c}{4}\left[z - \frac{(1-z)\ln(1-z) - (1-z)}{\ln z_0}\right]_{0}^{1} \qquad (37) \\
&= \frac{U_c}{4}\left(\frac{1}{\ln z_0} + 1\right) + \frac{U_c}{4}\left(1 - \frac{1}{\ln z_0}\right) \\
&= \frac{U_c}{2}
\end{aligned}$$

Furthermore, because the non-dimensional depth-averaged velocity should be equal to 1 due to the normalization, we find that $U_c = 2$. Thus, (36) is rewritten in the form, and is presented in Figure 3:

$$u(z) = \begin{cases} 1 - \dfrac{\ln(1+z)}{\ln z_0} & (-1 \le z \le 0) \\ 1 - \dfrac{\ln(1-z)}{\ln z_0} & (0 \le z \le 1) \end{cases} \qquad (38)$$

In addition, the important resistance law (35) reduces to:

$$C_f = \left(\frac{1}{k}\ln\frac{1}{z_0}\right)^{-2} \qquad (39)$$

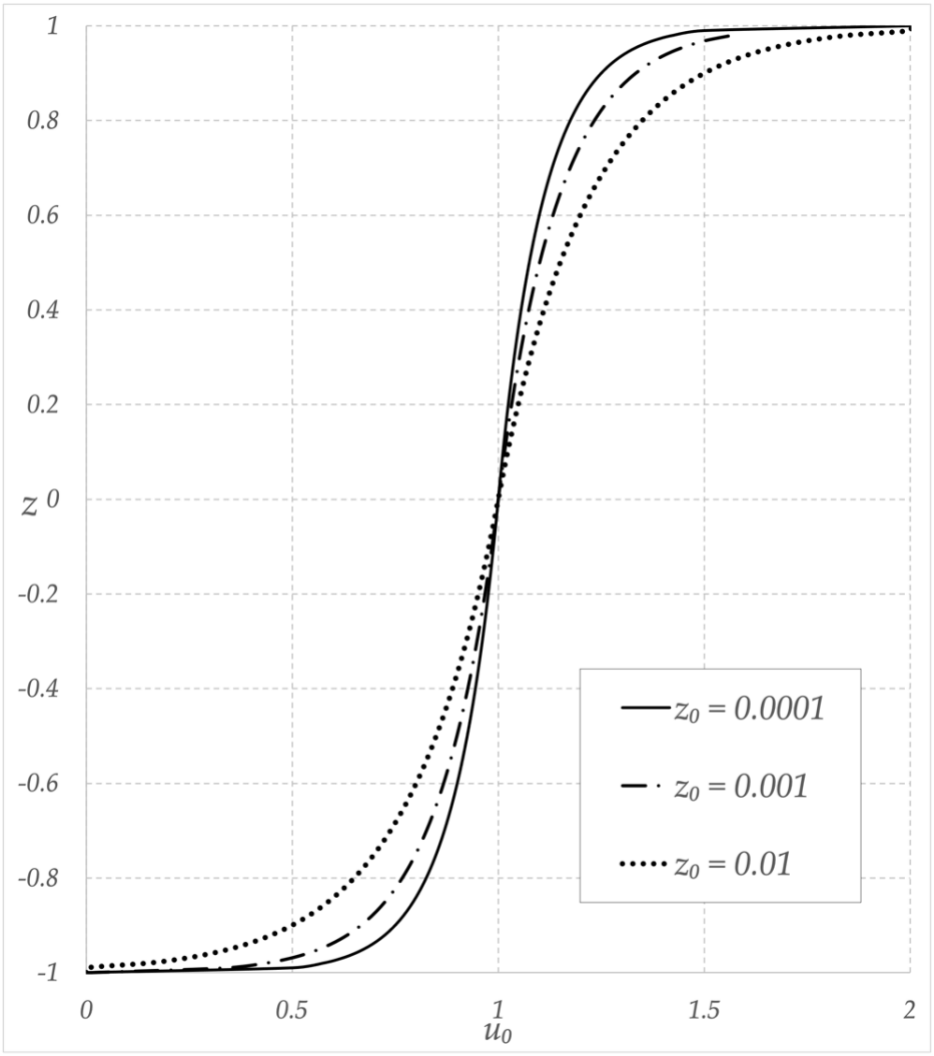

Figure 3: Non dimensional streamwise U velocity distribution along the vertical.

The primary flow velocity distribution along the vertical direction, expressed in Equation (38), is plotted in Figure 3. The plot is non-dimensional, the vertical axis represents the z-direction and the horizontal axis represents the primary flow. It is shaped like a standing letter "S" and symmetrical at the channel center, located at $(u_0, z) = (1, 0)$. Three graphs with different values of z_0 are presented and show that the roughness increase affects the velocity distribution shape and makes the near-boundary velocity rise and reduce.

2.2.2 Secondary flow velocity - Asymptotic expansions

We expand u, v and p with the use of ϵ in the form

$$u = u_0(z) + \epsilon u_1(s,n,z) + \epsilon^2 u_2(s,n,z) + \cdots \quad (40)$$

$$v = \epsilon v_1(s,n,z) + \epsilon^2 v_2(s,n,z) + \cdots \quad (41)$$

$$p = \epsilon p_1(s,n) + \epsilon^2 p_2(s,n) + \cdots \quad (42)$$

As already described, ϵ is the parameter standing for the channel sinuosity; therefore, the terms of $O(\epsilon^0)$ correspond to solutions for straight channels. It follows that (38) corresponds to $u_0(z)$.

Substituting the above expansions (40)-(42) into (12), (13), and (15), and picking up the terms of each order of ϵ, we obtain the following results.

$$0 = \beta \frac{\partial}{\partial z}\left(\nu_{T0} \frac{\partial u_1}{\partial z}\right) \quad (43)$$

$$-u_0^2(z) = -\frac{\partial p_1}{\partial n} + \beta \frac{\partial}{\partial z}\left(\nu_{T0} \frac{\partial v_1}{\partial z}\right) \quad (44)$$

$$\frac{\partial v_1}{\partial n} = 0 \quad (45)$$

where

$$\nu_{T0} = \begin{cases} \kappa^2(1+z)^2 \left|\frac{\mathrm{d}u_0}{\mathrm{d}z}\right| = \kappa(1+z) & (-1 \le z \le 0) \\ \kappa^2(1-z)^2 \left|\frac{\mathrm{d}u_0}{\mathrm{d}z}\right| = \kappa(1-z) & (0 \le z \le 1) \end{cases} \quad (46)$$

From (45), we find v_1 not a function of n. Then, $\frac{\partial p_1}{\partial n}$ in (44) is not a function of n either. Because p_1 is not a function of z, $\frac{\partial p_1}{\partial n}$ turns out to be a constant. We assume that $\frac{\partial p_1}{\partial n} = a$, hereafter.

2.2.2.1 *Secondary flow velocity in the lower half*

In the lower half domain $(-1 \le z \le 0)$, we find (44) to be

$$\frac{\mathrm{d}}{\mathrm{d}z}\left(\kappa(1+z)\frac{\mathrm{d}v_1}{\mathrm{d}z}\right) = \frac{1}{\beta}\left[a-\left(1-\frac{\ln(1+z)}{\ln z_0}\right)^2\right]$$

$$= \frac{1}{\beta}\left[a-1+2\frac{\ln(1+z)}{\ln z_0}-\frac{(\ln(1+z))^2}{(\ln z_0)^2}\right] \qquad (47)$$

The above differential equation describes the velocity distribution of the secondary flow v_1 in the lower half domain. Integrating the above relation for z, we obtain

$$\kappa(1+z)\frac{\mathrm{d}v_1}{\mathrm{d}z} = \frac{1}{\beta}\left[(a-1)(1+z)+2\frac{(1+z)\ln(1+z)-(1+z)}{\ln z_0}\right.$$
$$\left.-\frac{(1+z)(\ln(1+z))^2-2(1+z)\ln(1+z)+2(1+z)}{(\ln z_0)^2}\right]+C_2$$

$$= \frac{1}{\beta}\left[\left(a-1-\frac{2}{\ln z_0}-\frac{2}{(\ln z_0)^2}\right)(1+z)\right.$$
$$+\left(\frac{2}{\ln z_0}+\frac{2}{(\ln z_0)^2}\right)(1+z)\ln(1+z)$$
$$\left.-\frac{(1+z)(\ln(1+z))^2}{(\ln z_0)^2}\right]+C_2 \qquad (48)$$

where C_2 is an integral constant determined by the boundary conditions at the bottom and the matching conditions between the solutions in the upper and lower half domains. Note that the above equation is the shear stress due to the secondary flow and is used to match the solutions in the lower and upper half domains.

Dividing both hand sides of the above equation by $\kappa(1+z)$, we obtain

$$\frac{\mathrm{d}v_1}{\mathrm{d}z} = \frac{1}{\kappa\beta}\left[\left(a-1-\frac{2}{\ln z_0}-\frac{2}{(\ln z_0)^2}\right)+\left(\frac{2}{\ln z_0}+\frac{2}{(\ln z_0)^2}\right)\ln(1+z)-\frac{(\ln(1+z))^2}{(\ln z_0)^2}\right]$$
$$+\frac{C_2}{\kappa(1+z)} \qquad (49)$$

This equation is further integrated to be

$$
\begin{aligned}
v_1 = \frac{1}{\kappa\beta}\Bigg[&\left(a - 1 - \frac{2}{\ln z_0} - \frac{2}{(\ln z_0)^2}\right)(1+z) \\
&+ \left(\frac{2}{\ln z_0} + \frac{2}{(\ln z_0)^2}\right)\left((1+z)\ln(1+z) - (1+z)\right) \\
&- \frac{(1+z)(\ln(1+z))^2 - 2(1+z)\ln(1+z) + 2(1+z)}{(\ln z_0)^2}\Bigg] \\
&+ \frac{C_2}{\kappa}\ln(1+z) + C_3
\end{aligned}
\qquad (50)
$$

$$
\begin{aligned}
v_1 = \frac{1}{\kappa\beta}\Bigg[&\left(a - 1 - \frac{4}{\ln z_0} - \frac{6}{(\ln z_0)^2}\right)(1+z) + \left(\frac{2}{\ln z_0} + \frac{4}{(\ln z_0)^2}\right)(1+z)\ln(1+z) \\
&- \frac{(1+z)(\ln(1+z))^2}{(\ln z_0)^2}\Bigg] + \frac{C_2}{\kappa}\ln(1+z) + C_3
\end{aligned}
$$

The velocity should vanish at the bottom. However, the velocity of the secondary flow has a singularity at the bottom as the velocity of the main flow. Therefore, the velocity becomes $-\infty$ at the bottom. We assume that the velocity of the secondary flow vanishes at the point ($z = -1 + z_0$) where the velocity of the main flow vanishes. Applying this assumption $v(-1+z_0)=0$ to the above equation, we obtain a relation between C_2 and C_3 in the following form:

$$
C_3 = -\frac{1}{\kappa\beta}\left(a - \frac{6}{(\ln z_0)^2}\right)z_0 - \frac{C_2}{\kappa}\ln z_0 \qquad (51)
$$

Substituting the above equation into (50), we obtain:

$$
\begin{aligned}
v_1 = \frac{1}{\kappa\beta}\Bigg[&\left(a - 1 - \frac{4}{\ln z_0} - \frac{6}{(\ln z_0)^2}\right)(1+z) + \left(\frac{2}{\ln z_0} + \frac{4}{(\ln z_0)^2}\right)(1+z)\ln(1+z) \\
&- \frac{(1+z)(\ln(1+z))^2}{(\ln z_0)^2}\Bigg] + \frac{C_2}{\kappa}(\ln(1+z) + \ln z_0)
\end{aligned}
\qquad (52)
$$

2.2.2.2 *Secondary flow velocity in the upper half*

In the upper half domain ($0 \le z \le 1$), we obtain:

$$\frac{\mathrm{d}}{\mathrm{d}z}\left(\kappa(1-z)\frac{\mathrm{d}v_1}{\mathrm{d}z}\right) = \frac{1}{\beta}\left[a-\left(1+\frac{\ln(1-z)}{\ln z_0}\right)^2\right]$$
$$= \frac{1}{\beta}\left[a-1-2\frac{\ln(1-z)}{\ln z_0}-\frac{(\ln(1-z))^2}{(\ln z_0)^2}\right] \quad (53)$$

The above differential equation describes the velocity distribution of the secondary flow v_1 in the upper half domain. Integrating the above equation concerning z, we obtain:

$$\kappa(1-z)\frac{\mathrm{d}v_1}{\mathrm{d}z} = \frac{1}{\beta}\left[(-a+1)(1-z)+2\frac{(1-z)\ln(1-z)-(1-z)}{\ln z_0}\right.$$
$$\left.+\frac{(1-z)(\ln(1-z))^2-2(1-z)\ln(1-z)+2(1-z)}{(\ln z_0)^2}\right]+C_4$$
$$= \frac{1}{\beta}\left[\left(-a+1-\frac{2}{\ln z_0}-\frac{2}{(\ln z_0)^2}\right)(1-z)\right.$$
$$+\left(\frac{2}{\ln z_0}-\frac{2}{(\ln z_0)^2}\right)(1-z)\ln(1-z)$$
$$\left.+\frac{(1-z)(\ln(1-z))^2}{(\ln z_0)^2}\right]+C_4 \quad (54)$$

where C_4 is an integral constant determined by the boundary condition at the ceiling and the matching conditions between the solutions in the upper and lower half domains. As already explained, the above equation describes the shear stress due to the secondary flow. Dividing the above equation by $\kappa(1-z)$, we obtain:

$$\frac{\mathrm{d}v_1}{\mathrm{d}z} = \frac{1}{\kappa\beta}\left[\left(-a+1-\frac{2}{\ln z_0}+\frac{2}{(\ln z_0)^2}\right)+\left(\frac{2}{\ln z_0}-\frac{2}{(\ln z_0)^2}\right)\ln(1-z)+\frac{(\ln(1-z))^2}{(\ln z_0)^2}\right]$$
$$+\frac{C_4}{\kappa(1-z)} \quad (55)$$

This equation is further integrated to be

$$v_1 = \frac{1}{\kappa\beta}\left[\left(a - 1 + \frac{4}{\ln z_0} - \frac{6}{(\ln z_0)^2}\right)(1-z) - \left(\frac{2}{\ln z_0} - \frac{4}{(\ln z_0)^2}\right)(1-z)\ln(1-z) - \frac{(1-z)(\ln(1-z))^2}{(\ln z_0)^2}\right] + \frac{C_4}{\kappa}\ln(1-z) + C_5 \quad (56)$$

where C_5 is another integral constant determined by the boundary condition ($v(1-z_0) = 0$). We find

$$C_5 = -\frac{1}{\kappa\beta}\left(a - 4 + \frac{8}{\ln z_0} - \frac{6}{(\ln z_0)^2}\right)z_0 + \frac{C_4}{\kappa}\ln z_0 \quad (57)$$

Substituting the above equation into (56), we obtain

$$v_1 = \frac{1}{\kappa\beta}\left[\left(a - 1 + \frac{4}{\ln z_0} - \frac{6}{(\ln z_0)^2}\right)(1-z) - \left(\frac{2}{\ln z_0} - \frac{4}{(\ln z_0)^2}\right)(1-z)\ln(1-z) - \frac{(1-z)(\ln(1-z))^2}{(\ln z_0)^2} - \left(a - 4 + \frac{8}{\ln z_0} - \frac{6}{(\ln z_0)^2}\right)\right] - \frac{C_4}{\kappa}(\ln(1-z) - \ln z_0) \quad (58)$$

2.2.2.3 *Matching the Solutions in the lower and upper half domains*

At the depth center of the channel ($z = 0$), the shear stresses (48) and (54) should be continuous. Therefore, we have the relation

$$\frac{1}{\beta}\left(a - 1 - \frac{2}{\ln z_0} - \frac{2}{(\ln z_0)^2}\right) + C_2 = \frac{1}{\beta}\left(-a + 1 - \frac{2}{\ln z_0} + \frac{2}{(\ln z_0)^2}\right) + C_4 \quad (59)$$

The above equation reduces to

$$C_4 = \frac{1}{\beta}\left(2a - 2 - \frac{4}{(\ln z_0)^2}\right) + C_2 \quad (60)$$

The velocities v_1 described by (52) and (58) should be matched at the depth center of the channel ($z = 0$), such that

$$\frac{1}{\beta}\left[a(1-z_0)-1-\frac{4}{\ln z_0}+\frac{6(1-z_0)}{(\ln z_0)^2}\right]-\ C_2\ln z_0$$
$$=\ \frac{1}{\beta}\left[a(1-z_0)-1+4z_0+\frac{4(1-2z_0)}{\ln z_0}-\frac{6(1-z_0)}{(\ln z_0)^2}\right]+\ C_4\ln z_0 \qquad (61)$$

The above equation reduces to

$$C_4\ =\ \frac{1}{\beta}\left(\frac{8z_0-8}{(\ln z_0)^2}-\frac{4z_0}{\ln z_0}\right)-\ C_2 \qquad (62)$$

Solving (60) and (62) for C_2 and C_4, we obtain

$$C_2=\frac{1}{\beta}\left(\frac{4z_0-2}{(\ln z_0)^2}-\frac{2z_0}{\ln z_0}-a+1\right) \qquad (63)$$

and

$$C_4=\frac{1}{\beta}\left(\frac{4z_0-6}{(\ln z_0)^2}-\frac{2z_0}{\ln z_0}+a-1\right) \qquad (64)$$

In the lower half domain and the upper half, we obtain respectively

$$v_1=\frac{1}{\kappa\beta}\left[\left(a-1-\frac{4}{\ln z_0}-\frac{6}{(\ln z_0)^2}\right)(1+z)+\left(\frac{2}{\ln z_0}+\frac{4}{(\ln z_0)^2}\right)(1+z)\ln(1+z)\right.$$
$$-\frac{(1+z)(\ln(1+z))^2}{(\ln z_0)^2}+\left(1-a-\frac{2z_0}{\ln z_0}+\frac{4z_0-2}{(\ln z_0)^2}\right)(\ln(1+z)-\ln z_0) \qquad (65)$$
$$\left.-\left(a-\frac{6}{(\ln z_0)^2}\right)z_0\right]$$

$$v_1=\frac{1}{\kappa\beta}\left[\left(a-1+\frac{4}{\ln z_0}-\frac{6}{(\ln z_0)^2}\right)(1-z)-\left(\frac{2}{\ln z_0}-\frac{4}{(\ln z_0)^2}\right)(1-z)\ln(1-z)\right.$$
$$-\frac{(1-z)(\ln(1-z))^2}{(\ln z_0)^2}-\left(a-1-\frac{2z_0}{\ln z_0}+\frac{4z_0-6}{(\ln z_0)^2}\right)(\ln(1-z)-\ln z_0) \qquad (66)$$
$$\left.-\left(a-4+\frac{8}{\ln z_0}-\frac{6}{(\ln z_0)^2}\right)z_0\right]$$

Figure 4 shows the secondary flow velocity distribution due to the combination of Equation (65) and Equation (66). The plot is non-dimensional, the z-direction is represented along the vertical left axis and the secondary flow velocity varies along the horizontal bottom axis. The velocity distribution takes a quasi-symmetric shape "Z" and reveals the increase of z_0 rises the local maximum near-bed v_1 and its distance from the boundary. Positive and negative values indicate that the flow goes toward the outer and inner wall, respectively.

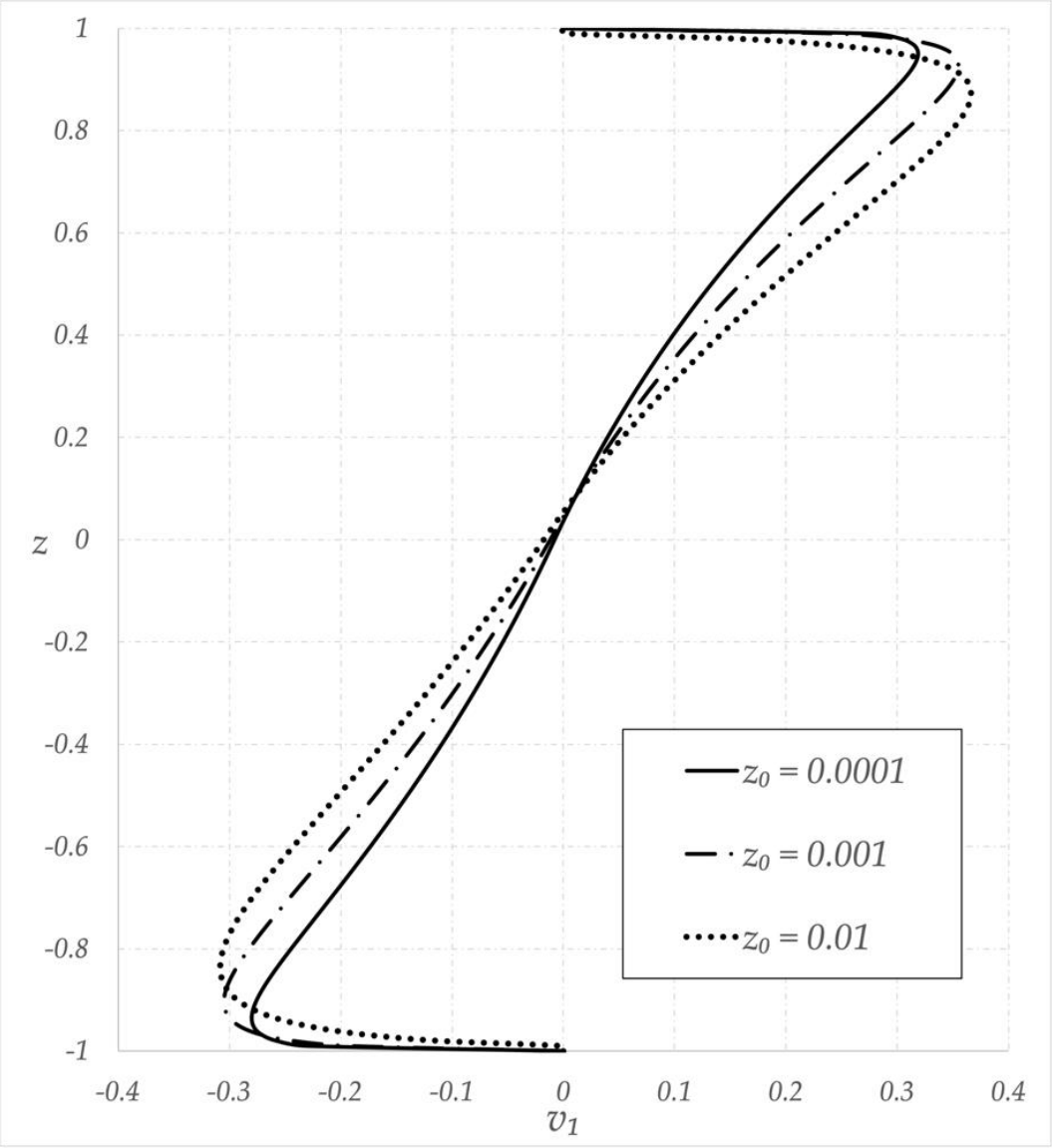

Figure 4: Non-dimensional secondary velocity distribution along the vertical.

2.2.3 Determination of the lateral gradient of the pressure "a"

In addition, the integration of the secondary flow from the bottom to the water surface has to vanish, such that

$$\int_{-1}^{1} v_1 \, \mathrm{d}z = \int_{-1}^{0} v_1 \, \mathrm{d}z + \int_{0}^{1} v_1 \, \mathrm{d}z = 0 \qquad (67)$$

Integrating (65) in the lower half domain ($-1 \le z \le 0$), we obtain

$$\int_{-1}^{0} v_1 \, \mathrm{d}z = \frac{1}{\kappa\beta}\left[\left(\frac{3}{2} - z_0 + \ln z_0\right)a - \left(\frac{3}{2} - 2z_0 + \ln z_0\right) - \frac{1/2 + 2z_0}{\ln z_0} - \frac{9/4 - 2z_0}{(\ln z_0)^2}\right] \qquad (68)$$

Integrating (66) in the upper half domain ($0 \le z \le 1$), we obtain

$$\int_{0}^{1} v_1 \, \mathrm{d}z = \frac{1}{\kappa\beta}\left[\left(\frac{3}{2} - z_0 + \ln z_0\right)a - \left(\frac{3}{2} - 2z_0 + \ln z_0\right) - \frac{7/2 + 6z_0}{\ln z_0} - \frac{41/4 - 10z_0}{(\ln z_0)^2}\right] \qquad (69)$$

Substituting (68) and (69) into (67), we obtain

$$\left[(3 - 2z_0 + 2\ln z_0)a - (3 - 4z_0 + 2\ln z_0) - \frac{4 + 8z_0}{\ln z_0} - \frac{50/4 - 12z_0}{(\ln z_0)^2}\right] = 0 \qquad (70)$$

This condition determines another unknown a. The result is

$$a = \frac{3 - 4z_0 + 2\ln z_0}{3 - 2z_0 + 2\ln z_0} + \frac{4 + 8z_0}{(3 - 2z_0 + 2\ln z_0)\ln z_0} + \frac{50/4 - 12z_0}{(3 - 2z_0 + 2\ln z_0)(\ln z_0)^2} \qquad (71)$$

2.2.4 Depositional morphology

Suppose we supply a sufficient amount of sediment in the channel, the sediment deposits and covers part of the channel bed. Denoting the height of the depositional surface by η, and the half flow depth by D, which are both normalized by the original half depth D_0^*, we have the relation:

$$2D = 2 - \eta \; or \; D = 1 - \frac{1}{2}\eta \tag{72}$$

The flow domain is now $-1 + \eta < z < 1$. To project this physical flow domain in the imaginary domain $-1 < \zeta < 1$, we employ the coordinate transformation of the form:

$$\zeta = \frac{z - \frac{\eta}{2}}{D} \tag{73}$$

From the above equation, we obtain the following differential relation:

$$\mathrm{d}z = D \, \mathrm{d}\zeta \tag{74}$$

The depositional surface is $z = -1 + \eta$, and therefore, the flow depth (distance from the depositional surface to the ceiling) is $2 - \eta$, the half-depth is $1 - \frac{\eta}{2}$, and the depth center locates where $z = \frac{\eta}{2}$, corresponding to $\zeta = 0$.

We assume that the effect of the bed (depositional surface) is dominant in the lower part half domain $-1 + \eta \leq z \leq \frac{\eta}{2}$, corresponding to $-1 \leq \zeta \leq 0$. As the distance from the depositional surface to the height z is $z + 1 - \eta$, the eddy viscosity is expressed in the form

$$\nu_{T0} = \kappa^2 (1 + z - \eta)^2 \frac{\mathrm{d}u_0}{\mathrm{d}z} \tag{75}$$

Using the new vertical coordinate ζ and the differential relation $\mathrm{d}z = D \, \mathrm{d}\zeta$, we can rewrite the above equation into the form

$$\nu_{T0} = \kappa^2 \frac{\left(1 - \frac{\eta}{2} + D\,\zeta\right)}{D} \frac{\mathrm{d}u_0}{\mathrm{d}\zeta} \tag{76}$$

Because $1 - \frac{\eta}{2} = D$, the above reduces to

$$\nu_{T0} = \kappa^2 D (1+\zeta)^2 \left|\frac{\mathrm{d}u_0}{\mathrm{d}\zeta}\right| \tag{77}$$

Substituting the above equation into (18) with ν_T replaced with ν_{T0}, and transform z into ζ, we obtain

$$\kappa^2 (1+\zeta)^2 \left|\frac{\mathrm{d}u_0}{\mathrm{d}\zeta}\right| \frac{\mathrm{d}u_0}{\mathrm{d}\zeta} = C_f \tag{78}$$

We find that the above equation is identical to (21) with z replaced with ζ. Therefore, the solution of the above equation is

$$u_0 = 1 - \frac{\ln(1+\zeta)}{\ln \zeta_0} \tag{79}$$

Where ζ_0 is now $\frac{z_0}{D}$.

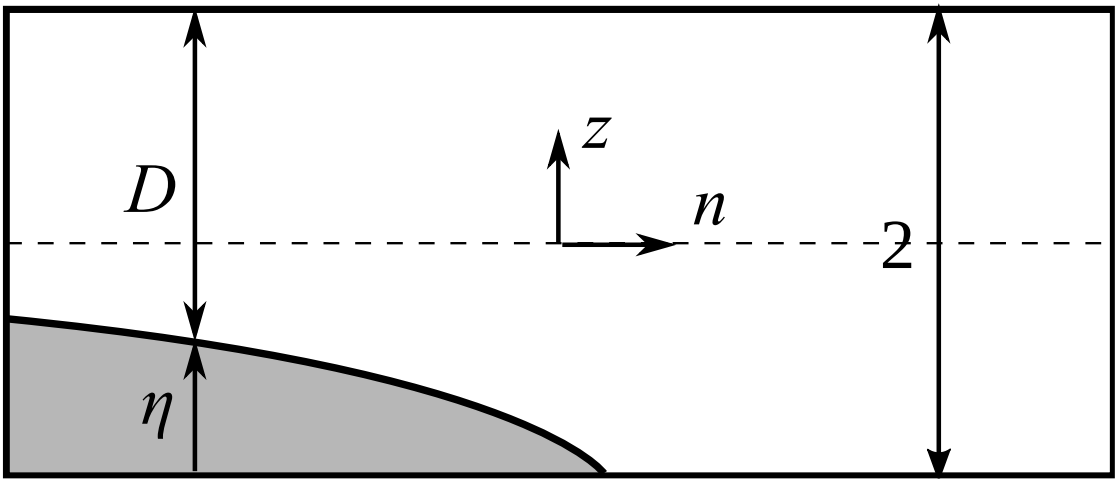

Figure 5: Definitions of non-dimensional variables describing the cross-section

In the upper half domain ($0 \leq \zeta \leq 1$), we assume that the effect of the ceiling is dominant. The distance from the ceiling to the height z is $1 - z$, and therefore, we have the relation

$$\nu_{T0} = \kappa^2 (1-z)^2 \left|\frac{\mathrm{d}u_0}{\mathrm{d}z}\right| \tag{80}$$

With the use of the new vertical coordinate ζ , we can rewrite the above equation in the form

$$\nu_{T0} = \kappa^2 \frac{\left(1 - D\zeta - \frac{n}{2}\right)^2}{D} \left|\frac{\mathrm{d}u_0}{\mathrm{d}\zeta}\right| \tag{81}$$

Because $1 - \frac{\eta}{2} = D$, the above equation reduces to

$$\nu_{T0} = \kappa^2 D (1-\zeta)^2 \left|\frac{\mathrm{d}u_0}{\mathrm{d}\zeta}\right| \tag{82}$$

Substituting the above equation into (18), we obtain:

$$\kappa^2 (1-\zeta)^2 \left|\frac{\mathrm{d}u_0}{\mathrm{d}\zeta}\right| \frac{\mathrm{d}u_0}{\mathrm{d}\zeta} = C_f \tag{83}$$

We also find the above equation is identical to (29) with z replaced with ζ. Therefore, we find the solution of the form:

$$u_0 = 1 + \frac{\ln(1-\zeta)}{\ln \zeta_0} \tag{84}$$

where again $\zeta_0 = \frac{z_0}{D}$.

The solution in the whole domain is

$$u_o = \begin{cases} 1 - \dfrac{\ln(1+\zeta)}{\ln \zeta_0}, & (-1 \le \zeta \le 0) \\ 1 + \dfrac{\ln(1-\zeta)}{\ln \zeta_0}, & (0 \le \zeta \le 1) \end{cases} \tag{85}$$

In the lower half domain $(-1 \le \zeta \le 0)$, substituting (79) into (77), we obtain

$$\nu_{T0} = \kappa^2 D (1+\zeta) \tag{86}$$

Substituting the above equation into (44) and applying the coordinate transformation (73), we obtain

$$\frac{\partial}{\partial\zeta}\left[\kappa^2(1+\zeta)\frac{\partial v_1}{\partial\zeta}\right]=\frac{D}{\beta}\left(a-u_0^2\right) \tag{87}$$

Therefore, the secondary flow is written in the form

$$v_1 = D\mathcal{V}_1^l(\zeta) \tag{88}$$

where ϑ_1^l is the solution of (65) with z and z_0 replaced with ζ and ζ_0, respectively. Similarly, the secondary flow in the upper half domain is

$$v_1 = D\mathcal{V}_1^u(\zeta) \tag{89}$$

where ϑ_1^u is the solution of **Error! Reference source not found.** with z and z_0 replaced w ith ζ and ζ_0, respectively.

The lateral sediment transport q_n is described by

$$q_n = q_s\left(\frac{v_{1b}}{u_{0b}}+\frac{r}{\beta\theta^{\frac{1}{2}}}\frac{\partial\eta}{\partial n}\right) \tag{90}$$

where q_s is the sediment transport rate in the s direction, u_{0b} and v_{1b} are the u_0 and v_1 evaluated near the bed at the height of the sediment particle, r is a coefficient standing for the effect of the bed slope in lateral direction, and θ is the non-dimensional bed shear stress. r is in the range 0.5 – 0.6 approximately [53]. Previous studies [29,54,55] showed that the coefficient r is theoretically described by:

$$r = \frac{1+\alpha\mu}{\lambda\mu}\theta_c^{\frac{1}{2}} \tag{91}$$

where α is the ratio between the lift and the drag forces, μ is the Coulomb friction factor, λ is the sheltering factor, and θ_c is the non-dimensional critical bed shear stress. When the

values of α, μ, λ and θ_c are assumed to be 0.85, 0.43, 0.59, and 0.05 respectively [56], r is calculated to be 0.597.

In the equilibrium state, the lateral sediment transport rate q_n vanishes. Thus, (90) reduces to

$$\frac{\mathrm{d}\eta}{\mathrm{d}n} = \frac{\beta\theta^{\frac{1}{2}}}{r}\frac{v_{1b}}{u_{0b}} \tag{92}$$

The non-dimensional bed shear stress θ is defined by

$$\theta = \frac{u_*^2}{R_s g D_s^*} = \frac{C_f U_a^{*2}}{R_s g D_s^*} \tag{93}$$

Where U_a^* is the depth-averaged velocity as already explained, R_s is the submerged specific gravity $\left(= \frac{\rho_s}{\rho} - 1 = 1.65\right)$, g is the gravity acceleration $\left(= 9.8\,\frac{m}{s^2}\right)$, and D_s^* is the sediment diameter.

We evaluate the flow velocity acting on the sediment particle at the center height of the particle $D_s^*/2$. If we assume that the dimensional roughness height k_s^* is identical to the sediment size D_s^*, the evaluation height $\frac{D_s}{2}$ normalized by the initial half-depth D_o^* is $\frac{k_s}{2}$. Because $z_0 = \frac{k_s}{30}$, we find $D_s/2 = 15\,z_0$. As ζ_0 depends on D, ζ_0 changes in the lateral direction. Since the change in the flow depth is relatively small, we assume that ζ_0 is constant in the lateral direction. As a result, we have the relations

$$v_{1b} = D\mathcal{V}_1^l(-1 + 15\zeta_0),\ u_{0b} = u_0(-1 + 15\zeta_0) \tag{94}$$

Substituting the above relations into (92), we obtain the following equation:

$$\frac{\mathrm{d}\eta}{\mathrm{d}n} = M\left(1 - \frac{1}{2}\eta\right) \tag{95}$$

where

$$M = \frac{\beta\ \theta^{\frac{1}{2}}\ \vartheta_1^l(-1+15\zeta_0)}{r\ u_0(-1+15\zeta_0)} \tag{96}$$

Integrating (95) from $\eta(n_0) = 0$ to $\eta(n)$, we obtain

$$\eta(n) = 2\left[1 - e^{-\frac{1}{2}M(n-n_0)}\right] \tag{97}$$

where n_0 is the coordinate where the deposition begins.

2.3 Results

Overall, under bedload sediment transport, Equation (97) implies that the average transverse bed slope mainly depends on two main factors: the sediment deposition limit n_0 and the parameter M. According to Equation (93), various parameters intervene in the second factor M such as the bed roughness z_0, the channel geometry (channel aspect ratio - β), the near-bed flow dynamics (friction coefficient – C_f, bed shear stress – θ, flow velocities ratio – $\mathcal{V}_1^l/u_0$).

The analysis of Equation (97) reveals that, for $n < n_0$, the transverse bed slope surface η is always positive. The flow velocities ratio is negative near the bed ($\mathcal{V}_1^l/u_0 \leq 0$), implying that M is negative. In addition, the term $n - n_0$ is always positive, and Equation 97 converges and is positive. In contrast, η becomes 0 whenever $n \geq n_0$. Meaning that the transverse bed slope reaches its maximum near the inner wall, decreases towards the outer wall and becomes null beyond $n = n_0$. It makes sense that the sediment is deposited along the inner wall because near the bottom, the flow goes from the outer wall to the inner wall, and there is no sediment deposit between the outer wall and n_0.

Figure 6 shows the transverse bed profile graphs with different values of n_0. With the increasing distance n_0 from the inner wall, the transverse bed slope appears to decrease slightly.

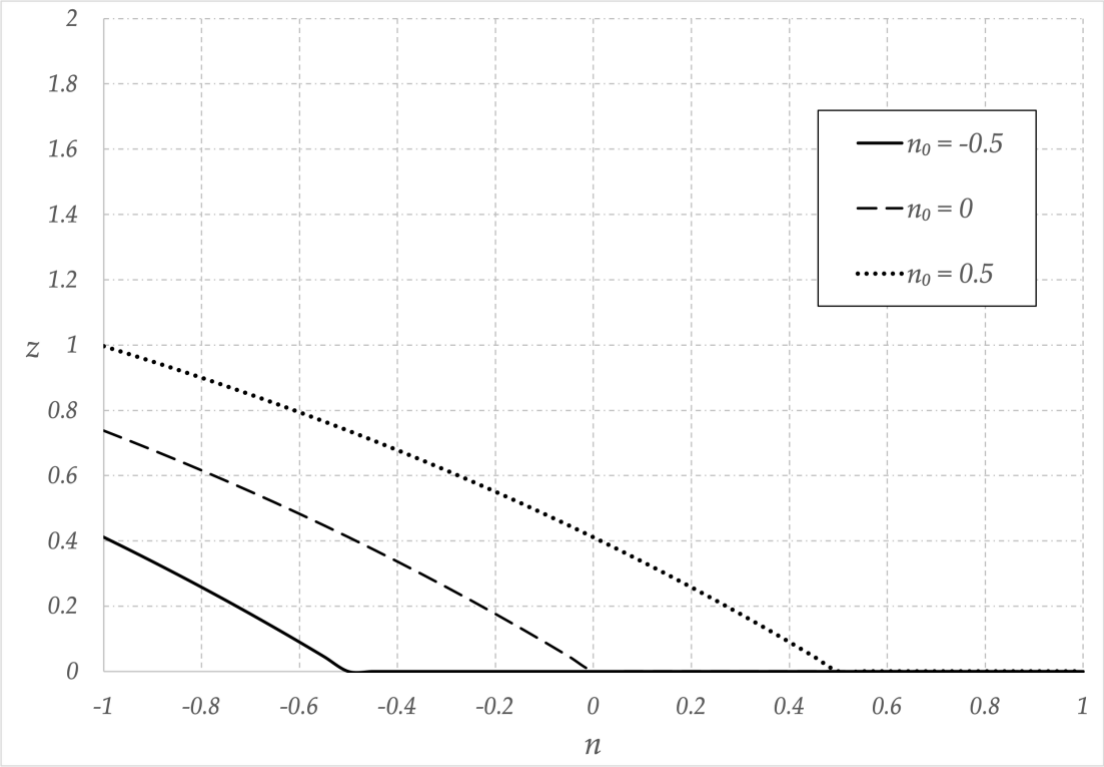

Figure 6: Analytical cross-sections of the sediment deposition η, according to Equation (97), depending on the values of the start of the sediment deposition n_0 along the radial coordinate.

The fluctuation of the transverse bed slope as a function of the parameter M is shown in Figure 7 to Figure 10. Equation (97) indicates that the transverse bed slope flattens as M decreases.

Figure 7 displays a group of transverse bed slope graphs plotted with two different depth-averaged flow velocities (U_a^*) and three values of bed roughness z_0. The transverse slope angle appears to increase when the depth-averaged flow velocity grows.

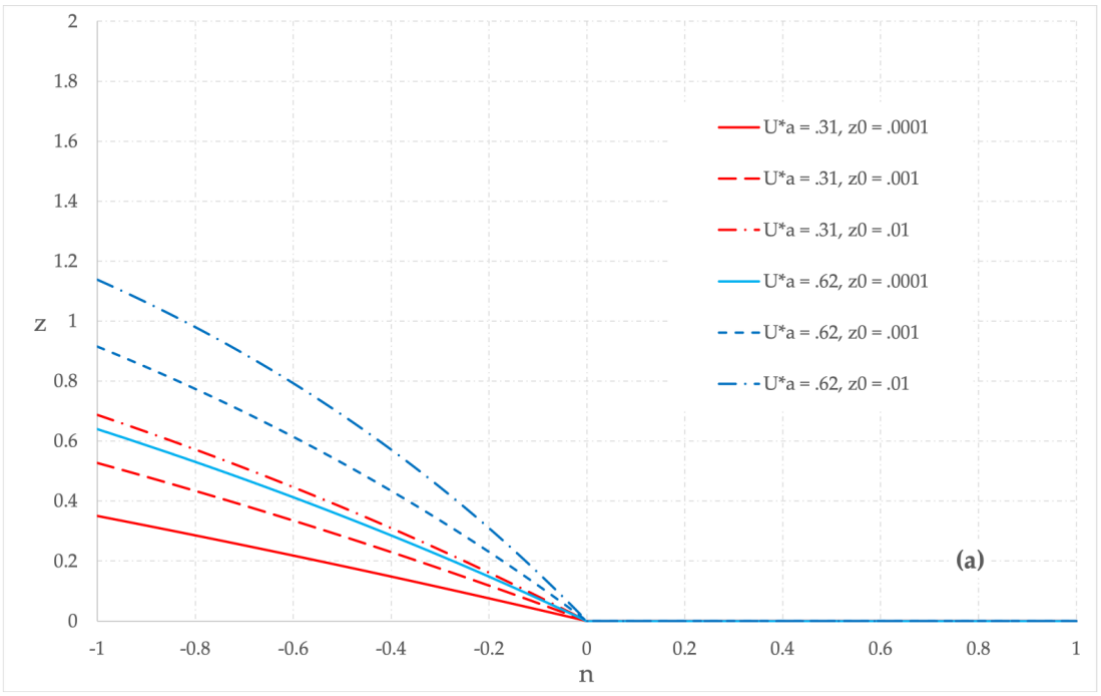

Figure 7: Analytical cross-sections of the sediment deposition η, according to Equation (97), depending on the values of (a) U_a^* and z_0.

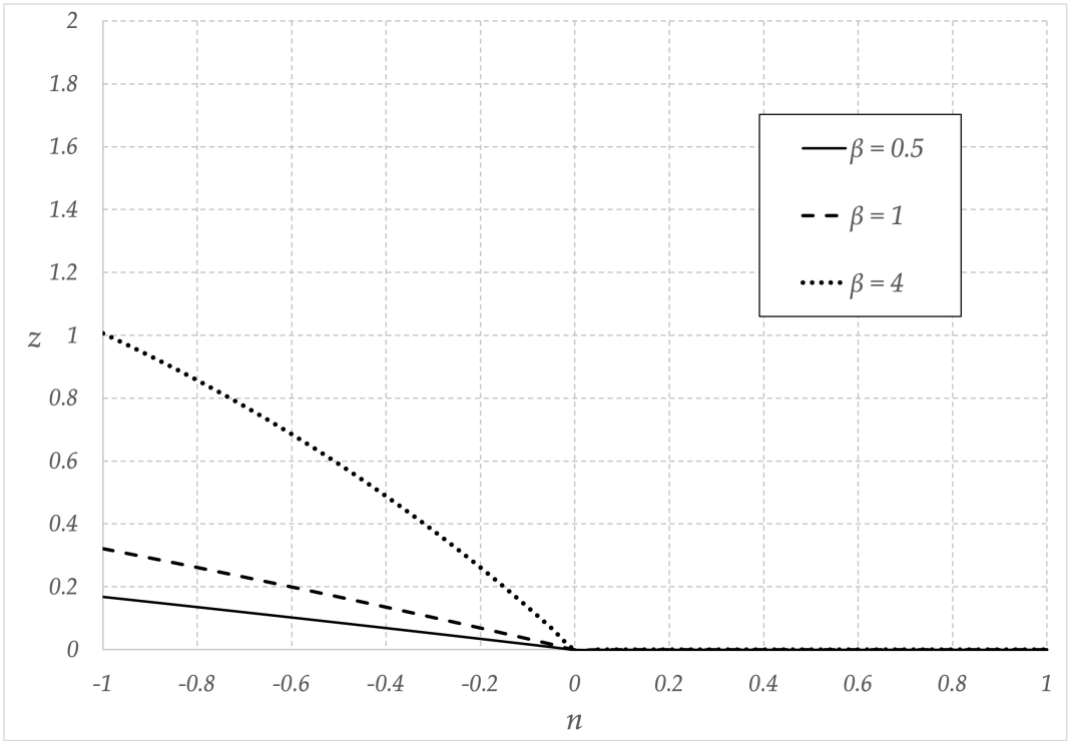

Figure 8: Analytical cross-sections of the sediment deposition η, according to Equation (97), as a function of the the channel aspect ratio β.

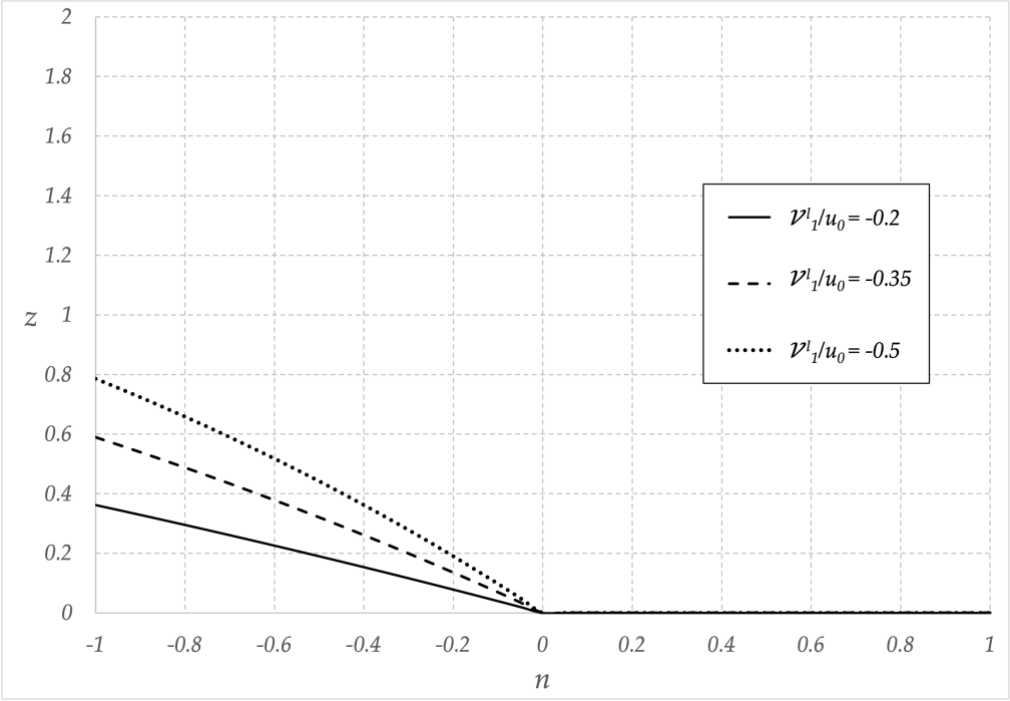

Figure 9: Analytical cross-sections of the sediment deposition η, according to Equation (97), depending on the near bed flow $\vartheta_1^I/u_{0'}$.

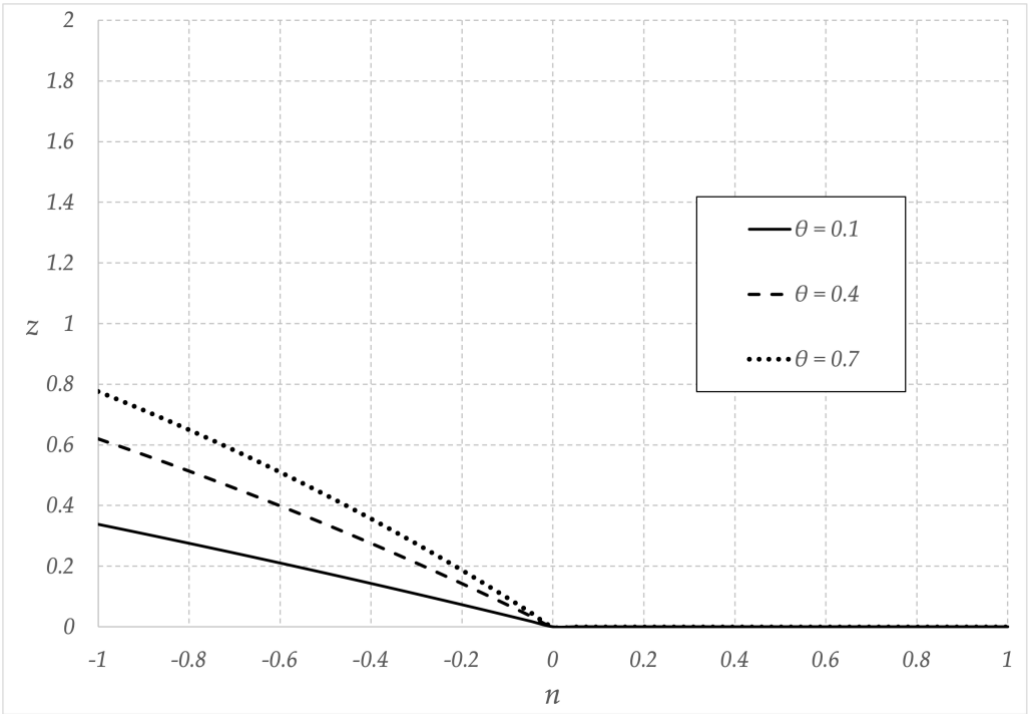

Figure 10: Analytical cross-sections of the sediment deposition η, according to Equation (97), as a function of the bed shear stress θ.

3 Bed Configurations in Mixed Bedrock-Alluvial in Uniformly Curved Channels

3.1 Materials and Methods

The experiments use an annular flume, similarly to the work conducted by Taguchi et al. [32,33], but with different cover lid rotation speeds: 40 RPM and 48 RPM. Each experiment with different lid rotation speeds is referred to as Case 1 and Case 2, respectively. We use the plaster model of the bedrock for simulation purposes and we use different rotation speeds of the cover lid.

3.1.1 Annular flume

We conducted the experiments in an annular flume made of plexiglass, the cover lid of metal for better stability, and the plate in contact on the water surface is also made of plexiglass. as seen in Figure 11. Figure 12 shows the schematic diagram of the annular flume.

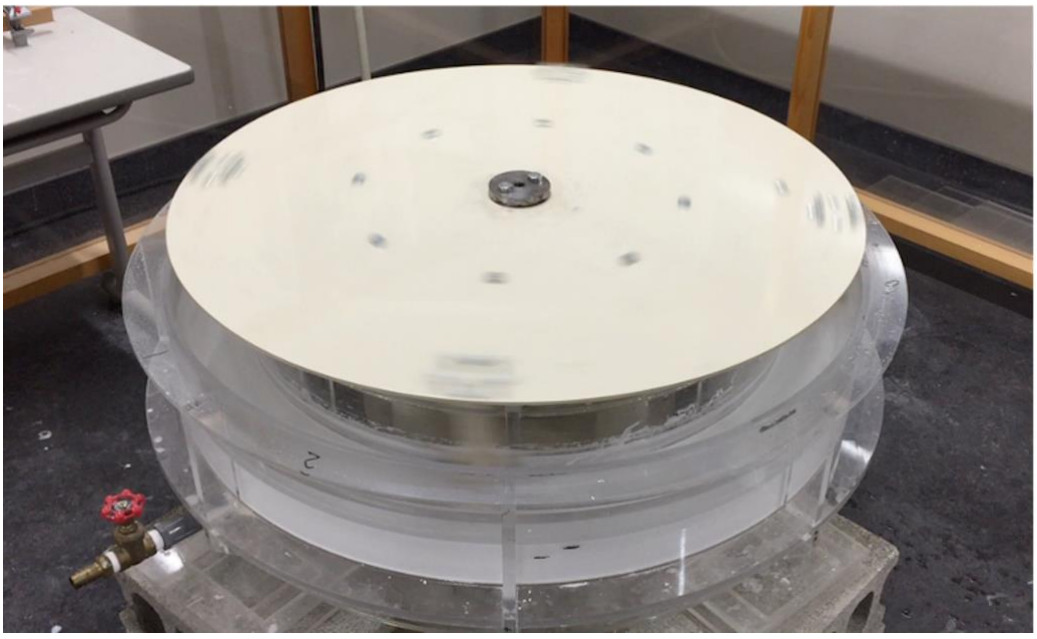

Figure 11: Photo of the annular flume with the white plaster.

It has a rectangular cross-section with a half-width $B^* = 50$ mm, and a maximum depth $H^*\max = 180$ mm, and a radius at the centerline of $R_c^* = 450$ mm. We adjusted the cover lid

to have $D_0^* = 25$ mm of the water column. The rotation of the cover lid on the water column permitted the flow to generate inside the flume.

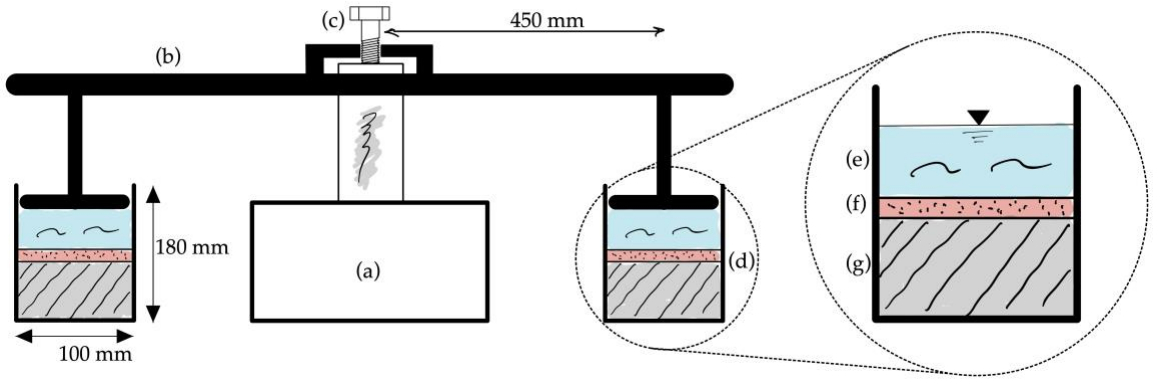

Figure 12: Schematic diagram of the cross section of the annular flume and the original bed configuration inside the flume channel. (a) electrical motor, (b) cover lid, (c) lever for the cover lid plate to obtain the desired water depth, (d) flume channel, (e) 50 mm of water depth, (f) 2.5 kg of sediment, (g) 6 cm of plaster, a mixture of gypsum powder and water.

3.1.2 Bed materials

We used plaster, a mixture of gypsum and water, as bedrock. We used the HS-650® gypsum provided by Noritake Co., Ltd., Nagoya, Japan. [57]. After the mixing process, the plaster was poured into the flume and was left for 12 h, then the excess water was pumped out, and the plaster was left to cure for 24 h. The amount of plaster used in our studies was such that it reached a thickness d = 60 mm. Plaster was used because it is easier and faster to prepare than mortar [32–34,58]. In addition, plaster has a lower resistance against erosion[59]. For Case 1 and Case 2, the plaster mixtures were 1:2 and 1:2.5 by weight of gypsum and water, respectively. It means that the bedrock in Case 2 was slightly softer than in Case 1. Regardless, the bedrock preparation was identical for both cases.

As sediment, 2.5 kg of sand was used. It is a natural sand (No. 5® provided by Tohoku Keisya Co., Ltd.) and it has a diameter $D_s^* = 0.45\ mm$ with a density of $\rho_s = 2.61 \frac{g}{cm^3}$. Its grain-size distribution curve is presented in Figure 13 [60]. The sand was painted red to contrast the bedrock with the sediment [32,33]. The sediment was dispersed on the bed surface before each start, as uniformly as possible. Water was then poured carefully into the

flume to avoid the possibility of sediment disruption and any damage to the bed surface due to the water jet. For these reasons, the pouring flow was kept as low as possible, and the water was passed through a small-screen sponge. In our experiments, the water depth was 50 mm, and any excess water was removed for safety reasons.

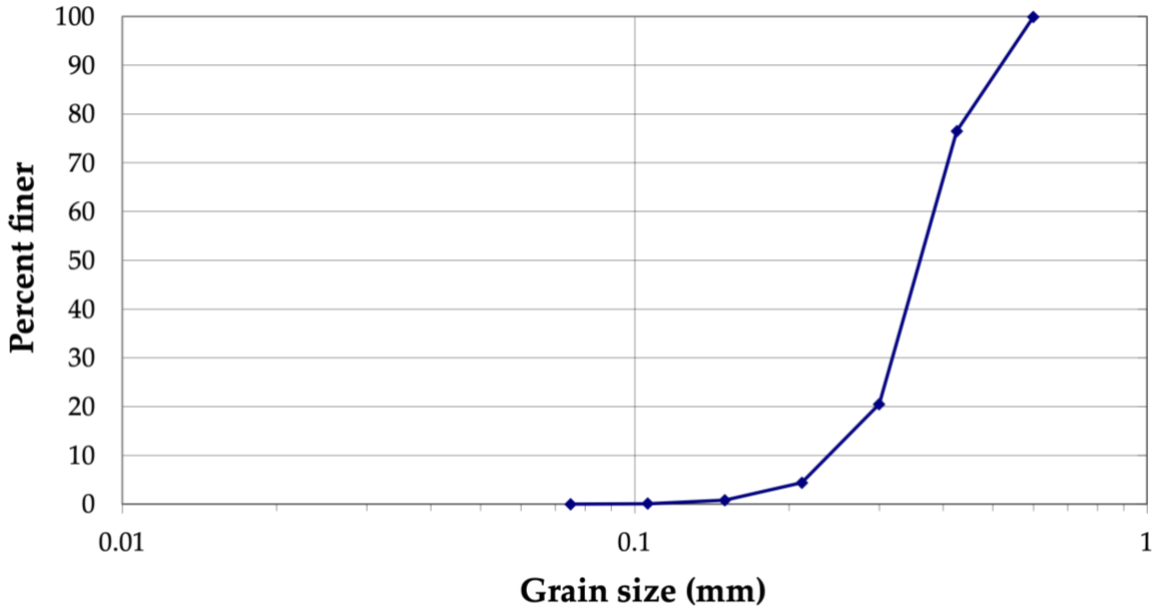

Figure 13: Grain - size distribution curve of the sand No.5® used during the experiments [60]

3.2 Experimental conditions and data acquisition

As previously stated, two experimental cases were conducted. In Case 1, the rotation speed was 40 RPM of top lid rotation, and in Case 2, it was 48 RPM. The studies by Taguchi et al. [32,33] were used as a guide for the speed in Case 1, and in Case 2 the aim was simply to investigate the higher rotation speed effects on the erosion. The amount of sediment remained constant throughout the experiments, and the sediment transport was kept to bedload transport, which was checked visually at the start of each experiment.

We ran the experiments within specified timesteps (Table 1). After each timestep, the bed surface topography was surveyed twice. First, the bed surface with the sediment coverage (WS) was surveyed, and then the bed surface without the sediment coverage (NS) was done.

Table 1. Experimental conditions and resultant bed formation.

	Timestep	Δt [1]	T [2]	Speed [3]	α [4]	W [5]	Bedforms, Number of Wavelengths (k)
Case 1	1	1/12	0	40	23–24	26	Uniform transform slope
	2	3	3	40	8–37	41	5 bedforms
	3	3	6	40	16–28	34	5 bedforms
	4	6	12	40	15–38	37	6 bedforms
	5	12	24	40	15–61	24	8 bedforms
	6	24	48	40	18–55	33	9 bedforms
Case 2	1	1/12	0	48	20–30	20	Uniform transform slope
	2	3	3	48	12–33	24	12 bedforms
	3	3	6	48	15–31	22	12 bedforms
	4	6	12	48	21–26	17	Uniform transform slope
	5	12	24	48	20–26	17	Uniform transform slope
	6	24	48	48	20–22	17	Uniform transform slope
	7	24	72	48	20–27	18	Uniform transform slope
	8	12	84	40	12–38	34	6 bedforms

[1] Δt: the timestep's duration, in hours (h); [2] T: the cumulative time, in hours (h); [3] Speed: the annular flume top lid rotation speed, in rounds per minute (RPM); [4] α: the transverse slope angle, in degrees (°); [5] W: the transverse slope base sweep width, in millimeters (mm).

We used laser scanning to measure the topography of the bed surface. However, the scanning equipment was different for the two cases: Case 1 used a Keyence CMOS Multi-Function Analog Laser Sensor, whereas Case 2 used an Artec EVA 3D scanner. The Sensor head IL-300 was utilized with the Keyence CMOS Multi-Function Analog Laser Sensor and was placed above the bed surface at a distance of 300 mm to provide the optimal precision of 0.5 mm [34]. Similar to the studies of Taguchi et al. [32,33], the bed surface was surveyed circumferentially at every 50 mm from the inner wall side. The 3D scanner Artec EVA of Artec 3D was operated at a 500–600 mm distance from the bed surface to provide better resolution. It has a resolution of up to 0.2 mm [61]. Contrary to the Keyence IL 300 Laser Sensor, the bed surface and the flume were surveyed and provided complete and continuous topography data.

3.3 Data processing and calculation

The measured data were in (x^*, y^*, z^*) format, representing the relative bed elevation of the bed surface in the cartesian coordinates system. It is then changed into a curvilinear coordinates system $(s^*,\ n^*, z^*)$ or (s, n, z) for visual convenience. The tangential and radial coordinates (s, n) are respectively defined by the following:

$$n = R^* - R_c^* \tag{98}$$

$$s = R_c^* * \theta \qquad (99)$$

where R_c^* is the radius at the centerline of the flume, which is 450 mm, $R^* = \sqrt{x^{*2} + y^{*2}}$ is the radius, and $\theta = tan^{-1}(y^*/x^*)$. Hence, in non-dimensional form, $s = [0, 18] * \pi$; and $n = [-1, 1]$. The negative values of n indicate the half side near the inner wall of the annular flume. In contrast, the positive ones represent the half near the outer wall, and 0 is the flume centerline. Note that -1 represents the inner wall side, and 1 represents the outer wall.

3.3.1 Transverse slope

We generated cross-section profiles for each timestep from the bed surface topographical map. We measured the width and the depth of the inner channel along those sections, denoted as Be and He, respectively (Figure 14).

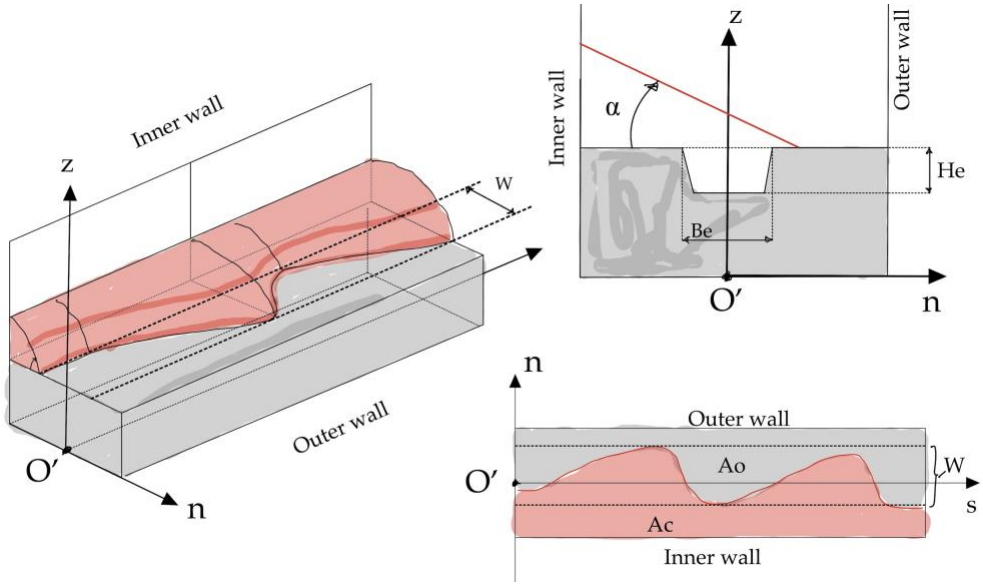

Figure 14: Schematic diagrams of the bed configurations and parameters definition. The sediment coverage is colored in red; the bedrock is gray (left). The corresponding plan and section views are on the upper right and bottom right, respectively

Photos of the bed surface are presented in Figure 15. We also retrieved the profile data from the 18 transverse sections distant by π, presented in Figure 16 and Figure 17. The average erosion rate (Em) is obtained by dividing the difference between the sequential bed surface and the original bed surface by the duration.

3.3.2 Sweep width

The sweep width, denoted as W, was defined as the bedrock surface area inside which the transverse slope base undulates (Figure 14). This sweep width is also retrieved from these cross-section profiles. The difference between the minimum and maximum radial coordinates of the transverse slope base on the bedrock surface defines it.

3.3.3 Fraction of exposed bed

The fraction of the exposed bed, denoted as Po, was calculated by analyzing the topographical map of the bed surface. First, we generated the sediment thickness maps. Then the spatial analysis tools implemented in ArcGIS [62] were used to delineate and calculate the areas of the exposed bed (Ao) and the sediment coverage (Ac) (Figure 14). To differentiate the sediment coverage to the exposed bed, we applied a criteria value of 0.02 on the sediment thickness map, which is the diameter of the grain. Values below 0.02 were considered to represent the exposed bed, and higher values were considered sediment coverage. The following formula can be used to describe Po, according to the study of Sklar and Dietrich [13]:

$$P_0 = A_0/(A_0 + A_c) \qquad (100)$$

3.4 Results

The sediment deposition patterns with the corresponding transverse slope profiles and the evolution of the bedrock incision were determined for Case 1 and Case 2. Figure 15 shows two photos of the resultant bed configurations for Case 1. The bed incision resulted in the formation of an inner channel along the centerline of the flume. The sediment bed coverage constituting the bedforms (red-colored) was deposited along the inner wall, and the exposed bed (white-colored) along the vicinity of the outer wall could be observed (Figure 15, left). Moreover, light and linear scours were also noticed on the exposed bedrock (Figure 15, right).

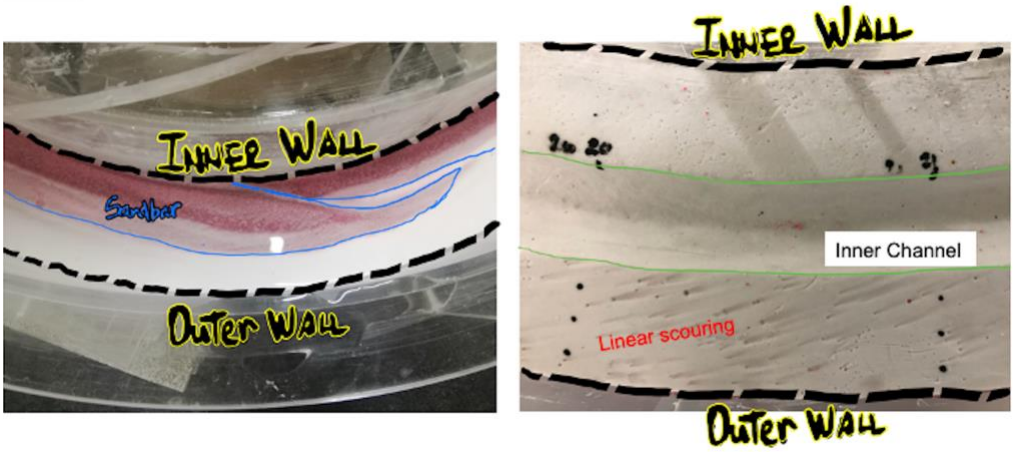

Figure 15: Photos of the bed configuration inside the flume—top view—Case 1 at the end of timestep 6. The white-colored area represents the exposed bed, the reddish part is the sediment coverage (left). The inner channel is visible after removing the sediment coverage, and linear scouring is visible under magnification (right)

3.4.1 Sediment deposition

Figure 16 and Figure 17 show the plan views of the sediment deposition pattern for Case 1 and Case 2, respectively. The figures represent the sediment deposition patterns and height in the annular flume, plotted dimensionless. The timesteps-displays allow to observe the temporal evolution of the bed configurations.

The boundary between the exposed bed and the sediment coverage is located at the limit of the light-blue and light-yellow color; the dashed lines represent the transverse sections for the profiles data for all 18 cross-sections.

The sediment transport inside the flume started soon after the experiment began. Initially, the sediment was dragged toward the inner wall due to the spiral flow and formed a uniform transverse slope along the inner wall. The uniform transverse slope was observed in Case 1 (Figure 16a) and Case 2 (Figure 17a). The sediment generally covered half the flume width.

Gradually, the uniform transverse slope turned into migrating bedforms, depending on the flow dynamic conditions in the flume. For instance, bedforms were observed throughout Case 1, their wavenumber increased, and their shape changed with time (Figure 16 b-f). In

Case 2 , there was minimal evidence of bedforms and the sediment deposition along the inner wall side looked like a uniform transverse slope (Figure 17). There were also six bedforms at timestep 8, when the rotation speed was reduced to 40 RPM (Figure 17 h).

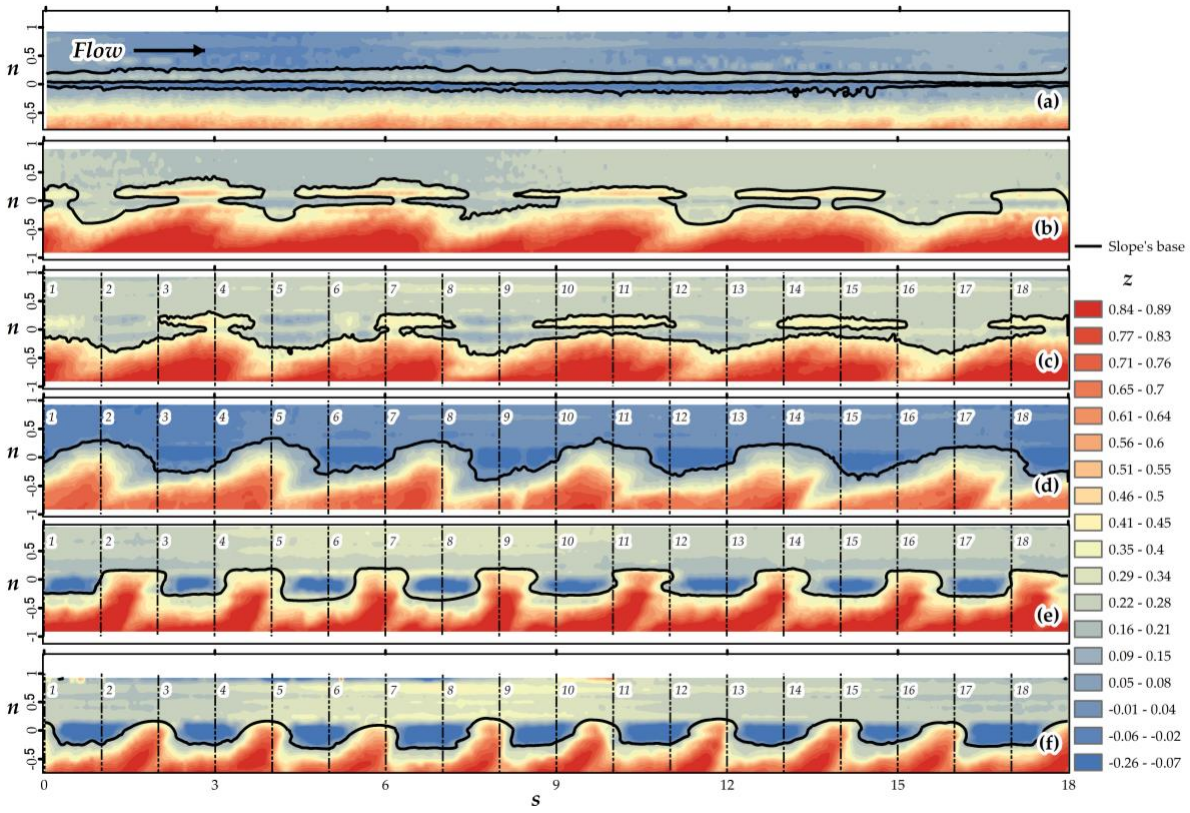

Figure 16: Plan views of the bed configurations - sediment deposition patterns, Case 1 (40 RPM) for all the timesteps: (a) timestep 1 (T = 5 min), (b) timestep 2 (T = 3 h), (c) Timestep 3 (T = 6 h), (d) timestep 4 (T = 12 h), (e) timestep 5 (T = 24 h), and (f) timestep 6 (T = 48 h).

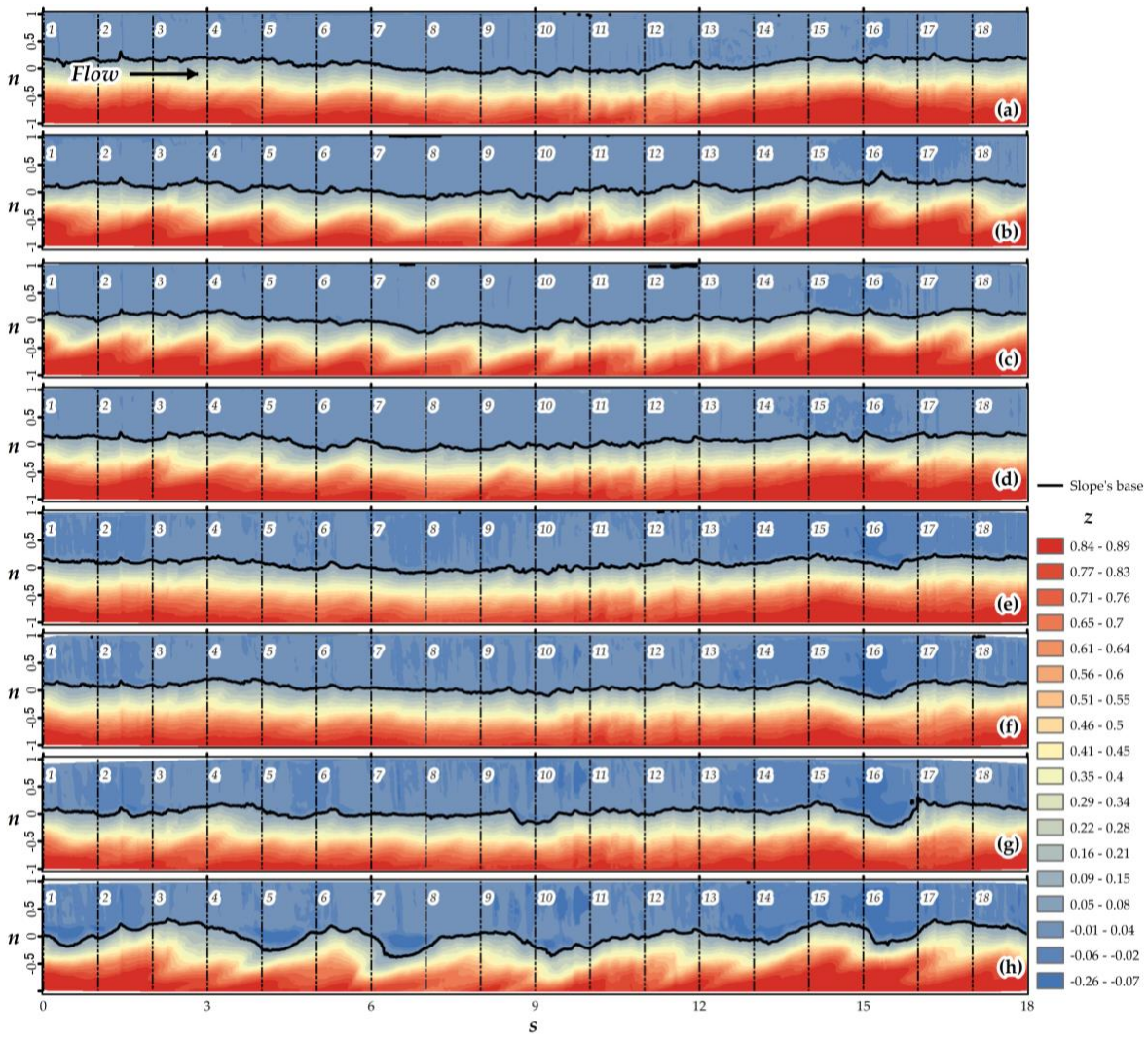

Figure 17: Plan views of the bed configurations - sediment deposition patterns, Case 2 (48 RPM) for all the timesteps: (a) timestep 1 (T = 5 min), (b) timestep 2 (T = 3 h), (c) timestep 3 (T = 6 h), (d) timestep 4 (T = 12 h), (e) timestep 5 (T = 24 h), (f) timestep 6 (T = 48 h), and (g) timestep 7 (T = 72 h); (h) timestep 8 (T = 84 h) but with 40 RPM

3.4.2 Transverse slopes and sweep width

The transverse slope profile sections are displayed in Figure 18 to Figure 23 for Case 1 and Figure 24 to Figure 31 for Case 2. The vertical axis z represents the relative height, non-dimensional, and the horizontal axis n represents the channel width from the inner wall (n = -1) to the outer wall (n = 1), also non-dimensional. The 18 profile sections, announced previously are plotted in gray-colored curves, whereas the average is colored in red. The

transverse slope angle (α) and the transverse slope base sweep width (W) were measured and are reported inTable 1.

The average transverse slopes in both cases are close and vary between 23 and 24 degrees. However, the results revealed that, in Case 2, the transverse slope angle α hardly varies, between 20 and 27 degrees, except at timesteps 2 (Figure 25), 3 (Figure 26), and 8 (Figure 31), where the fluctuation of the angle α became significant, from 12 to 38 degrees. In contrast, in Case 1, the variation of the angle α was significant, from 8 to 61 degrees, as observed in Figure 18 to Figure 24.

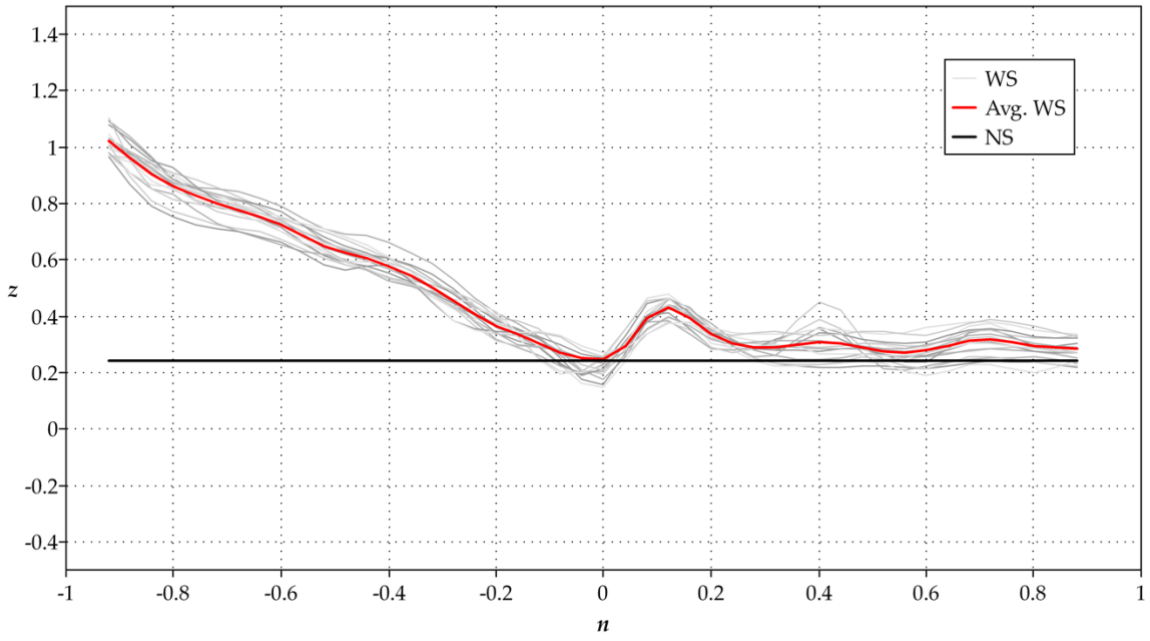

Figure 18: Transverse slope profile sections obtained for each timestep, Case 1 (40 RPM): (a) timestep 1 (T = 5 min).

In addition, with the formation of the bedforms, the sweep width (W) became wider. Case 1 showed well-formed bedforms (long wavelength), and W became wider than 25 mm (Table 1). Contrarily, when the bedforms were poorly formed (short wavelength) or remained as a quasi-uniform transverse slope as in Case 2, W became narrower, at less than 25 mm.

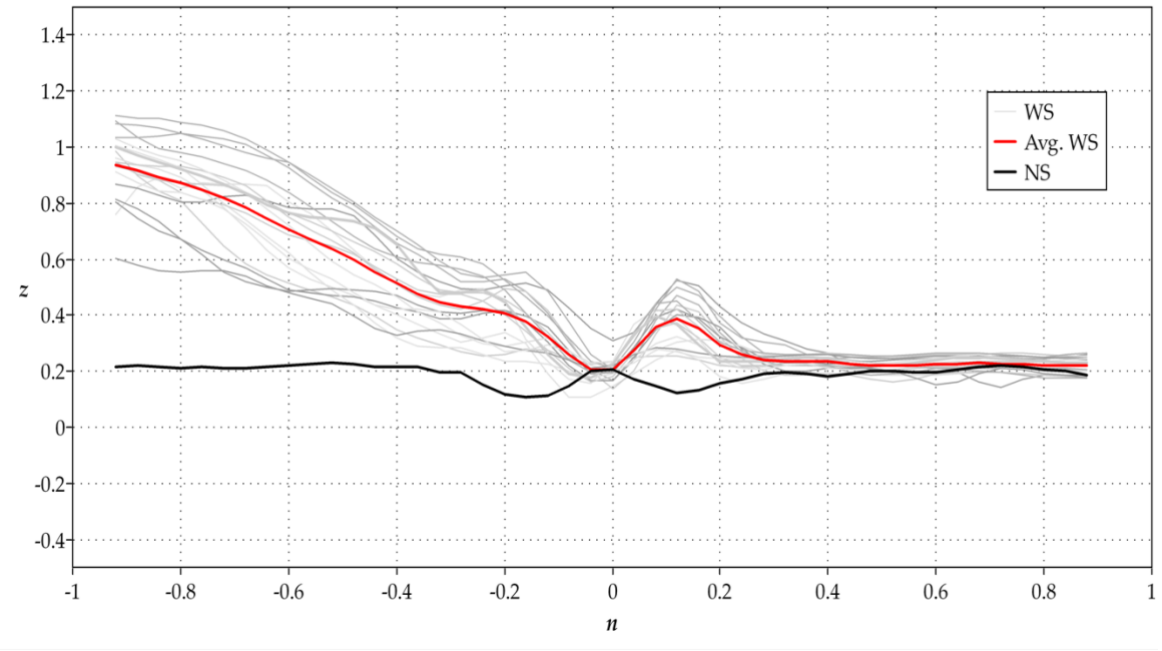

Figure 19: Transverse slope profile sections obtained for each timestep, Case 1 (40 RPM), timestep 2 (T = 3 h).

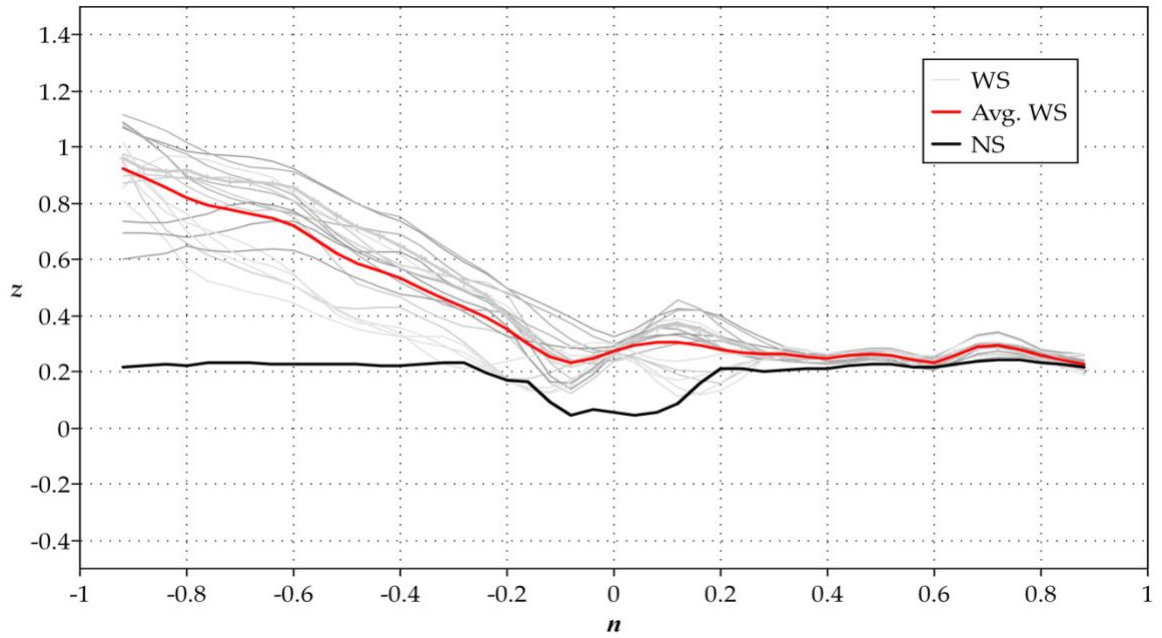

Figure 20: Transverse slope profile sections obtained for each timestep, Case 1 (40 RPM), timestep 3 (T = 6 h).

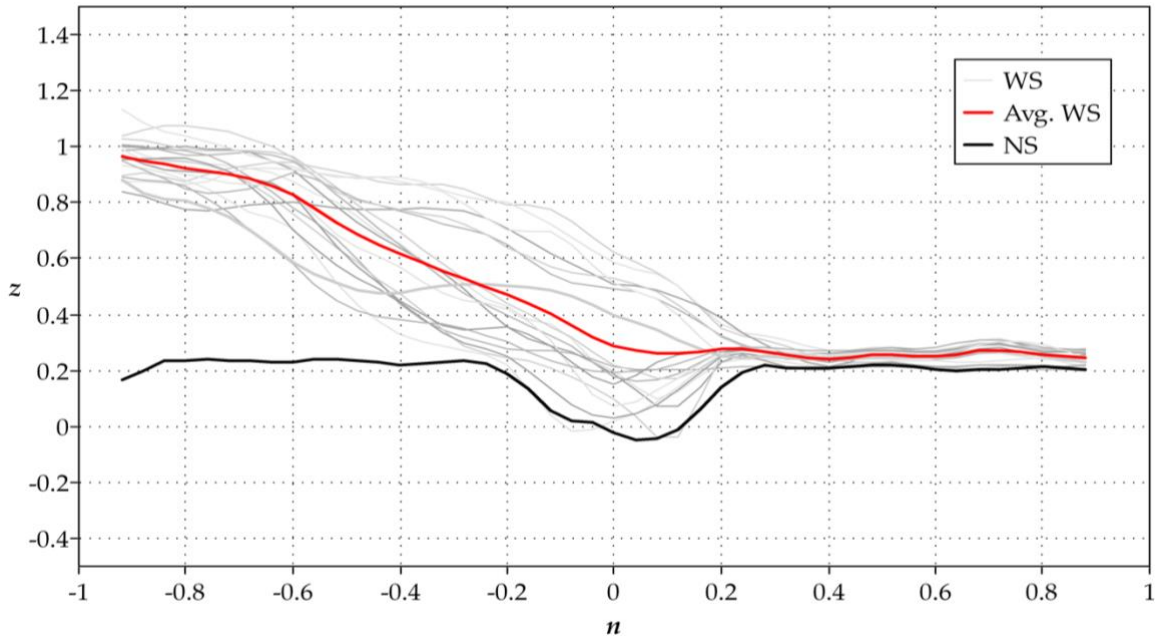

Figure 21: Transverse slope profile sections obtained for each timestep, Case 1 (40 RPM), timestep 4 (T = 12 h).

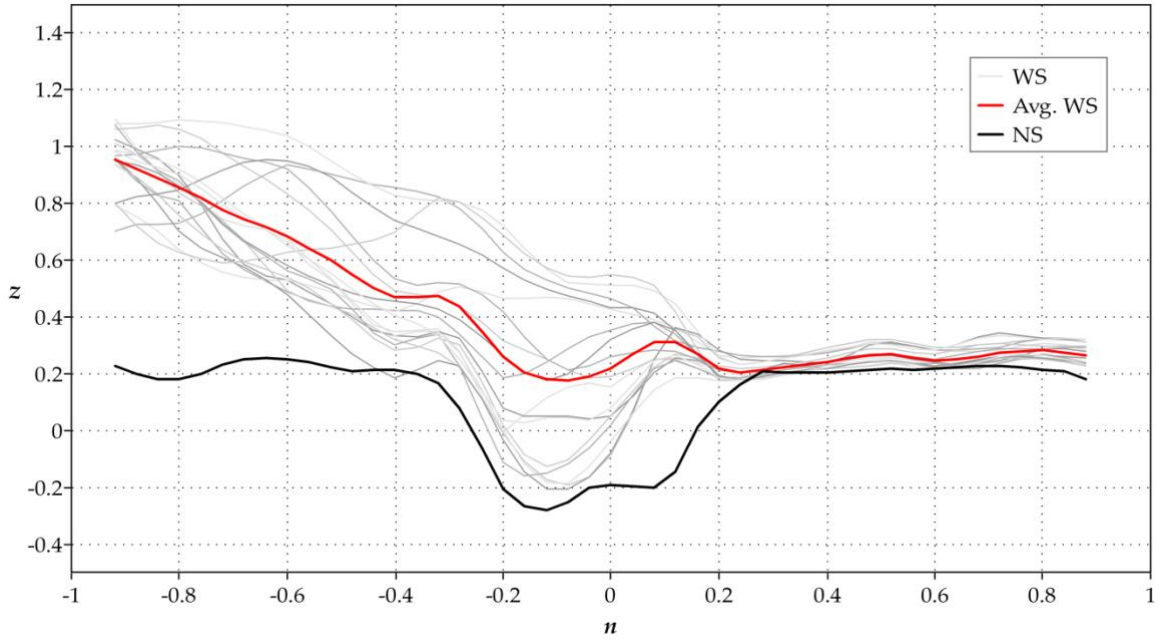

Figure 22: Transverse slope profile sections obtained for each timestep, Case 1 (40 RPM), timestep 5 (T = 24 h).

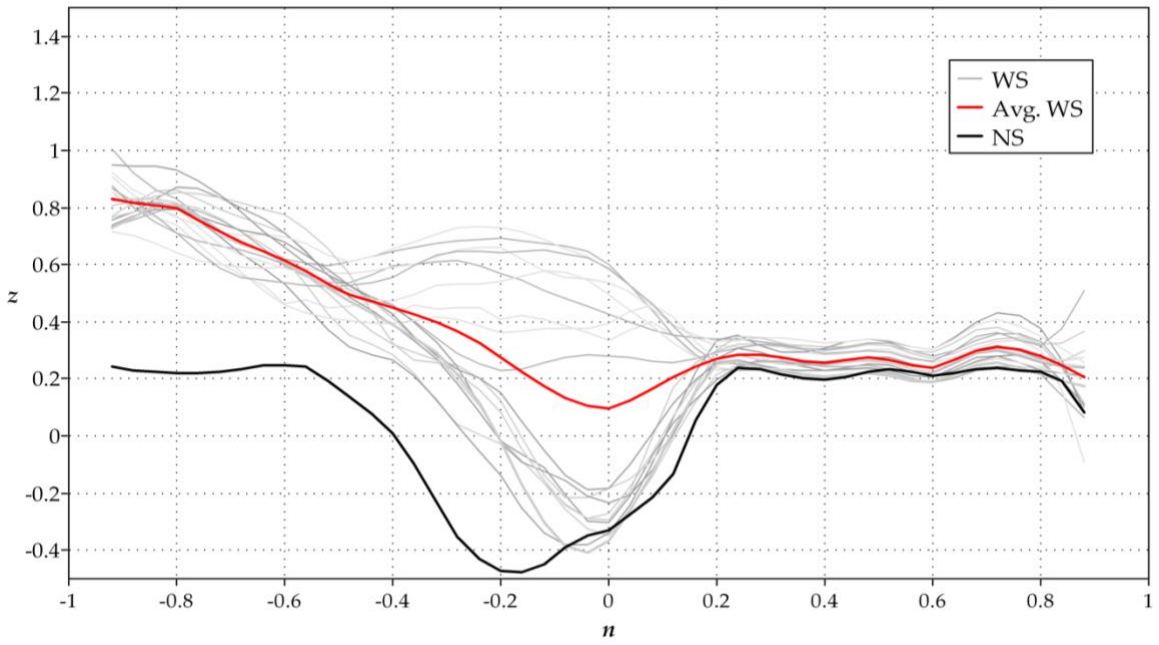

Figure 23: Transverse slope profile sections obtained for each timestep, Case 1 (40 RPM), timestep 6 (T = 48 h).

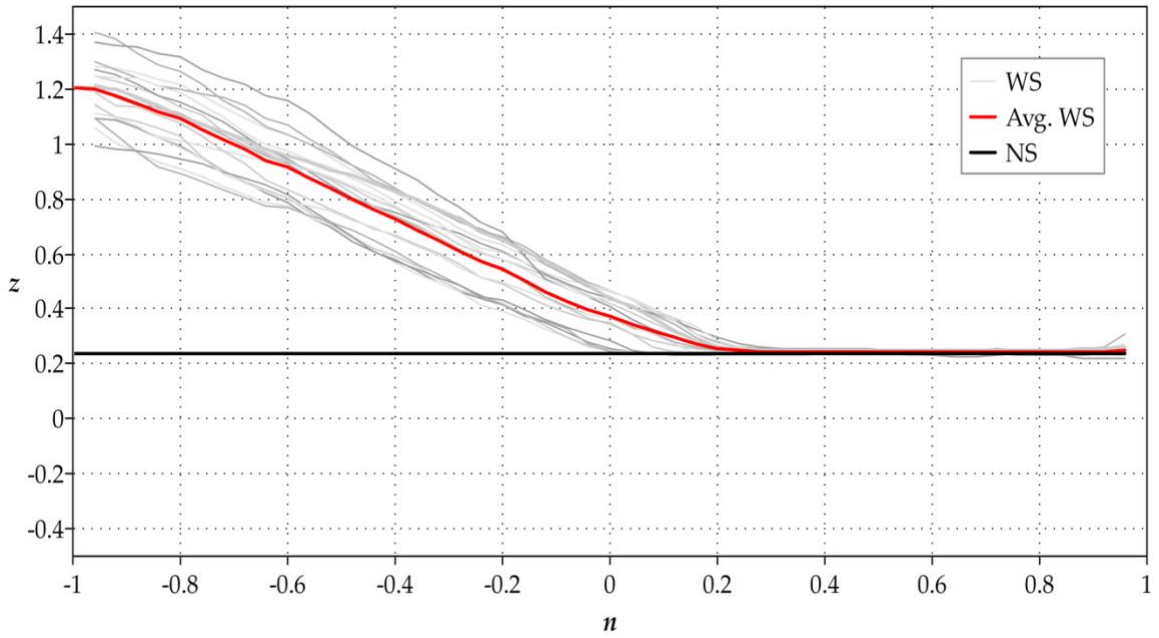

Figure 24: Transverse profile sections obtained for each timestep, Case 2 (48 RPM): timestep 1 (T = 5 min).

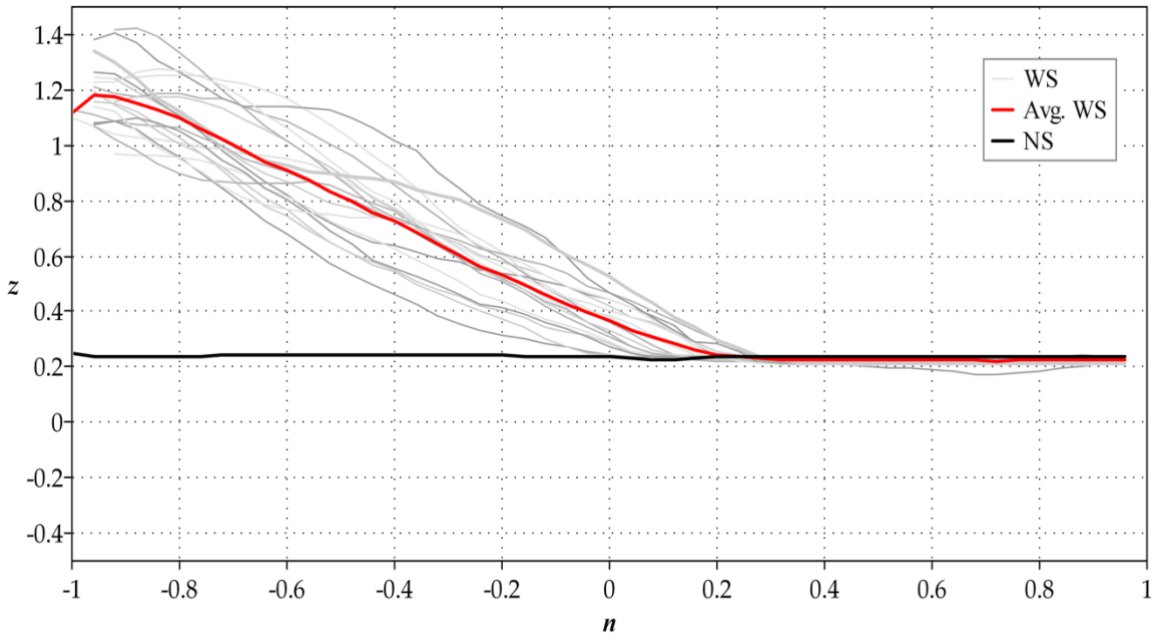

Figure 25: Transverse profile sections obtained for each timestep, Case 2 (48 RPM), timestep 2 (T = 3 h).

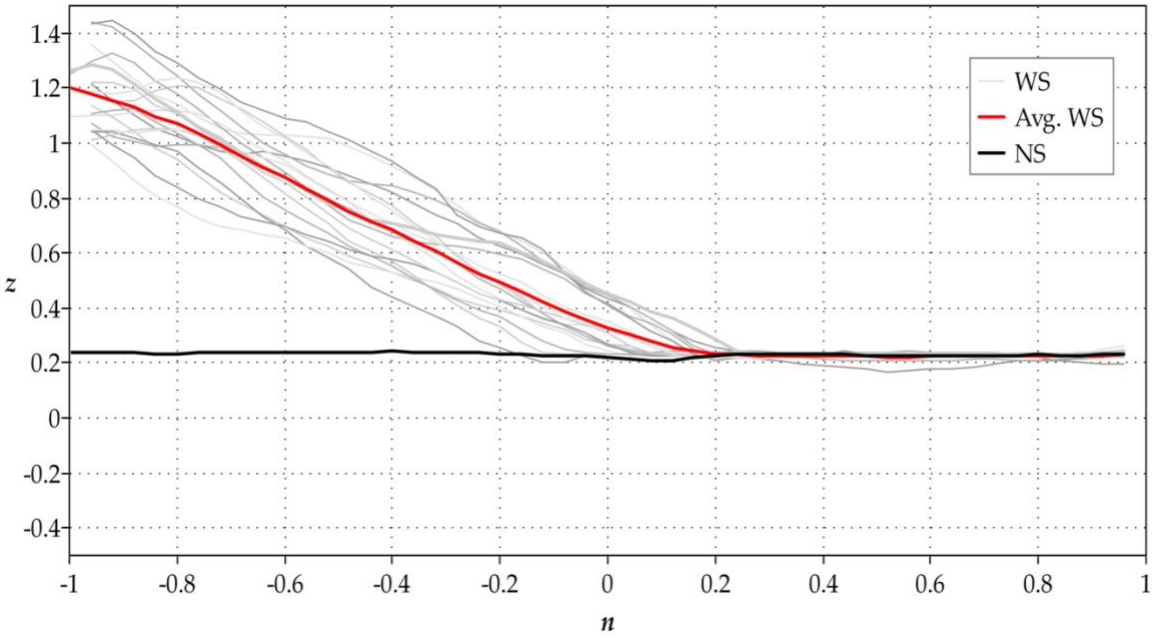

Figure 26: Transverse profile sections obtained for each timestep, Case 2 (48 RPM), timestep 3 (T = 6 h).

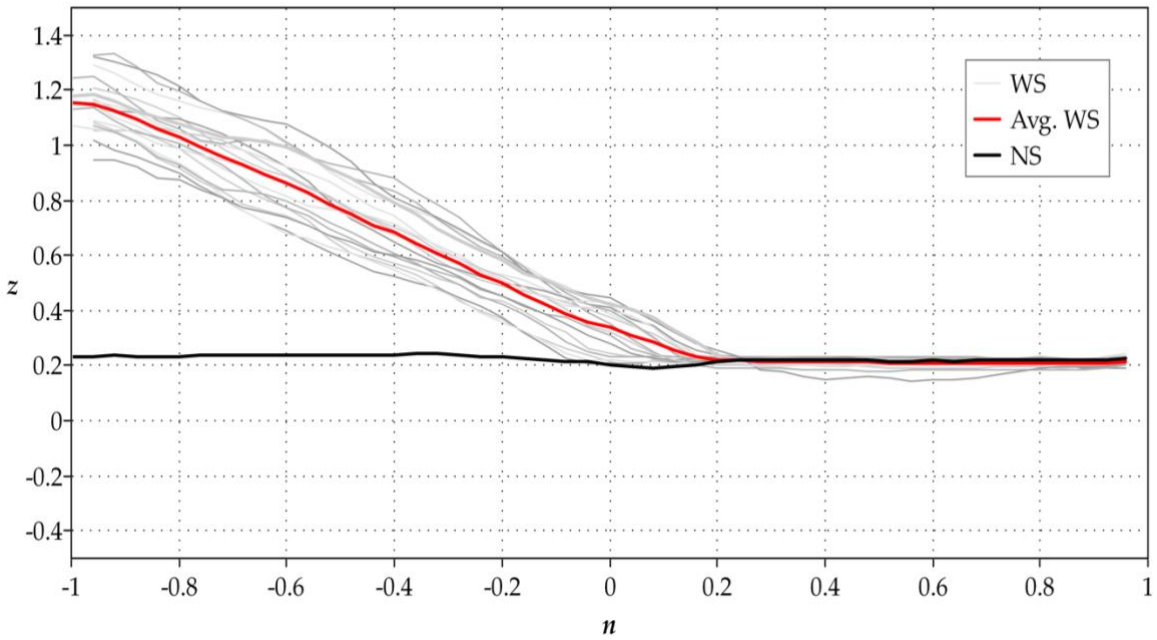

Figure 27: Transverse profile sections obtained for each timestep, Case 2 (48 RPM), timestep 4 (T = 12 h).

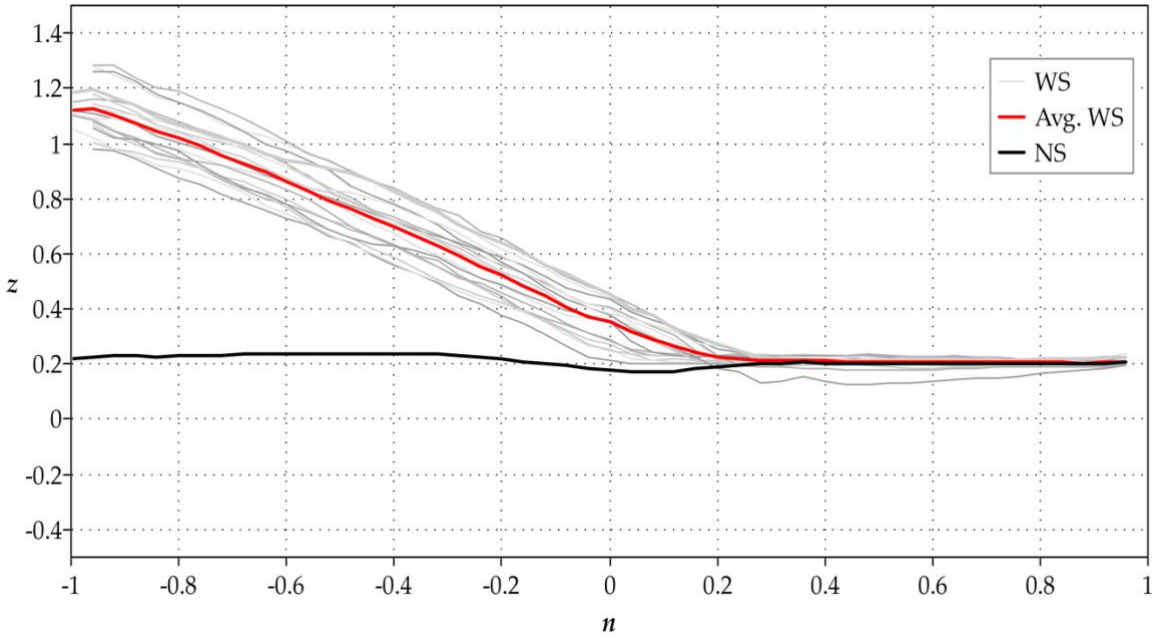

Figure 28: Transverse profile sections obtained for each timestep, Case 2 (48 RPM), timestep 5 (T = 24 h).

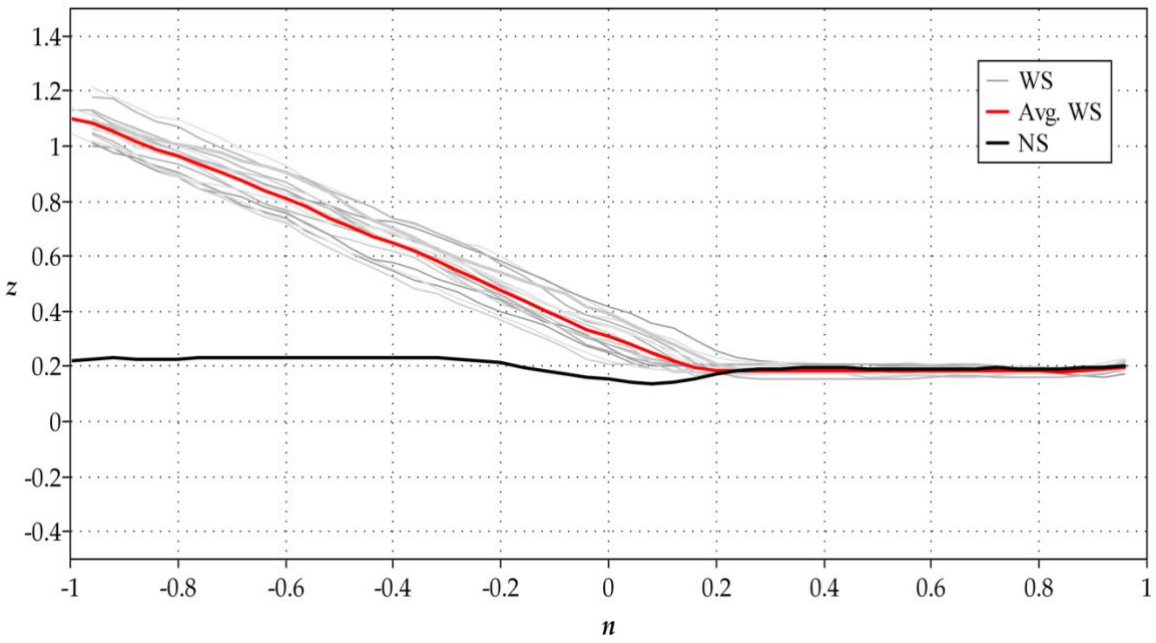

Figure 29: Transverse profile sections obtained for each timestep, Case 2 (48 RPM), timestep 6 (T = 48 h).

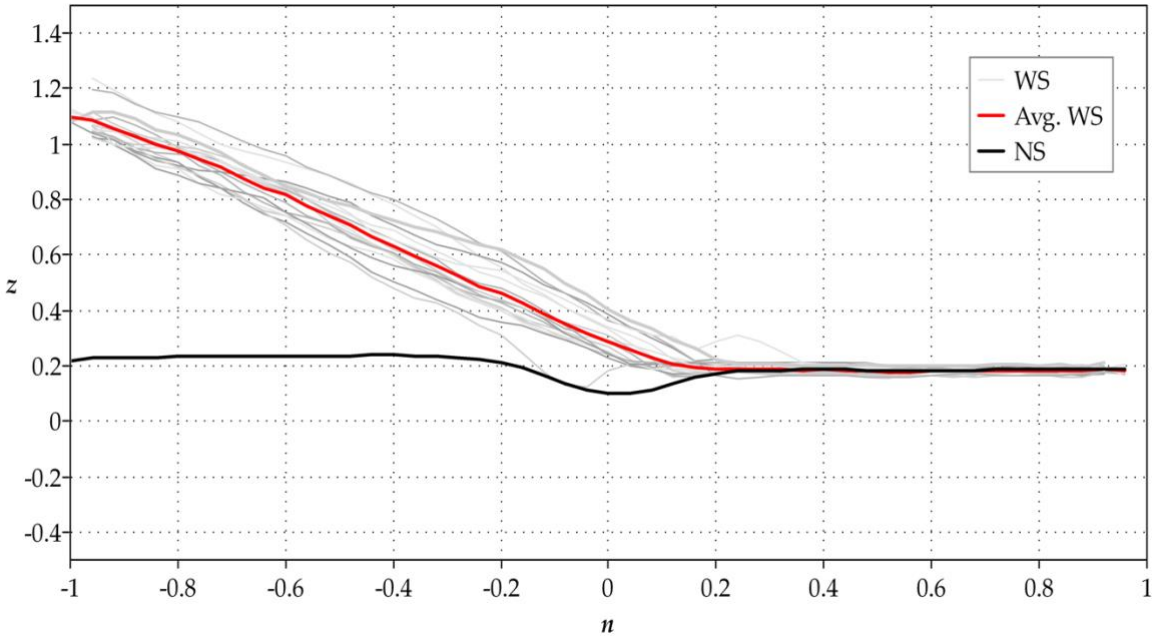

Figure 30: Transverse profile sections obtained for each timestep, Case 2 (48 RPM), timestep 7 (T = 72 h).

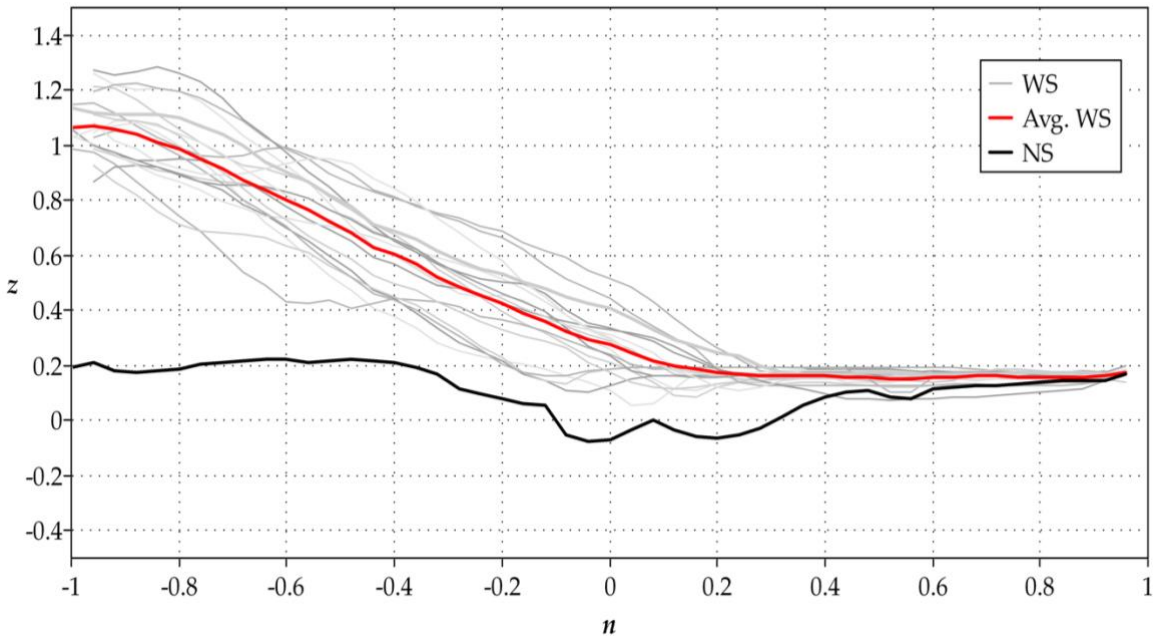

Figure 31: Transverse profile sections obtained for each timestep, Case 2 (48 RPM), timestep 8 (T = 84 h) but with 40 RPM.

3.4.3 Fraction of exposed bed and average erosion

Figure 32 displays the plots of the fraction of exposed bed (Po) and the average erosion rate (Em) over time, revealing a close link between the two: a rise in Po was accompanied by a rise in Em.

In both Case 1 and Case 2, around 45% of the bed surface is exposed at the beginning. Then, until T = 6 h, Em and Po grew and achieved local maxima.

Following that, Em and Po in Case 1 increased, reaching 1.78×10^3 mm^3/h and 56%, respectively, by the end of the experiment T = 48 h. Conversely, in Case 2, Em and Po decreased and stabilized at 4.8×10^3 mm^3/h and 47%, respectively.

The graphs pointed out that, particularly in Case 2, Po increased and reached 52%, leading to a slight increase of Em by the end of the experiment when the rotation speed was reduced to 40 RPM.

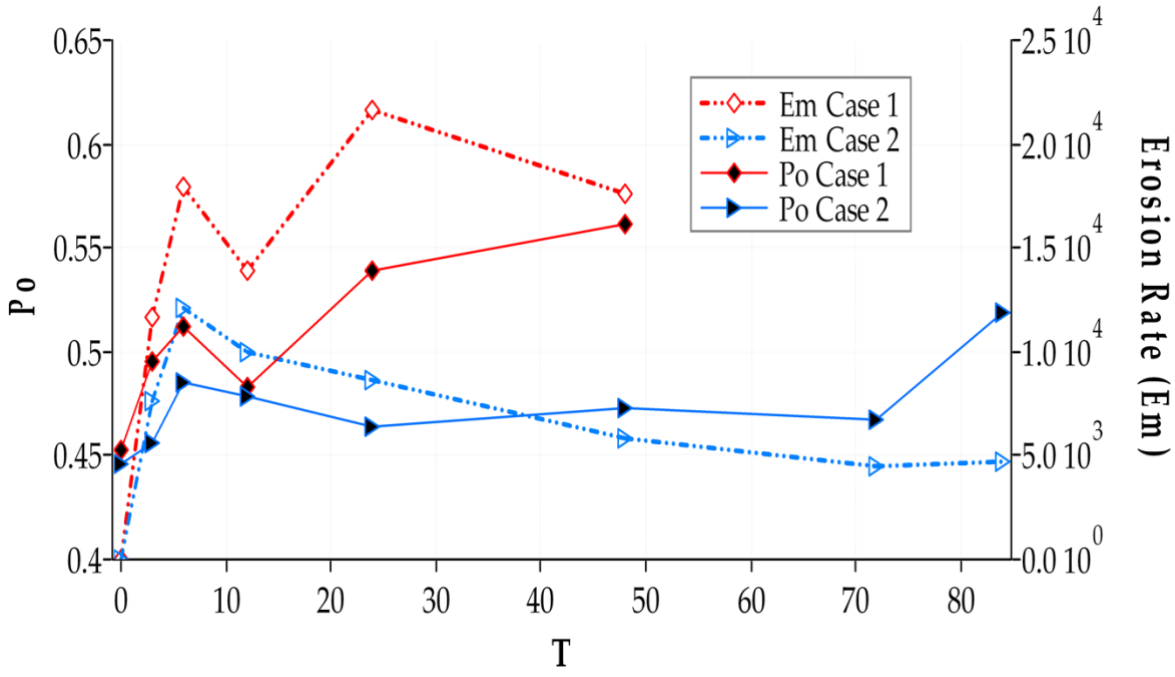

Figure 32: Graphs of the mean erosion rate (Em, dashed lines, mm3/h) and the fraction of exposed bed (Po, solid line) for Case 1 (in red) and Case 2 (in blue). The horizontal axis is the cumulative time T (h); the vertical axes represent Po on the left and Em on the right.

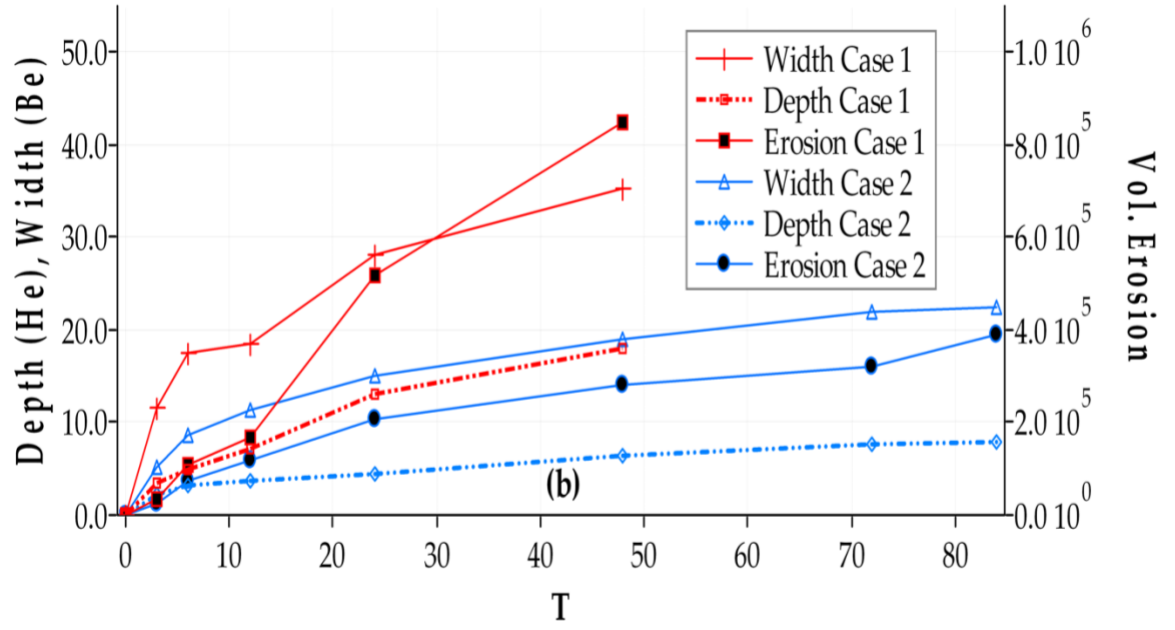

Figure 33: Temporal evolution of the erosion for Case 1 (red) and Case 2 (blue) over cumulative time T (h). The vertical axis on the left represents the depth (He) and the width (Be) of the inner channel (mm), and the right axis represents the volume of erosion (mm3/h).

3.4.4 Bedrock surface and erosion

As previously explained, the water depth and sediment used during both Case 1 and Case 2 were identical, and the only difference was the cover lid rotation speed, which was 40 RPM for Case 1 and 48 RPM for Case 2. This made it possible to investigate the effect of rotation speed on abrasion erosion on the bedrock surface by comparing the two cases.

First, the erosion in Case 2 was less than half that of Case 1. In fact, at the end of timestep 6, the total volume of erosion in Case 1 was 800,000 mm^3, whereas it was only 300,000 mm^3 in Case 2 (Figure 33). In general, the erosion graphs grew quickly from the start until T = 6 h, and gradually increased afterward. However, a sudden rise in the erosion appeared at T = 24 h in Case 1, and at T = 84 h in Case 2.

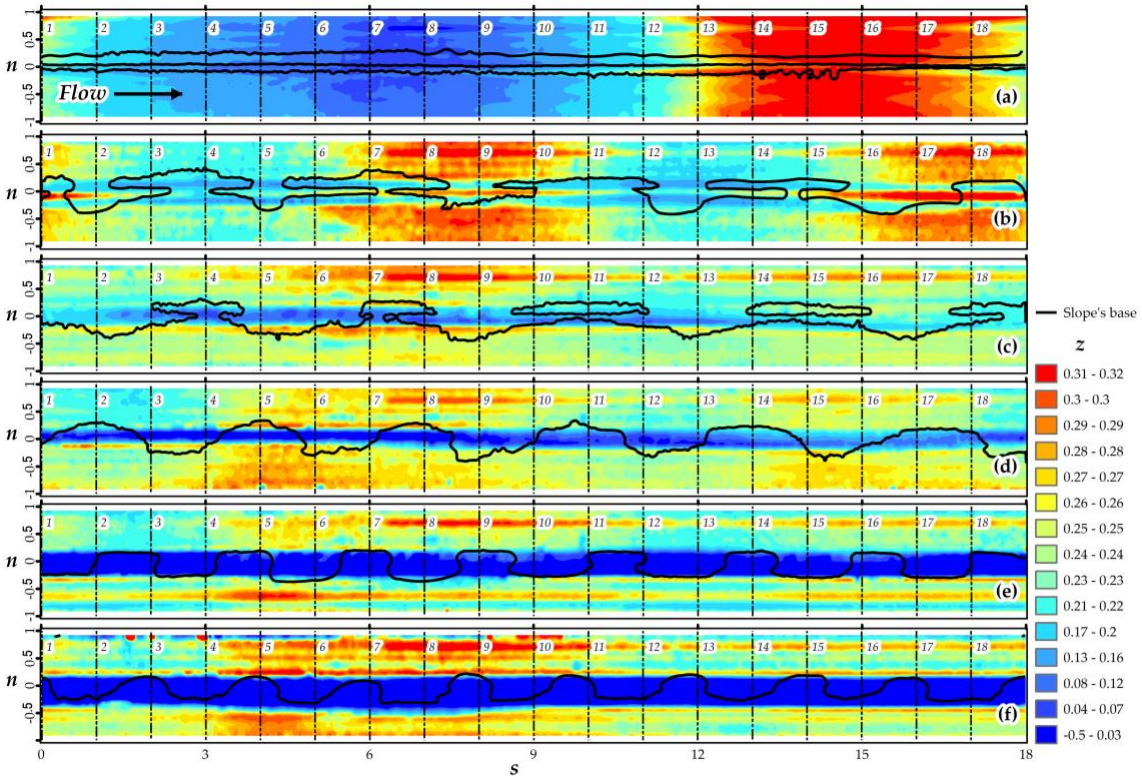

Figure 34: Plan views of the bed configurations - Bedrock surface, Case 1 (40 RPM) for all the timesteps: (a) timestep 1 (T = 5 min), (b) timestep 2 (T = 3 h), (c) timestep 3 (T = 6 h), (d) timestep 4 (T = 12 h), (e) timestep 5 (T = 24 h), and (f) timestep 6 (T = 48 h).

Second, the lateral expansion of the inner channel was faster than the vertical expansion. The increase in width (Be) was more significant than the increase in depth (He) throughout

the experiments in both cases. At the end of the experiments, Be was 35 and 22 mm in Case 1 and 2, respectively, while He was 18 and 8 mm, respectively (Figure 33).

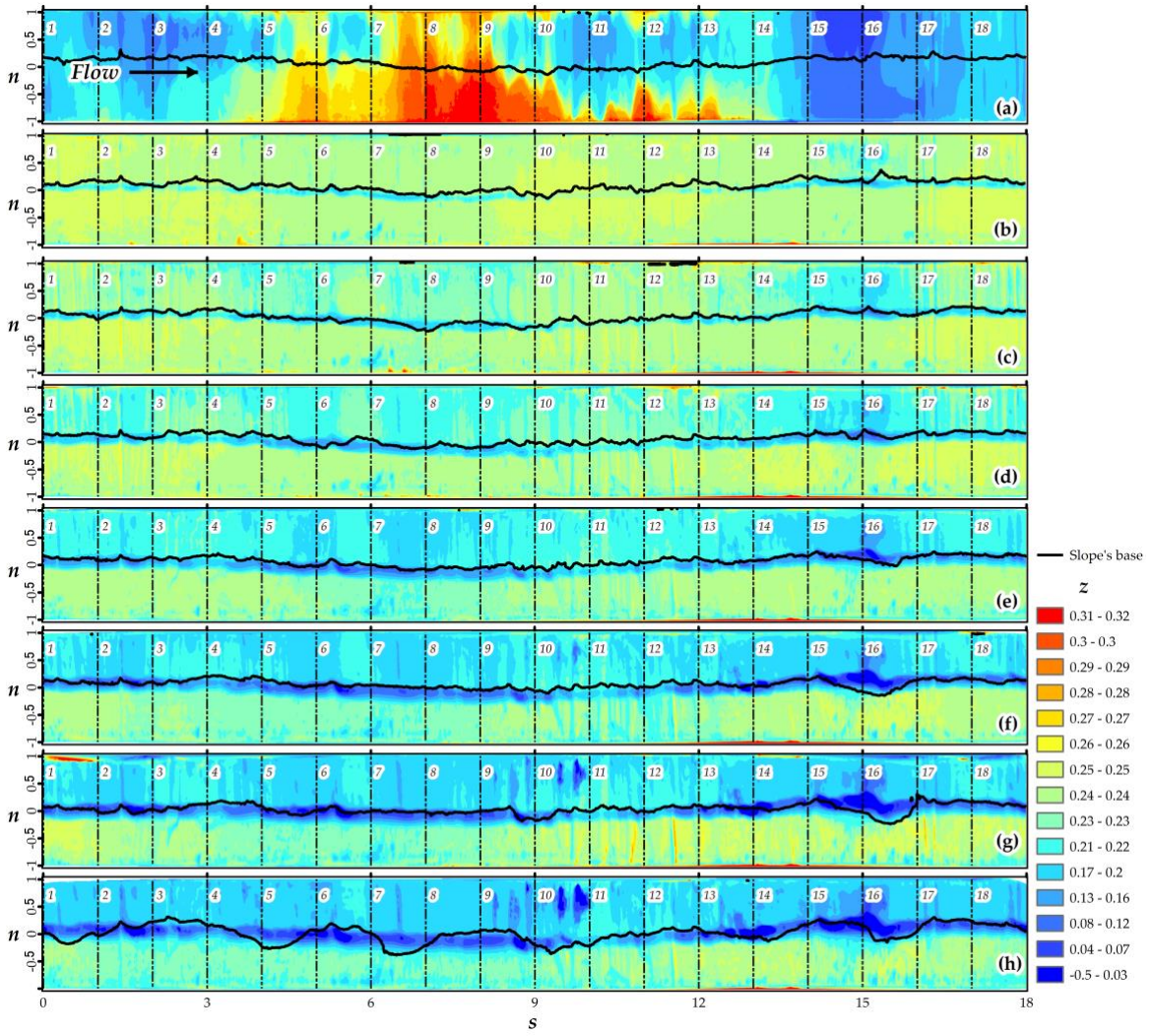

Figure 35: Plan views of the bed configurations - Bedrock surface, Case 2 (48 RPM) for all the timesteps: (a) timestep 1 (T = 5 min), (b) timestep 2 (T = 3 h), (c) timestep 3 (T = 6 h), (d) timestep 4 (T = 12 h), (e) timestep 5 (T = 24 h), (f) timestep 6 (T = 48 h), and (g) timestep 7 (T = 72 h); (h) timestep 8 (T = 84 h) but with 40 RPM.

Figure 34 and Figure 35 show the plan views of the bedrock surface after pouring the water and removing the sediment inside the flume, for Case 1 and Case 2, respectively. The figures represent the relative height of the bedrock surface in the annular flume, also plotted dimensionless. The corresponding profile sections are presented in Figure 36 as NS. The timesteps-displays allow to observe the temporal evolution of the inner channel, which is

the result of the incision of the bedrock surface. Growth in the inner channel, considered primary erosion, was observed along the boundary between the bed coverage and the exposed bed, inside the sweep width (W) area.

Finally, Case 1 obtained a much more advanced inner channel stage than Case 2. The bedrock was vertically incised, then downcut toward the inner wall (Figure 36 a). In Case 1, the incision toward the inner wall was visible from T = 12 h. The vertical incision was observed until T = 12 h in Case 1, while in Case 2 (Figure 36 b), it was observed until T = 84 h.

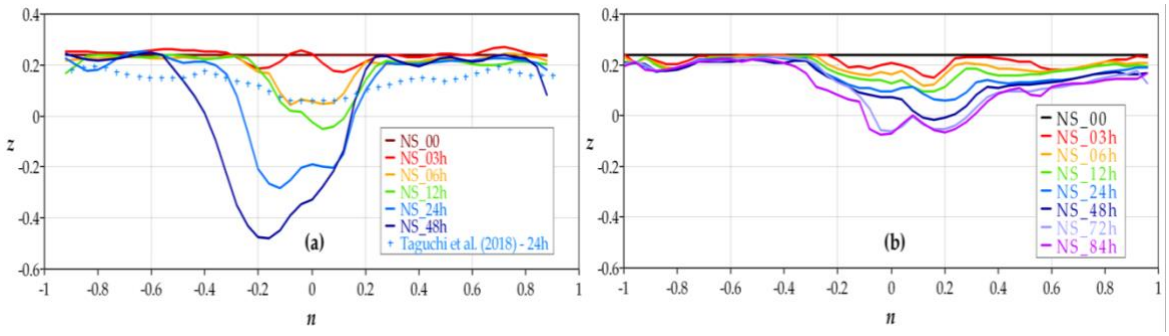

Figure 36: Circumferentially averaged bedrock surface profiles evolution with the cumulative time T, Case 1 (a) and Case 2 (b). The radial and vertical coordinates (n, z) are represented by the horizontal and vertical axes, as shown in Figure 7. The centerline of the flume is represented by n = 0, with negative values on the half side near the inner wall and positive values on the outer wall side. The measured mortar bedrock surface level by Taguchi et al. [28] at T = 24 h are plotted as blue crosses.

4 Comparison with Experiments

4.1 Preprocessing

The applicability of Equation (97) is compared with the experimental data, presented in the previous section. Among the parameters involved in that equation, the bed roughness z_0 and the depth-averaged velocity U_a^* can be considered for validation.

It should be reminded that two experiments, Case 1 and Case 2, were conducted in an annular flume for bedrock erosion investigation in uniformly curved channels. Both cases employed identical sediment (2.5 kg, $D_s^* = 0.45$ mm, $\rho_s = 2.61 \frac{g}{cm^3}$); however, the top ceiling rotation speeds were different, 40 and 48 RPM, respectively. Each experiment is subdivided into timesteps (Table 1), 6 timesteps for Case 1 and reaches a total runtime of 48 hours and 8 timesteps for Case 2 with a total time of 84 hours [63].

The bed surface was surveyed circumferentially after each timestep using laser scanners [32,33,63]. The experiments results showed that the sediment is deposited along the inner wall, showing two bedform types: uniform and wavy, as presented in Figure 16 and Figure 17.

The depth-averaged velocity in the flume U_a^* can be estimated directly from the top ceiling rotation speed using [39]:

$$U_a^* = \Omega \, R_c^*/3 \qquad (101)$$

where Ω is the rotation speed of the top ceiling expressed in rad/s.

On the other hand, two different values of z_0 can also be extracted from the experiments when considering the obtained two bedform types, as observed in Figure 16 and Figure 17. Assuming a rough boundary, $z_0 - GR$ and $z_0 - BFR$ are calculated using Equation (27) and the equivalent roughness [64]. Consequently, herein, $z_0 - GR$ represents the grain roughness, and $z_0 - BFR$ is the bedform roughness.

From the bed surface of both Case 1 and Case 2, the average profile sections presented in Figure 23 and Figure 31 will be used for the validation [22,63].

Table 2 summarizes the calculated parameters to reproduce the analytical bed profiles.

Table 2. Calculated parameters (depth-averaged flow velocity and boundary roughness) obtained from the experiments.

	Case 1			**Case 2**		
U_a^{*} [3]	**0.62**			**0.75**		
Timestep	$z_0 - GR$ [1]	$z_0 - BFR$ [2]	n_0	$z_0 - GR$ [1]	$z_0 - BFR$ [2]	n_0
1	0.0012	0.0038	-0.08	0.0012	0.0047	0.07
2	0.0012	0.0054	-0.05	0.0012	0.0035	0.1
3	0.0012	0.0059	-0.13	0.0012	0.0033	0.07
4	0.0012	0.0072	0.01	0.0012	0.0049	0.18
5	0.0012	0.0088	-0.15	0.0012	0.0047	0.065
6	0.0012	0.00946	-0.2	0.0012	0.0045	0.06
7	0.0012	-	-	0.0012	0.0052	0.06
8	0.0012	-		0.0012	0.0067	0.02

[1] z_0 – GR: the bed roughness calculated based on the Grain Roughness [64], equal to $2D_S^*$; [2] z_0 – BFR: the bed roughness calculated based on the Bed Form Roughness [64], equal to $\delta(\delta/L)^{0.1}$, δ and L are the bedform height and length respectively; [3] U_a^*: the depth-averaged of the flow velocity rotation speed (m/s) [39,63].

4.2 Results

The comparison results are plotted from Figure 37 to Figure 40. As in Figure 23 and Figure 31, the vertical axis z represents the relative height, and the horizontal axis n represents the channel width from the inner wall $(n = -1)$ to the outer wall $(n = 1)$, both non-dimensional.

The calculated cross sections are obtained using Equation (97) and the parameters in Table 2. The corresponding graphs for Case 1 and Case 2 are colored in red ad in blue, respectively. The value of n_0 may vary for each timestep and each Case (cf. Table 2). The experimental data, however, are scatter-plotted as dots for Case 1 and diagonal crosses for Case 2. Figure 37 shows the comparisons for timesteps 1 and 2, Figure 38 for the timesteps 3 and 4, Figure 39 for the timesteps 5 and 6, and finally Figure 40 for timesteps 7 and 8.

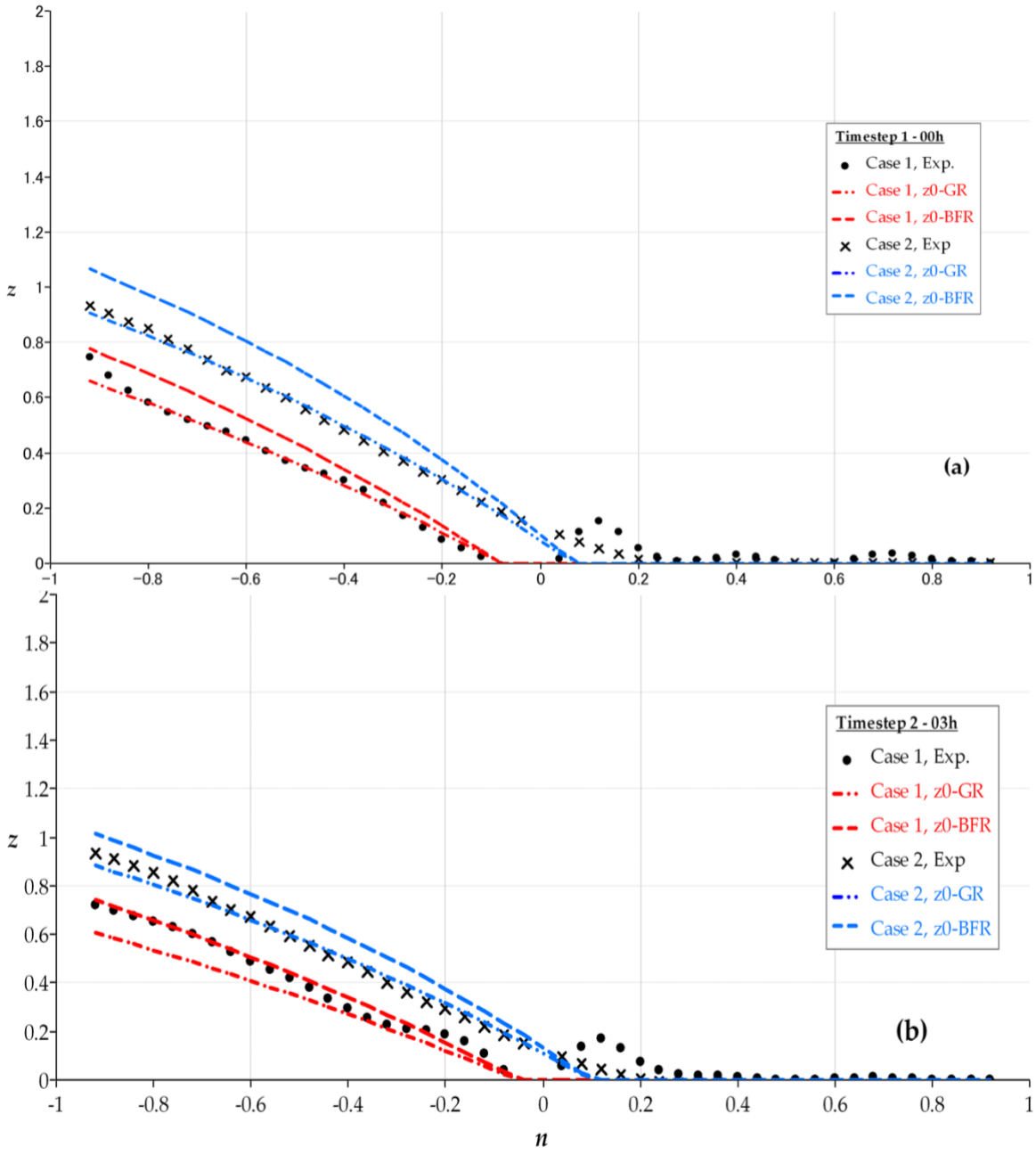

Figure 37: Calculated and measured bed profile cross-sections for Timestep 1 – 00h (a) and Timestep 2 – 03h (b).

At the beginning of the experiment (Figure 37a), both Case 1 and 2 data agreed well with the theoretical models based on the Grain Roughness (z0-GR). In Figure 37b, 3 hours later, the Case 2 data still agreed with the z0-GR model, whereas the Case 1 data shifted to the model made on the Bedform Roughness (z0-BFR).

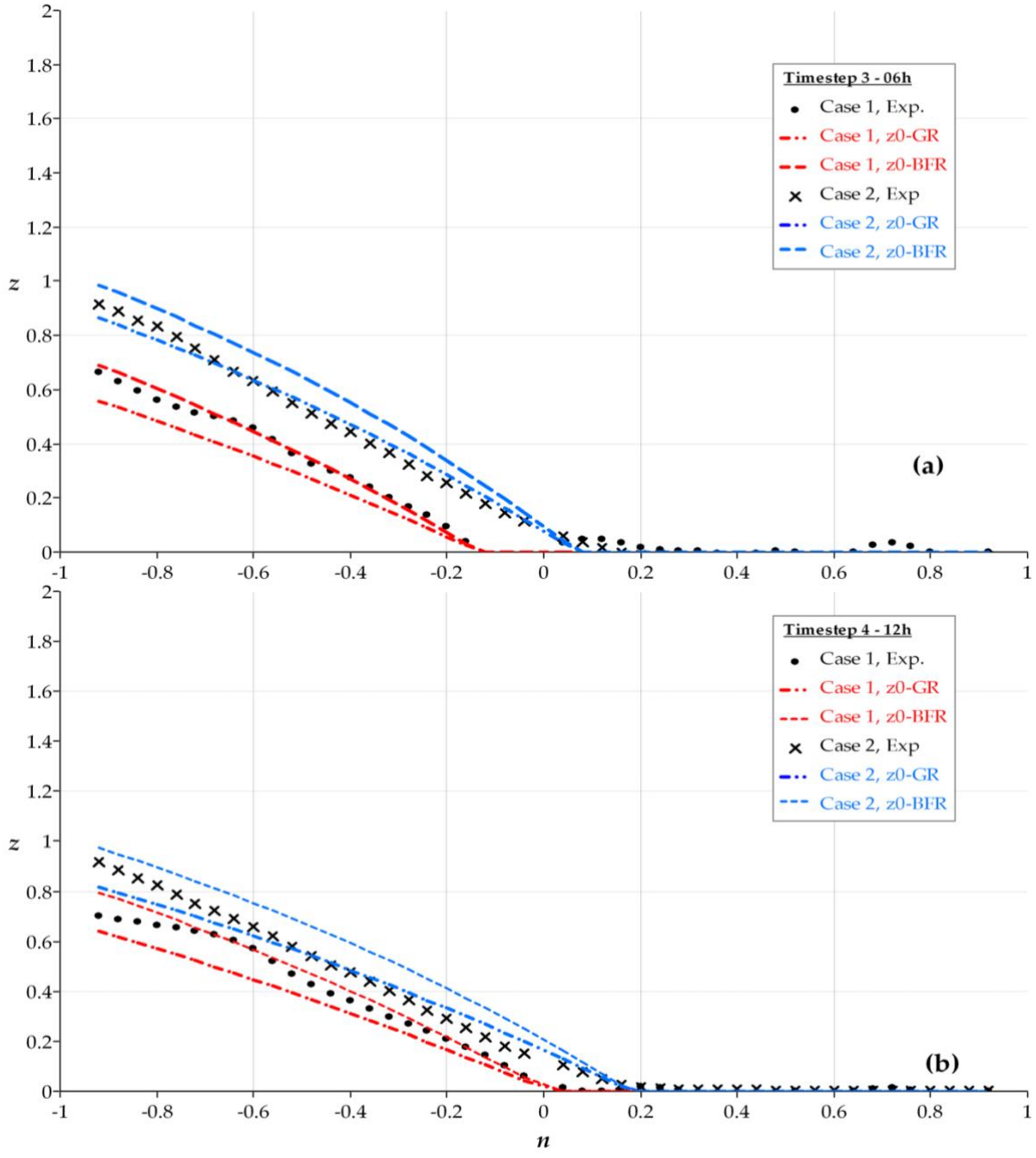

Figure 38: Calculated and measured bed profile cross-sections for Timestep 3 – 06h (a) and Timestep 4 – 12h (b).

Again, the Case 1 data still fitted more with z0-BFR models for the timesteps 3 and 4. In contrast, the Data for Case 2 is closer to z0-GR models (Figure 38a & b). The same scenario was also observed after timesteps 5 and 6 for Case 1 and 2, respectively (Figure 39a & b).

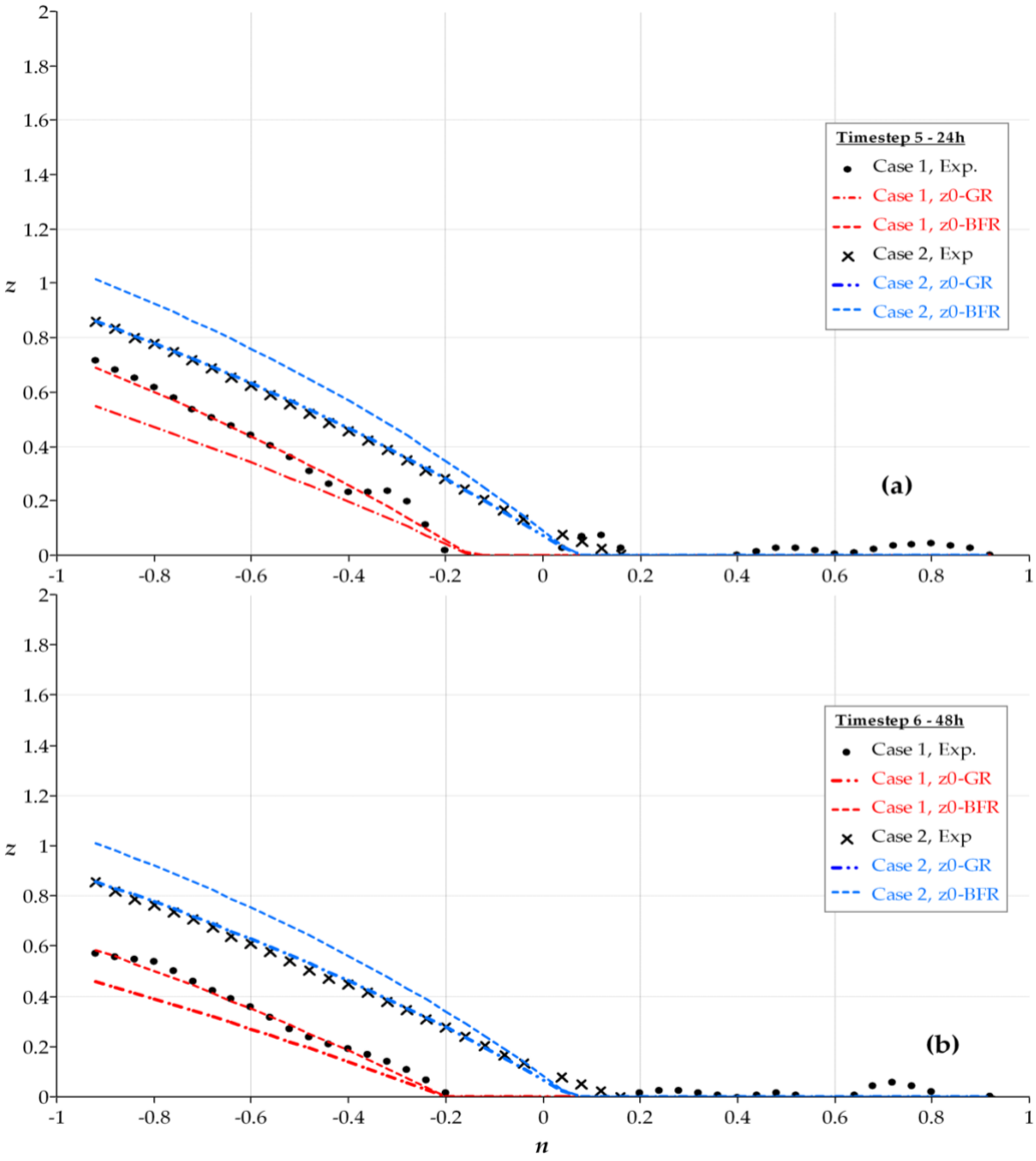

Figure 39: Calculated and measured bed profile cross-sections for Timestep 5 – 24h (a) and Timestep 6 – 48h (b).

Timesteps 7 and 8 are exclusively dedicated to Case 2, as Case 1 ended at timestep 6 (Table 1). The experimental data showed good agreement with the z0-GR model for timestep 7 (Figure 40a); in contrast, the experimental data shifted to the z0-BFR model at timestep 8, when the rotation speed was reduced to 40 RPM (Figure 40b, Table 1).

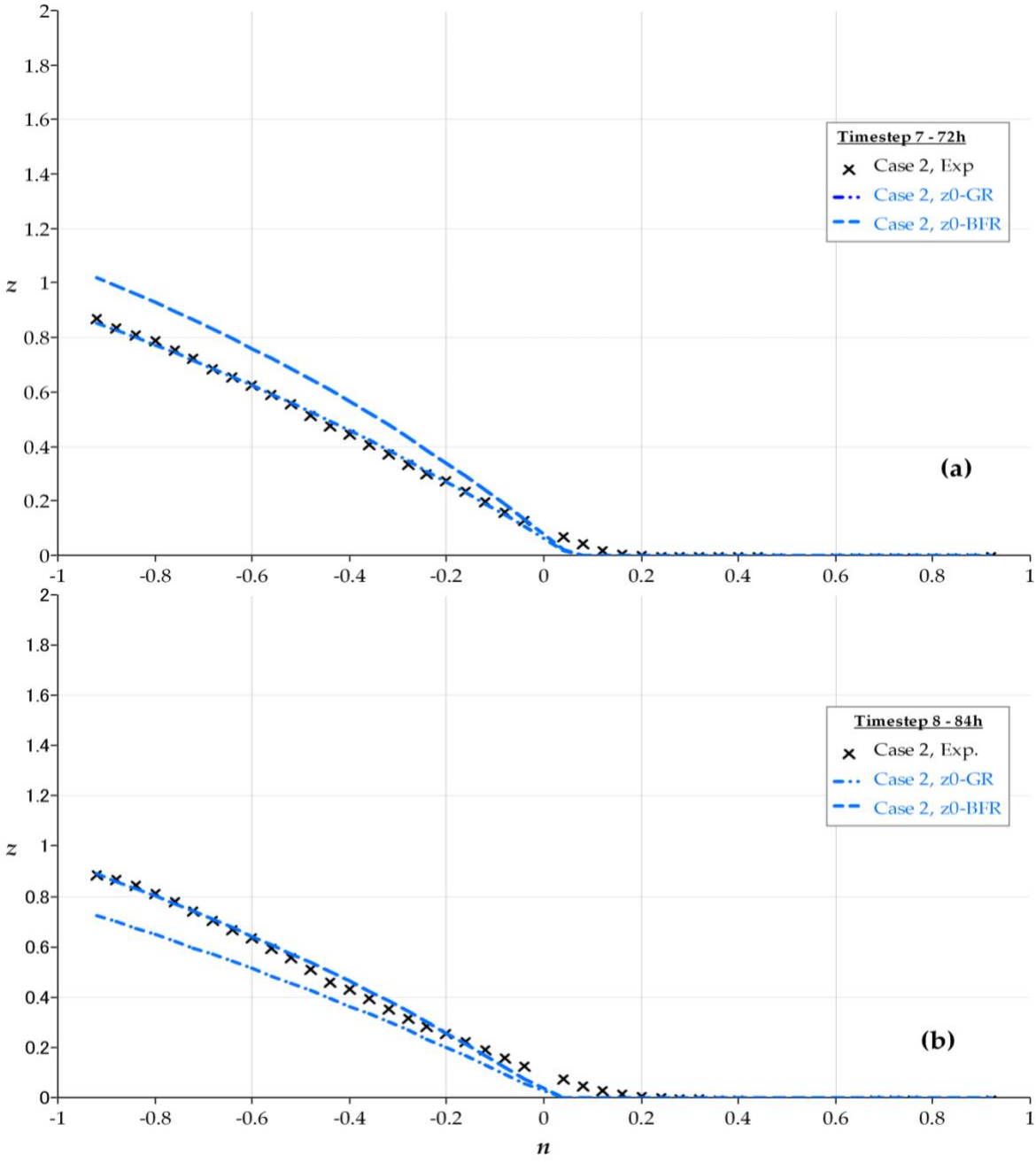

Figure 40: Calculated and measured bed profile cross-sections for Timestep 7 – 72h (a) and Timestep 8 – 84h (b).

5 Discussion

5.1 Discussion on the velocity distribution and bed morphology

Figure 3 exhibited the distribution of the primary velocity at the centerline of the flume in a non-dimensional form. The flow distribution appears to be symmetrical at the center of the flume. This symmetry feature is attributed to the fact that the boundary roughness at the top and the bottom are assumed to be similar during the analysis for simplicity. However, this assumption stands because, in the experiments, the roughness difference between the top lid cover (Plexiglas) and the bottom (fine grain gypsum) is negligible compared to the sediment characteristics. Thus, it is supposed not to affect the primary flow velocity distribution significantly.

Similarly, the secondary flow velocity distribution in Figure 4 shows a symmetrical likewise shape. It indicates that the flow goes toward the outer wall near the top (positive value) and the inner wall near the bottom. However, the velocity magnitudes differ so that the near-top velocity is slightly higher than the bottom one, which makes sense because the flow motion of the top lid cover generates the flow inside the flume. Near the bottom, the secondary flow velocity varies between $25-30\%$ of U_a^* for z_0 ranging between $0.0001-0.01$. This is in good agreement with the suggested results by previous studies [23].

However, in contrast to the primary flow, the secondary flow velocity distribution does not match at the center of the flume; it matches around $z=0.1$. This is because the shear stress due to the secondary flow should match at the center of the flume (Equation (59)), not the secondary flow velocity. As a result, the center of the spiral flow is located slightly above the center of the flume.

In addition, further analysis was made to examine the effect of the parameters listed above on the transverse bed slope, expressed in Equation (97). The results are reported in Figure 6 to Figure 10.

With the increasing distance n_0 from the inner wall, the transverse bed slope appears to decrease slightly (Figure 6). The geometrical analysis on the wavy bedforms reported in previous studies reveals similarities with this variation of the transverse bed slope with n_0 [22,29,33,50,63]. This bed slope and n_0 relationship could be attributed to various factors, such as the decrease of the bed shear distribution, the amount and characteristics of the sediment–dynamic friction angle, and the secondary flow along the transverse bed slope [22,29,50]. Further investigation would be needed to confirm this connection between the transverse bed slope and n_0.

Figure 7 shows that the transverse slope angle increases when the depth-averaged flow velocity grows. This transverse bed slope behavior looks apparent because the increase of U_a^* makes θ more significant (Figure 10, Equation (93)), which diminishes M (Equation (96)) and thus increases η (Equation (97)).

Interestingly, previous experimental results show alike variation of the transverse slope with the depth-averaged flow velocity, however not that significant [22,29,63]. The reasons for this slight discordance might be the result of the interference of other parameters during the experiments, which are kept constant here. Moreover, an increase in the bed roughness also causes the bed slope to rise, as seen in Figure 7. Previous studies suggested that the bedforms strongly affect the secondary flow, which, in turn, impacts the transverse bed slope [50,53,65]. When z_0 increases, the secondary flow increases (Figure 4), whereas the primary flow decreases (Figure 3), thus increasing the parameter M (Equation (96)). In addition, the height where the maximum velocity occurs also increases (Figure 4). Combined, those two conditions would ease the growth of the transverse bed slope, as also observed in Figure 8 and Figure 9. Figure 8 highlights the effect of the channel aspect ratio β on the transverse bed slope. The transverse slope appears to rise with the channel aspect ratio. The bed slope is sharp when the channel is broader than the water depth.

Finally, the transverse bed slope variation with flow velocities ratio is presented in Figure 9. It shows that the increase of the near-bed flow velocities ratio ϑ_1^l/u_0 enlarges the

transverse bed slope. In contrast to the channel width, a thick water column has less impact on the transverse bed slope.

5.2 Discussion on the erosion

The results reveal the mechanism involved at the onset of the erosion. Also, the spatiotemporal evolution of the inner channel and the sediment deposition pattern found during the experiments allow us to determine how erosion evolves in space and time.

5.2.1 The erosion locus

The inner channel formed along the boundary between the bed coverage with sediment and the exposed bedrock. This boundary is located around the channel centerline. Furthermore, if looking into the transverse slope, this boundary was at the base of the transverse slope, where the sediment coverage is relatively thin. A close observation of the incision of the bedrock surface at the end of timestep 2 reveals that the bedrock was downcut vertically (Figure 23).

While it was impossible to accurately determine the thickness of sediment coverage under which the bed incision occurs, we could graphically estimate that it required about 0.2 in the experimental conditions employed in this study, or approximately 20 times the sediment grain size. It should be noted, however, that this estimation was deduced from the transverse slope at the end of each timestep, meaning that it was at its angle of repose. This suggests that the thickness of the deposit was less than 0.2 in our study.

Under that thickness, the sediment grains can saltate, hit, and wear the bedrock surface. When the coverage exceeds that boundary, no erosion occurs because the motion of the sediment grains cannot reach the bed surface and can be considered a fully covered bed. According to previous researchers, that boundary is the place of "tradeoff between the availability of abrasive tools and the partial alluviation of the bedrock" [9] or the toe of the alluvial bedforms [12] or the portion moderately covered with sediment [27,28]. In sum, the

base of the transverse slope would be the only place where the sediment grains may collide with the bedrock surface [30].

On the other hand, increased cover lid rotation speed did not affect the location of erosion occurrence. That is, the boundary between the sediment coverage and the exposed bed was positioned at the same place across the flume width on both Case 1 and Case 2. This can likely be attributed to the mean transverse slope and the amount of sediment used, since they specify the position of the boundary between the sediment coverage and the exposed bed, as well as the location of the incision. This is consistent with Engelund's findings [21] that the mean transverse slope was almost independent of the top lid rotational speed as long as the sediment grains flowed as bedload. Taguchi et al. [28] also obtained similar results to the current study with the same amount and caliber of sediment. From these results it can be concluded that the border between the sediment-covered bed and the exposed bedrock where erosion occurs is essentially the same regardless of how fast the cover lid rotates.

We also observed linear scours on the exposed bed surface even though erosion should not have happened on the exposed bed based on the abrasion models. These scours, we believe, were the consequence of interaction between sediment grains and flow directly on the bedrock surface, with the fine structure of the gypsum powder in the plaster allowing this interaction engraved on the bed surface (Figure 15, right). If this is the case, these linear scours should be investigated further to understand flow dynamics at the bedrock-fluid interface better.

5.2.2 The evolution of the bedrock incision and the inner channel

5.2.2.1 *The bedrock incision evolution*

The rate and spatial extension of the bedrock incision was found to be inversely proportional to the cover lid rotation speed. That is, a faster rotation speed is associated with less erosion. This is due to the sediment deposition patterns imposed by the flow conditions. With a higher rotation speed (48 RPM in Case 2), uniform transverse slope formed, and the

incision occurred only along its base. With a slower rotation speed (40 RPM in Case 1), migrating bedforms formed, leading to an increase in the bed area subjected to erosion, which can be attributed to the undulations of the bedform boundary (Figure 16, Figure 17, Figure 23, and Figure 31). Also, when reducing the rotation speed from 48 to 40 RPM (Case 2, timestep 8), the bedforms reappeared (Figure 17 h), resulting in a greater erosion rate at the end of the experiment in Case 2 (Figure 32).

The bedforms vary with rotation speed because the speed influences the secondary flow (e.g., [16,24]), and with time as the bedforms fluctuate and stabilize at a "mature" stage (e.g., [21,26,24]).

In addition, when the undulating bedforms are formed, their migration allows for the alternation of "covered" and "exposed" bedrock surfaces, a phenomenon known as runaway alluviation [37]. This runaway alluviation combined with the saltation of the sediment grains and the undulation of the boundary explains the higher erosion in Case 1 than in Case 2. In the latter, no runaway alluviation was observed. Our results provided one quantitative example of runaway alluviation to add to the results obtained in previous studies (e.g., [8,20,21,31]).

5.2.2.2 The inner channel development

Initially, the incision vertically downcut the bedrock, slightly shifting toward the outer wall (Figure 36). This vertical incision occurred at the center of the sweep width (W), or right under the boundary of sediment coverage and the exposed bed, because this location had a high probability and high frequency of erosion. This high probability of erosion was due to the primary conditions of incision and high frequency due to its position inside the sweep width.

The advanced state of the incision shows that it gradually downcut towards the inner wall (Figure 36 a). This shift resulted from the alternating lateral shift toward the inner wall and the downward incision on the bedrock surface. Because no extra sediment was supplied, the bedrock near the outside wall was left exposed. Because the sediment was only available

along the inner wall side due to the spiral flow, it is evident that the conditions for maximum incision also move towards the inner wall. The height of the bedform gradually decreased with the growth of the inner wall, suggesting that the incision would erode the bedrock along the inner channel at some point.

This incision toward the inner wall is consistent with the results reported by Fernández et al. [12] using a meandering channel of highly fixed sinuosity in the absence of sediment supply. Shepherd [31] also discovered similar findings in his experiment along the manually excavated sinuous channel and reported that the erosion went toward the inside of the bend until the gradient and the velocity dropped, allowing the sediment to deposit, and after that the erosion process inverted toward the outer wall.

However, this was not reported by Taguchi et al. [27,28] in their experiment. The geometry of the inner channel may explain this. In this study, the simulated bedrock, made of plaster, provided faster erosion. For instance, at T = 24 h, the inner channel size was larger in plaster than in mortar (Figure 36a). The flow dynamics combined with this growth of the inner channel and the sediment transport inside the flume likely explain the actual result.

In the current study, there was no sediment supply, and the rotation speed was maintained constant so the erosion would continue toward the inner wall. However, further investigation is required to determine the progress of the inner channel.

5.2.3 The deposition patterns

Along uniformly curved channels, the bedforms depend on the rotation speed, time, and development of the inner channel resulting from the bedrock incision.

First, the averaged transverse slope angle for both cases was similar, at about 23 degrees, throughout the timesteps (Figure 23 and Figure 31). This averaged angle represents the angle of the mean bedforms and was found to be independent of the rotation speed in case of sediment bedload transport [24]. However, the difference in the slope angles in Case 1 and Case 2 may be related to the timing of the measurements and the rotation speed. The

slightly higher transverse slope angle and height in Case 2 than in Case 1 can likely be attributed to the faster rotation speed of Case 2 [24]. However, we should remember that the obtained values may be underestimated because these measurements were made after the experiments were stopped.

Second, while the secondary flow increases when the rotation speed is high, the spiral flow wavelength, as well as the wavelength of the bedforms decreases. Case 2, at 48 RPM, for example, had poorly formed bedforms that were hardly discernible (Figure 17). Engelund [21] discovered a similar result when the rotation speed was increased and attributed it to the reformation of the uniform transverse slope. Inversely, with a slower rotation speed, the secondary flow decreases, and the effects of the spiral flow on the bedforms could be well observed, as we could witness the well-formed bedforms in Case 1 at 40 RPM. After timestep 2, for example, there were 5 and 12 bedforms in Case 1 and Case 2, respectively. This is consistent with the results reported by Baar et al. [24] and Kikkawa et al. [23] when observing the effect of the variation of the secondary flow intensity on the bed morphology.

Third, the number of bedforms increases with the growth of the inner channel. When the rotation was lowered from 48 to 40 RPM, as in Case 2 timestep 8, the bedforms reappeared, with a total of 6 bedforms (Figure 35 h). However, for the same 12 h of experimentation in timestep 4 in Case 1, there were 8 bedforms (Table 1). This discrepancy could be attributed to the difference in the dimension of the inner channel, which is more significant in Case 1 than in Case 2 (Figure 36). A larger inner channel was associated with increased bedforms from 5 to 9, as seen in Case 1 (Figure 34).

Finally, another feature revealed by the experimental results is the reformation of the uniform transverse slope over a longer experiment run, as indicated in Case 2 (Figure 17). The bedforms gradually faded as the rotation speed increased, restoring the uniform transverse slope. The gradual convergence of the sediment surface towards the uniform transverse slope can be seen in the section profiles (Figure 23 and Figure 31). However, these

results do not agree with the results reported by Engelund [21] and Taguchi et al. [27]. They claimed that the number of bedforms increased and then decreased as the experiment progressed. In Engelund's experiment, the erosion was not part of the study, whereas in Taguchi et al.'s experiment, the erosion was not significant compared to the erosion observed. Most likely, the development of the inner channel was the reason for this discrepancy (Case 1). While it remains unclear, it appears that the inner channel's growth adds to the flow dynamics' complexity. On the other hand, this discrepancy can also be the outcome of the bedforms splitting and merging processes in Case 2, leading to an equilibrium state at a mature experiment stage. This is a topic for further investigation.

5.3 Discussion on the analytical and experimental data comparison

One of the objectives of this study is to compare the analytical transverse bed slope with the transverse bed slope obtained during the experiments, which results from the interaction between the flow and the sediment transport in the annular flume.

One of the physical terms of this interaction that has been considered here is the bottom roughness z_0, affecting the flow near the bed, and thus influencing the transverse bed slope. Interestingly, analytical data showed good agreements with the experimental data. This agreement provides further evidence for the importance of considering the bottom roughness even in curved channels. In contrast to earlier findings [22,35], the actual transverse bed slope model permits to include this bottom roughness and qualitatively provides better accuracy of the estimation of the transverse bed slope.

When there are the wavy bedforms, the transverse slope section of the depositional morphology can be predicted with Equation (97), but using the equivalent roughness "Bedform Roughness", as seen at the timesteps 2 – 6 for Case 1 (Figure 37 b, Figure 38, and Figure 39)and at the timesteps 8 for the Case 2 (Figure 40 b). Conversely, the use of the equivalent roughness "Grain Roughness" provides more accurate prediction of the transverse slope section in case of uniform transverse slope, as observed at the timestep 1

for both cases (Figure 36), and at timesteps 2 to 7 for Case 2 (Figure 37, Figure 38, Figure 39, and Figure 40 a).

With the calculated and the chosen parameters, each figure revealed suitable agreements of the theoretical and the experimental data. Particularly, the experimental data for Case 1 fit more with the theoretical model which uses $z_0 - \mathrm{BFR}$. Case 2, on the contrary, the experimental data are closer to the theoretical model, which are obtained with $z_0 - \mathrm{GR}$.

Our data comparison was only limited to the parameter Transverse bed slope, due to the lack of available data. In addition, the relationship between the transverse bed slope and the erosion by incision, as function of n_0 and the wavy bedforms characteristics (e.g., wave celerity) has not been modeled. First, a better understanding on the sediment thickness under which the abrasion may occur, and second, an accurate estimation of the variation of n_0 as function of the near bed flow fluctuation would be able to calculate the erosion.

6 Conclusion

This work has shown the close interaction between the flow and the sediment transport/deposition in uniformly curved channels. This interaction significantly affects the bedrock incision along such channels.

The flow velocities distribution in annular flume revealed a spiral flow pattern. The spiral flow center is located slightly above the center of the channel and the near flow velocity. The near-bottom velocity varies between $25-30\%$ of the depth-averaged velocity in the flume. The bed roughness level significantly affects the flow velocity distribution, and inversely, the flow pattern also conditions the bed morphology, based on which the bed roughness calculation is based.

The analytical findings indicated that, under the bedload transport mode of the sediment, the bed morphology accentuates the bottom boundary roughness, influencing the near-bed primary and secondary flow velocities. Conversely, the flow at the bottom of the channels also conditions sediment transport and deposition. At the first order of the channel curvature, the bed morphology, expressed as the transverse bed slope, depends on different parameters such as the ratio of the secondary to the primary flow near the bed, the aspect ratio of the channel, the boundary roughness, the shield stress, and the location of the transverse slope base.

The experiments in annular flume allowed to simulate erosion by incision of the bedrock along uniformly curved channels. The bedrock incision was observed at the base of the transverse slope. The rotation speeds significantly impacted sediment deposition and transport. The evolution of erosion and the in-flume flow were closely related and varied with time and space. The rotation speed does not significantly impact the average transverse slope angle, but it does condition the formation of wavy bedforms. The initial uniform transverse slope gradually turns into bedforms. After a long experiment run, the bedforms may turn back into uniform transverse slopes, thanks to the bedforms splitting and merging.

The bedrock incision occurs mainly at the base of the transverse slope and the growth of the inner channel – the result of the incision depends on whether the bed deposition pattern constitutes a uniform transverse slope or bedforms. The base of the transverse slope - the boundary of the exposed bed and the sediment coverage appears linear under the uniform transverse slope and undulates inside the sweep width when the bedforms form. The erosion is minimal when the transverse slope is uniform along the flume, leading to a vertical, shallow, and narrow channel. In contrast, erosion is significant when there are bedforms: the spatiotemporal variation of the bedforms conditions the development of the inner channel. When there is no sediment supply, the inner channel progresses towards its convex side, leaving the concave side and the bedrock surface near the outer wall of the flume intact.

The study's results constitute an initial step toward understanding the bedrock incision in curved channels. Further analysis would be necessary to investigate the bond between the transverse slope and the bedrock incision, by introducing the obtained transverse slope model to the existing erosion models along the transverse direction, also by inserting a function varying with time, which permits to control the start of the deposition n_0.

In addition, more experiments are also necessary; not only would it bring more data for validation, but also would increase the data's accuracy. A large value of each variable (water depth, bedrock type, sediment type and amount, slope…) is to be monitored, including the rotation speed of the top cover lid.

Last but not the least, a deeper investigation of the effect of the development of the inner channel and the suspended sediment on the flow dynamics is required. The bigger the inner channel becomes, the greater its influence on the flow velocity distribution and sediment transport and deposition Simultaneously; the effect of suspended sediment from the eroded bedrock on the flow dynamics should also be examined; it may affect the sediment transport and deposition, increase the boundary roughness, it may reduce the average flow, even the erosion rate.

Bibliography

1. Kirkby, M. Alluvial and Non-Alluvial Meanders. *The Royal Geographical Society* **1972**, *4*, 284–288.
2. Mishra, J.; Inoue, T.; Shimizu, Y. Comparison of Bedrock and Alluvial Meanders Using 2D Modelling. *Journal of Japan Society of Civil Engineers, Ser. B1 (Hydraulic Engineering)* **2017**, *73*, I_835-I_840, doi:10.2208/jscejhe.73.i_835.
3. Nakano, D.; Nakamura, F. The Significance of Meandering Channel Morphology on the Diversity and Abundance of Macroinvertebrates in a Lowland River in Japan. *Aquat Conserv* **2008**, *18*, 780–798, doi:10.1002/aqc.885.
4. Parker, G. River Meanders in a Tray. *Nature* **1998**, *395*, 111–112, doi:10.1038/25832.
5. Wohl, E.; Bledsoe, B.P.; Jacobson, R.B.; Poff, N.L.; Rathburn, S.L.; Walters, D.M.; Wilcox, A.C. The Natural Sediment Regime in Rivers: Broadening the Foundation for Ecosystem Management. *Bioscience* **2015**, *65*, 358–371, doi:10.1093/biosci/biv002.
6. Gallen, S.F.; Pazzaglia, F.J.; Wegmann, K.W.; Pederson, J.L.; Gardner, T.W. The Dynamic Reference Frame of Rivers and Apparent Transience in Incision Rates. *Geology* **2015**, *43*, 623–626, doi:10.1130/G36692.1.
7. Davis, W.M. (Harvard C. The Topographic Maps of the United States. *Science (1979)* **1893**, *21*, 225–226, doi:10.1515/9781400878031-006.
8. Winslow, A. The Osage River and Its Meanders. *Science (1979)* **1893**, *22*, 31–32.
9. Amissah, G.J.; Kiss, T.; Fiala, K. Active Point Bar Development and River Bank Erosion in the Incising Channel of the Lower Tisza River, Hungary. *Landscape & Environment* **2019**, *13*, 13–28, doi:10.21120/le/13/1/2.

10. Blanckaert, K.; Duarte, A.; Chen, Q.; Schleiss, A.J. Flow Processes near Smooth and Rough (Concave) Outer Banks in Curved Open Channels. *J Geophys Res Earth Surf* **2012**, *117*, doi:10.1029/2012JF002414.

11. Kiss, T.; Fiala, K.; Sipos, G. Alterations of Channel Parameters in Response to River Regulation Works since 1840 on the Lower Tisza River (Hungary). *Geomorphology* **2008**, *98*, 96–110, doi:10.1016/j.geomorph.2007.02.027.

12. Whipple, K.X.; DiBiase, R.A.; Crosby, B.T. *Bedrock Rivers*; Elsevier Ltd., 2013; Vol. 9; ISBN 9780080885223.

13. Sklar, L.S.; Dietrich, W.E. A Mechanistic Model for River Incision into Bedrock by Saltating Bed Load. *Water Resour Res* **2004**, *40*, doi:10.1029/2003WR002496.

14. Zhang, L.; Parker, G.; Stark, C.P.; Inoue, T.; Viparelli, E.; Fu, X.; Izumi, N. Macro-Roughness Model of Bedrock-Alluvial River Morphodynamics. *Earth Surface Dynamics* **2015**, *3*, 113–138, doi:10.5194/esurf-3-113-2015.

15. Wardhana, K.; Hadipriono, F.C. Analysis of Recent Bridge Failures in the United States., doi:10.1061/ASCE0887-3828200317:3144.

16. Maddison, B. Scour Failure of Bridges. *Proceedings of the Institution of Civil Engineers: Forensic Engineering* **2012**, *165*, 39–52, doi:10.1680/feng.2012.165.1.39.

17. Smith, L.M.; Winkley, B.R. *The Response of the Lower Mississippi River to River Engineering*; 1996; Vol. 45;.

18. Surian, N.; Rinaldi, M. Morphological Response to River Engineering and Management in Alluvial Channels in Italy. *Geomorphology* **2003**, *50*, 307–326, doi:10.1016/S0169-555X(02)00219-2.

19. Huang, M.W.; Liao, J.J.; Pan, Y.W.; Cheng, M.H. Rapid Channelization and Incision into Soft Bedrock Induced by Human Activity - Implications from the Bachang River in Taiwan. *Eng Geol* **2014**, *177*, 10–24, doi:10.1016/j.enggeo.2014.05.002.

20. Simon, A.; Rinaldi, M. Disturbance, Stream Incision, and Channel Evolution: The Roles of Excess Transport Capacity and Boundary Materials in Controlling Channel Response. *Geomorphology* **2006**, *79*, 361–383, doi:10.1016/j.geomorph.2006.06.037.

21. Thomson, J.; Thomson, W. On the Origin of Windings of Rivers in Alluvial Plains, with Remarks on the Flow of Water Round Bends in Pipes. *Proceedings of the Royal Society of London* **1877**, *25*, 5–8, doi:10.1098/rspl.1876.0004.

22. Engelund, F. Instability of Flow in a Curved Alluvial Channel. *J Fluid Mech* **1975**, *72*, 145–160, doi:10.1017/S002211207500300X.

23. Sheng, Y.P. Consideration of Flow in Rotating Annuli for Sediment Erosion and Deposition Studies. *J Coast Res* **1989**, *SI5*, 207–216.

24. Yen, B.-C. Characteristics of Subcritical Flow in a Meandering Channel, Univ. of Iowa, Institute of Hydraulics Research: Iowa City, 1965.

25. Rozovskii, I.L. (Institute of H. and H.E./ A. of S. of the U.S. *Flow of Water in Bends of Open Channels*; Israel Program for scientiific translations (1961), Ed.; Second Imp.; Academy of Sciences of the Ukrainian SSR: Kiev, 1957;

26. Corney, R.K.T.; Peakall, J.; Parsons, D.R.; Elliott, L.; Amos, K.J.; Best, J.L.; Keevil, G.M.; Ingham, D.B. The Orientation of Helical Flow in Curved Channels. *Sedimentology* **2006**, *53*, 249–257, doi:10.1111/j.1365-3091.2006.00771.x.

27. Fernández, R.; Parker, G.; Stark, C.P. Experiments on Patterns of Alluvial Cover and Bedrock Erosion in a Meandering Channel. *Earth Surface Dynamics* **2019**, *7*, 949–968.

28. Ippen, A.T.; Drinker, P.A. Boundary Shear Stresses in Curved Trapezoidal Channels. *Journal of the Hydraulics Division* **1962**, *88*, 143–180, doi:10.1061/JYCEAJ.0000772.

29. Kikkawa, H.; Ikeda, S.; Kitagawa, A. Flow and Bed Topography in Curved Open Channels. *Journal of the Hydraulics Division* **1976**, *102*, 1327–1342, doi:10.1061/JYCEAJ.0004615.

30. Yen, C.; Ho, S. Bed Evolution in Channel Bends. *Journal of Hydraulic Engineering* **1990**, *116*, 544–562.

31. Odgaard, A.J. Flow and Bed Topography in Alluvial Channel Bend. *Journal of Hydraulic Engineering* **1984**, *110*, 521–536.

32. Taguchi, S.; Ozawa, H.; de Lima, A.C.; Izumi, N. Experimental Study on Bedrock Incision and Bed Configuration in Annular Flume Flow. *Journal of JSCE: Hydraulic Engineering* **2017**, *73*, I_847-I_852, doi:10.2208/jscejhe.73.I_847.

33. Taguchi, S.; Kobayashi, S.; de Lima, A.C.; Izumi, N. Experimental Study on Mixed Bedrock-Alluvial Bed Erosion in Annular Flume Flow. *Journal of JSCE: Hydraulic Engineering* **2018**, *74*, I_1039-I_1044, doi:10.2208/jscejhe.74.I_1039.

34. Johnson, J.P.; Whipple, K.X. Feedbacks between Erosion and Sediment Transport in Experimental Bedrock Channels. *Earth Surf Process Landf* **2007**, *32*, 1048–1062, doi:10.1002/esp.

35. Sekine, B.M.; Member, A.; Parker, G. Bed-Load Transport on Transverse Slope. **1992**, *118*, 513–535.

36. Hooke, J.M. *River Meandering*; Elsevier Ltd., 2013; Vol. 9; ISBN 9780080885223.

37. Park, C.C. Man-Induced Changes in Stream Channel Capacity. *River channel changes* **1977**, 121–144.

38. Simon, A.; Rinaldi, M. 9.29 Incised Channels: Disturbance, Evolution and the Roles of Excess Transport Capacity and Boundary Materials in Controlling Channel Response. In *Treatise on Geomorphology*; Shroder, J.F., Ed.; Academic Press: San Diego, 2013; pp. 574–594 ISBN 978-0-08-088522-3.

39. Booij, R. *Measurments of the Flow Field in a Rotating Annular Flume, Report No. 94-2*; The Netherlands, 1994;

40. Booij, R.; Uijttewaal, W.S.J. *Modelling of the Flow in Rotating Annular Flumes*; Woodhead Publishing Limited, 1999;

41. Krishnappan, B.G.; Engel, P. Distribution of Bed Shear Stress in Rotating Circular Flume. *Journal of Hydraulic Engineering* **2004**, *130*, 324–331, doi:10.1061/(asce)0733-9429(2004)130:4(324).

42. Graham, D.I.; James, P.W.; Jones, T.E.R.; Davies, J.M.; Delo, E.A. Measurement and Prediction of Surface Shear Stress in Annular Flume. *Journal of Hydraulic Engineering* **1992**, *118*, 1270–1286, doi:10.1061/(asce)0733-9429(1992)118:9(1270).

43. Krishnappan, B.G. Rotating Circular Flume. *Journal of Hydraulic Engineering* **1993**, *119*, 758–767, doi:10.1061/(ASCE)0733-9429(1993)119:6(758).

44. Krishnappan, B.G.; Stone, M.; Granger, S.J.; Upadhayay, H.R.; Tang, Q.; Zhang, Y.; Collins, A.L. Experimental Investigation of Erosion Characteristics of Fine-Grained Cohesive Sediments. *Water (Switzerland)* **2020**, *12*, 1–14, doi:10.3390/w12051511.

45. Yang, Z.; Baptista, A.; Darland, J. Numerical Modeling of Flow Characteristics in a Rotating Annular Flume. *Dynamics of Atmospheres and Oceans* **2000**, *31*, 271–294, doi:10.1016/S0377-0265(99)00037-8.

46. Desaulniers, G.; Frenette, M. Contributions to the Study of Erosion and Deposition Mechanisms in River Bends. In *Sedimentation, Symposium to Honor Prof. H. A. Einstein*; Fort Collins (Col.) : Shen: Colorado State University, 1972; pp. 10.1-10.19.

47. Ikeda, S. On Secondary Flow and Dynamic Equilibrium of Transverse Bed Profile in Alluvial Curved Open Channel. **1974**, *Proc. JSCE*, 55–65, doi:https://doi.org/10.2208/jscej1969.1974.229_55.

48. Kikkawa, H.; Ikeda, S.; Kitagawa, A. Variation of bed profile with time in curved channel. *Proceedings of the Japan Society of Civil Engineers* **1976**, 65–75.

49. Bridge, J.S. A Revised Model for Water Flow, Sediment Transport, Bed Topography and Grain Size Sorting in Natural River Bends. *Water Resour Res* **1992**, *28*, 999–1013, doi:10.1029/91WR03088.

50. Baar, A.W.; de Smit, J.; Uijttewaal, W.S.J.; Kleinhans, M.G. Sediment Transport of Fine Sand to Fine Gravel on Transverse Bed Slopes in Rotating Annular Flume Experiments. *Water Resour Res* **2018**, *54*, 19–45, doi:10.1002/2017WR020604.

51. Fukuda, M.K.; Lick, W. The Entrainment of Cohesive Sediments in Freshwater. *J Geophys Res* **1980**, *85*, 2813–2824.

52. Kikkawa, H.; Kitagawa, A.; Ikeda, S. Flow and Bed Topography in Curved Open Channels. *Journal of the Hydraulics Division* **1976**, *102*, 1327–1342, doi:10.1061/JYCEAJ.0004615.

53. Talmon, A.M.; Struiksma, N.; Mierlo, M.C.L.M. van Laboratory Measurements of the Direction of Sediment Transport on Transverse Alluvial-Bed Slopes. *Journal Of Hydraulic Research1* **1995**, *33*, 495–517.

54. Parker, G. Discussion of "Lateral Bed Load Transport on Side Slopes" by Syunsuke Ikeda (November, 1982). *Journal of Hydraulic Engineering* **1984**, *110*, 197–199, doi:10.1061/(ASCE)0733-9429(1984)110:2(197).

55. Ikeda, S. Lateral Bed Load Transport on Side Slopes. *Journal of the Hydraulics Division* **1982**, *108*, 1369–1373, doi:10.1061/JYCEAJ.0005937.

56. Ikeda, S.; Izumi, N. Stable Channel Cross Sections of Straight Sand Rivers. *Water Resour Res* **1991**, *27*, 2429–2438, doi:10.1029/91WR01220.

57. NORITAKE Co. Ltd. Noritake Products - Catalog Lineup Available online: https://www.noritake.co.jp/eng/products/support/detail/11/ (accessed on 3 January 2022).

58. Shepherd, R.G. Incised River Meanders : Evolution in Simulated Bedrock. *American Association for the Advancement of Science* **1972**, *178*, 409–411.

59. Karni, J.; Karni, E. Gypsum in Construction: Origin and Properties. *Mater Struct* **1995**, *28*, 92–100, doi:10.1007/BF02473176.

60. TOHOKU KEISYA Co. Ltd. Tohoku Silica Sand Co. Available online: http://www.tohoku-keisya.co.jp/ (accessed on 3 January 2022).

61. 3D Artec Artec 3D EVA Available online: https://www.artec3d.com/portable-3d-scanners/artec-eva-v2 (accessed on 12 June 2021).

62. Allen, D.W. *GIS Tutorial 2 : Spatial Analysis Workbook*; Esri Press, 2016; ISBN 9781589484535.

63. Andriamboavonjy, M.R.; Terakado, T.; Izumi, N. Spatiotemporal Evolution of Bed Configurations in Mixed Bedrock-Alluvial in Uniformly Curved Channels. *Water (Basel)* **2022**, *14*, doi:10.3390/w14030397.

64. Yang, S.Q.; Tan, S.K.; Lim, S.Y. Flow Resistance and Bed Form Geometry in a Wide Alluvial Channel. *Water Resour Res* **2005**, *41*, 1–8, doi:10.1029/2005WR004211.

65. Yen, B.-C. Spiral Motion of Developed Flow in Wide Curved Open Channels. In *Sedimentation : symposium to honor Professor H. A. Einstein*; Shen, H.W., Ed.; Fort Collins (Colo.) : Shen: Colorado State University , 1972; pp. 22.1-22.33.